Tampere University

Mehdi Peyvandi Yazdi

DYNAMIC MODELLING AND CONTROL OF PMSG-BASED WIND TURBINES

Master's thesis
Faculty of Information Technology and Communication Sciences
Examiners: Paavo Rasilo
Tomi Roinila
May 2020

ABSTRACT

Mehdi Peyvandi Yazdi: Dynamic modelling and control of PMSG-based wind turbines
Master's thesis
Tampere University
Master's Degree Programme in Electrical Engineering
May 2020

With the high penetration of wind power in the electricity networks, the power system stability issues caused by modern wind turbines have become important. Nowadays, there are several different wind turbine system configurations in the market. In this thesis, the focus is on the direct-drive permanent-magnet synchronous generator wind energy conversion system (WECS) as one of the robust solutions for the large wind turbine applications due to the low demand maintenance and higher reliability because of the gearbox elimination. However, it has been revealed that using direct-driven permanent-magnet synchronous generator (DDPMSG)-based WECSs can cause fluctuations in output power due to soft drive-train system which may lead to instability due to the interaction with the power system inter-area oscillations or the WECS itself. Hence, the control design of a DDPMSG-based WECS has become a significant research topic and different control strategies have been proposed recently.

In this thesis, the dynamic behaviour of the direct-driven wind turbine coupled to the generator-connected converter is studied. Frequency-domain model of a conventional AC/DC boost converter is upgraded to a PMSG-connected converter where it is found that the q-channel input impedance of the generator has negative electrical damping behaviour in the low-frequency range. The interconnected system stability is evaluated based on the impedance ratio method where it is found that the wind turbine coupled to the converter under the open-loop condition is inherently unstable due to the negative resistor like behaviour of the converter.

The transfer functions of the open-loop model are used to design a cascaded control scheme in which the current control is considered as an inner loop and the DC-link voltage is employed as the outer loop. A non-minimum phase behaviour of the current control to the DC-link voltage is analysed in detail and the output voltage controller is tuned for the worst-case scenario.

The stability assessment of the closed-loop current control wind turbine generator (WTG)-coupled converter is studied, and it is concluded that the interconnected system can be stable as the q-channel input impedance has a high magnitude under a fast-current control loop. The control-to-DC-link voltage transfer function of WTG-coupled converter under the closed-loop current control is utilized to investigate the stability of the interconnected system under the maximum power point tracking (MPPT) mode and the controlled power (CP) mode.

It is revealed that under the MPPT mode the same fast DC-link voltage regulation that utilized for the PMSG-connected converter can stably work as there are no RHP-zeros in the control loop. However, when the operation mode switches to the controlled power mode, the WTG-coupled converter becomes unstable because a pair of RHP-zeros appears in the control loop and they impose limitations on the DC-link voltage closed-loop bandwidth. Therefore, in this study, a guideline for tuning PI controller parameters is developed to ensure the stability of the interconnected system under the CP mode. The frequency-domain model is verified through simulations; moreover, the stable operation of the WTG-coupled converter is demonstrated by the time-domain simulations.

Keywords: Direct-Driven Permanent Magnet Synchronous Generator, Wind Turbine, DC-link Voltage, Dynamic Modelling, Stability

PREFACE

This work was carried out at the Department of Electrical Engineering at Tampere University and funded by Tampere University of Technology.

I would like to take this opportunity to thank those who helped me during these years. I want to thank PhD. Jenni Rekola and Prof. Toumas Messo for their support during the first year. I want to also thank Prof. Tomi Roinila for his comments and suggestions at the final stage of this work.

I would like to address my gratitude to my supervisor Prof. Paavo Rasilo for this research opportunity and his support and patience during these years. I want to thank my parents Afsaneh and Mohammad for all the support and patience during my studies.

This work could not have been finished without the support of my wife Mahdokht and I would like to express my especial gratitude to her for all the encouragement and love during these years.

Kuopio, 20 May 2020

Mehdi Peyvandi

CONTENTS

1. INTRODUCTION 1
1.1 Wind power production statistics 1
1.2 Direct-driven PMSG-based WECS 2
1.3 Issues on the stability of DDPMSG-based WECSs 4
1.4 Damping methods 5
1.5 Thesis contributions and structure of thesis 7
2. SYSTEM CONFIGURATION OF DIRECT-DRIVEN PMSG-BASED WECS 9
2.1 Wind turbine characteristics 9
2.2 Drive-train model 11
2.3 Permanent-magnet synchronous generator model 12
3. PMSG-CONNECTED CONVERTER DYNAMIC MODEL 14
3.1 Average model 14
3.2 Steady-state operating point 17
3.3 Small-signal model 18
4. WIND TURBINE CONTROL 22
4.1 Generator-side converter control 22
4.2 Grid-side inverter control 35
5. WTG-COUPLED CONVERTER DYNAMIC MODEL 38
5.1 Dynamic properties of the wind turbine drive-train 38
5.2 Interconnected system stability assessment 41
5.3 Stability assessment under open-loop 45
5.4 Stability assessment under current-control loop 48
6. WTG-COUPLED CONVERTER UNDER DC-LINK VOLTAGE CONTROL 51
6.1 Stable operation under MPPT mode 51
6.2 Stable operation under CP mode 56
7. CONCLUSIONS 68
REFERENCES 70
APPENDIX A: CLOSED-LOOP CURRENT CONTROL TRANSFER FUNCTIONS 72
APPENDIX B: CASCADED CONTROL TRANSFER FUNCTIONS 74
APPENDIX C: STUDY CASE PARAMETERS 75

LIST OF SYMBOLS AND ABBREVIATIONS

ABBREVIATIONS

AC	Alternative current
AC/DC	AC to DC converter
CP	Controlled power
DC	Direct current
DC/AC	DC to AC converter
DDPMSG	Direct-driven permanent-magnet synchronous generator
DFIG	Double-fed induction generator
EMF	Electromotive force
ESR	Equivalent series resistance
EU	European Union
GM	Gain margin
GW	Gigawatt
Hz	Hertz
KCL	Kirchhoff's current law
KVL	Kirchhoff's voltage law
IGBT	Insulated-gate bipolar transistor
LHP	Left-half of the complex plane
LVRT	Low-voltage ride-thorough
MPP	Maximum power point
MPPT	Maximum power point tracking
MW	Megawatt
PAC	Pitch angle controller
PI	Proportional-integral
PLL	Phase-locked loop
PM	Permanent-magnet
PMSG	Permanent-magnet synchronous generator
PRBS	Pseudo-random binary sequence
RHP	Right-half of the complex plane
rpm	revolutions per minute
SSA	State-space averaging
TWh	Terawatt-hour
US	United States
UK	United Kingdom
W	Watt
VSWT	Variable-speed wind turbine
WECS	Wind energy conversion system
WFSG	Wound-field synchronous generator
WT	Wind turbine
WTG	Wind turbine generator

LATIN CHARACTERS

$\mathbf{A}$	Presenting the coefficient matrix A in state-space model
$\mathbf{B}$	Presenting the coefficient matrix B in state-space model
B_{s}	Damping coefficient
$\mathbf{C}$	Presenting the coefficient matrix C in state-space model
C_{dc}	DC-link capacitor
C_{f}	Capacitor in LC filter
C_{g}	Generator inertia in electrical expression
C_{p}	Power coefficient
C_{t}	Turbine inertia in electrical expression

$c_{0,\ldots,6}$	Constant parameters of blade characteristics
d_{A}	Duty ratio in phase A
d_{B}	Duty ratio in phase B
d_{C}	Duty ratio in phase C
d_{d}	Duty ratio for d-component
$\hat{d}_{\mathrm{d}}$	Perturbed duty ratio for d-component
d_{q}	Duty ratio for q-component
$\hat{d}_{\mathrm{q}}$	Perturbed duty ratio for q-component
$\mathbf{D}$	Presenting the coefficient matrix D in state-space model
D_{d}	Steady-state value of duty ratio for d-component
D_{q}	Steady-state value of duty ratio for q-component
e_{an}	Back-EMF voltage in phase A
$\langle e_{\mathrm{an}} \rangle$	Average value of back-EMF voltage in phase A
e_{bn}	Back-EMF voltage in phase B
$\langle e_{\mathrm{bn}} \rangle$	Average value of back-EMF voltage in phase B
e_{cn}	Back-EMF in phase C
$\langle e_{\mathrm{cn}} \rangle$	Average value of back-EMF voltage in phase C
e_{d}	Back-EMF voltage for the d-component
$\langle e_{\mathrm{d}} \rangle$	Average value of back-EMF voltage for the d-component
$\hat{e}_{\mathrm{d}}$	Perturbed back-EMF voltage for the d-component
e_{q}	Back-EMF voltage for the q-component
$\langle e_{\mathrm{q}} \rangle$	Average value of back-EMF voltage for the q-component
$\hat{e}_{\mathrm{q}}$	Perturbed back-EMF voltage for the q-component
e_{nN}	Common-mode voltage
$\langle e_{\mathrm{nN}} \rangle$	Average value of common-mode voltage
E_{d}	Steady-state value of back-EMF voltage for the d-component
E_{q}	Steady-state value of back-EMF voltage for the q-component
$\mathbf{G}$	Matrix of transfer functions
G_{cc}	Current controller transfer function
G_{ci}	Control-to-input transfer function
G_{co}	Control-to-output transfer function
G_{cr}	Cross-coupling transfer function
G_{cv}	DC-link voltage controller transfer function
i_{abcs}	Generator stator phase-currents
i_{c}	Current flowing in DC-link capacitor
i_{ina}	Input current in phase A
$\langle i_{\mathrm{ina}} \rangle$	Average value of input current in phase A
i_{inb}	Input current in phase B
$\langle i_{\mathrm{inb}} \rangle$	Average value of input current in phase B
i_{inc}	Input current in phase C
$\langle i_{\mathrm{inc}} \rangle$	Average value of input current in phase C
i_{La}	Inductor current in phase A
$\langle i_{\mathrm{La}} \rangle$	Averaged value of inductor current in phase A
i_{Lb}	Inductor current in phase B
$\langle i_{\mathrm{Lb}} \rangle$	Averaged value of inductor current in phase B
i_{Lc}	Inductor current in phase C
$\langle i_{\mathrm{Lc}} \rangle$	Averaged value of inductor current in phase C
$\langle i_{\mathrm{Ld}} \rangle$	Averaged value of inductor current for the d-component
$\hat{\imath}_{\mathrm{Ld}}$	Perturbed d-component of the inductor current
I_{Ld}	Inductor current steady-state value for the d-component
$\langle i_{\mathrm{Lq}} \rangle$	Averaged value of inductor current for the q-component
$\hat{\imath}_{\mathrm{Lq}}$	Perturbed q-component of the inductor current

I_{Lq}	Inductor current steady-state value for the q-component
i_{o}	Output current
$\langle i_{\mathrm{o}} \rangle$	Average value of output current
$\hat{\imath}_{\mathrm{o}}$	Perturbed output current
I_{o}	Output current steady-state value
$\hat{\imath}_{\mathrm{ref}}$	Perturbed current control setpoint
j	Imaginary part
J_{g}	Generator inertia
J_{t}	Turbine inertia
K_{c}	Controller gain
K_{cd}	Controller gain for the d-channel
K_{cq}	Controller gain for the q-channel
K_{iv}	Integral gain for voltage controller
K_{pv}	Proportional gain for voltage controller
K_{s}	Shaft stiffness
K_{T}	Machine torque constant
L	Generator inductance in the dq-domain
L_{abc}	Stator inductances
L_{d}	Generator inductance in the d-axis
L_{g}	Grid inductance
L_{f}	Inductance of LC filter
L_{in}	Current control loop gain transfer function
L_{q}	Generator inductance in the q-axis
L_{re}	Reluctance effect
L_{s}	Generator stator windings self-inductance
L_{t}	Shaft stiffness in electrical expression
L_{v}	DC-link voltage control loop gain transfer function
M_{s}	Mutual inductance
n_{p}	Number of pair poles
P_{grid}	Active power transfers to the grid
P_{m}	Mechanical power
P_{max}	Maximum mechanical power of the wind turbine
P_{MPPT}	Maximum power for a certain wind speed
P_{out}	Output power from DC-link
P_{w}	Wind power
Q_{grid}	Reactive power transfers to the grid
r_{c}	Equivalent series resistance of DC-link capacitor
r_{dyn}	Dynamic resistance of the wind turbine
r_{eq}	Overall resistance of each phase during on-state switching
r_{L}	Equivalent series resistance of stator inductor
r_{mppt}	Dynamic resistance of MPPT
r_{s}	Stator winding resistance
R	Blade radius
R_{fc}	Damping coefficient in electrical expression
R_{in}	Converter input impedance for the low frequency
R_{st}	Static resistance of the Converter for the low frequency
s	Laplace variable
T_{g}	Electromechanical torque of generator
T_{m}	Turbine shaft torque
T_{oi}	Output-to-input transfer functions
T_{t}	Mechanical torque applied on turbine rotor
u_{abcs}	Generator stator phase-voltage

u_{c}	DC-link capacitor voltage
$\langle u_{\mathrm{c}} \rangle$	Average value of capacitor voltage
$\hat{u}_{\mathrm{c}}$	Perturbed DC-link capacitor voltage
$u_{\mathrm{g,abc}}$	Grid voltage
$\langle u_{\mathrm{La}} \rangle$	Average value of the voltage across the inductor in phase A
$\langle u_{\mathrm{Lb}} \rangle$	Average value of the voltage across the inductor in phase B
$\langle u_{\mathrm{Lc}} \rangle$	Average value of the voltage across the inductor in phase C
u_{o}	Output voltage
$\langle u_{\mathrm{o}} \rangle$	Average value of output voltage
$\hat{u}$	Input variable vector
$\hat{u}_{\mathrm{o}}$	Perturbed output voltage
U_{o}	Output voltage steady-state value
$\boldsymbol{U}$	Input variables vectors in Laplace domain
v_{w}	Wind speed
$\hat{x}$	State variables vector
$\boldsymbol{X}$	State variables vectors in Laplace domain
$\hat{y}$	Output variables vector
Y_{in}	Input admittances transfer functions
$\boldsymbol{Y}$	Output variables vectors in Laplace domain
Z_{o}	Output impedance transfer function
Z_{oS}	Output impedance transfer function of wind turbine

GREEK CHARACTERS

Δ	Denominator transfer function
ρ	Air density
λ	Tip speed ratio
λ_{abcs}	Stator flux linkages
λ_{m}	Maximum flux linkage of permanent-magnet
$\lambda_{\mathrm{m,abcs}}$	Stator flux linkages of permanent-magnets
ζ_{res}	Damping ratio of the torsional resonance
$\zeta_{\mathrm{anti-res}}$	Damping ratio of the anti-torsional resonance
β	Pitch angle
m/s	meter per second
θ_{c}	Phase angle of the control system reference frame
θ_{e}	Electrical rotor angle
θ_{r}	Rotor angle
θ_{s}	Shaft angle
$\hat{\theta}_{\mathrm{s}}$	Perturbed shaft angle
$\omega_{\mathrm{anti-res}}$	Anti-resonance frequency (rad/s)
ω_{B}	Control loop bandwidth frequency (rad/s)
ω_{e}	Electrical angular frequency
ω_{g}	Generator angular speed
$\widehat{\omega}_{\mathrm{g}}$	Perturbed generator angular speed
ω_{Lp}	Control-to-output transfer function pole frequency (rad/s)
ω_{Lz}	Control-to-output transfer function zero frequency (rad/s)
ω_{MPP}	Maximum power point frequency (rad/s)
ω_{n}	Torsional natural frequency (rad/s)
ω_{nc}	Crossover frequency (rad/s)
$\omega_{\mathrm{n-res}}$	Resonance frequency (rad/s)
ω_{OP}	Operating point frequency (rad/s)
ω_{osc}	Drive-train torsional frequency
ω_{p}	LHP-pole frequency (rad/s)
ω_{pc}	Transfer function pole frequency (rad/s) of current controller

ω_{r}	Rotor angular frequency
ω_{s}	Grid angular frequency
ω_{sw}	Switching frequency (rad/s)
ω_{t}	Turbine angular speed
$\widehat{\omega}_{\mathrm{t}}$	Perturbed turbine angular speed
ω_{z}	RHP-zero frequency (rad/s)
ω_{zc}	Transfer function zero frequency (rad/s) of current controller
ω_{zv}	Transfer function zero frequency (rad/s) of voltage controller
α_{I}	Closed-loop current control bandwidth
$\frac{d}{dt}$	Derivate

SUBSCTRIPTS

-c	Closed-loop current control
-cv	Both DC-link voltage and current control loops are closed
-d	D-channel
-dq	Between d-channel and q-channel
-inf	Infinite bandwidth
-max	Maximum value
-q	Q-channel
-qd	Between q-channel and d-channel

SUPERSCRIPTS

-1	Inverse of matrix or transfer function
-ref	Reference
-S	Source dynamics included in the transfer function
-SL	Source and load dynamics included in the transfer function

1. INTRODUCTION

This chapter introduces the general background of the topics covered in this study. An overview on the production capacity of wind energy in European Union (EU) zone along with Finland's future targets in the national level is described. The reason behind the motivation of this thesis to focus on direct-driven permanent-magnet synchronous generator wind turbines is explained and the stability issues regarding this type of WECSs are presented. Furthermore, a short literature review on the damping approaches to overcome the instability problem caused by the gearless wind turbine construction are discussed. Finally, the thesis contributions and structure are explained.

1.1 Wind power production statistics

For decades, the fossil fuels have been the main source of energy production in all over the world. However, during the last decade, renewable energy has become more popular due to a rise in climate change concerns and the among of all type of the green energies, wind and solar energy are the most promising solutions when sustainability and clean energy are concerned. The capacity of power generation from wind and solar energy have significantly increased in the European Union. Based on the surveys conducted by WindEurope institution, it has been reported that, in 2018, wind power installations with 48% of the total new renewable energy installations was the most popular energy among other forms in EU zone where renewable energy-based power generation consists of 95% of the newly installed power capacity in Europe. Moreover, the top three countries with the largest installed wind power capacity during the last year were Germany, Spain and the UK, respectively, while Denmark with 41% share of wind energy in the power generation was ranked on the top in the Europe. However, despite the significant increase in the wind power capacity installations during the recent years, the gross annual installations dropped to 11.7 gigawatt (GW) in 2018 showing 32% decrease compared to 2017 [1]. According to [2], the total installed wind power capacity in Finland at the end of 2018 was 2041 megawatt (MW), including 698 onshore wind turbines (WTs) so this figure reached to 2381 MW as 340 MW new wind capacity completed by the end of 2019. The annual wind power production target in Finland is set to generate 30 terawatt-hour (TWh) by 2030, which would be 30% of its electricity demand at the time while only 6.7%

of Finland's electricity consumption was generated by wind power at the end of 2018 and this increased approximately 20% because of the new wind turbine installations in 2019.

Although fossil fuels have had negative impacts on the environment for a long time, they have been known as very reliable sources from the electricity network designers' point of view. However, wind energy as one of the fast-growing clean energy sources brings many challenges to the electric power grids. For example, it has been reported in the literature [3] that the stability of the electricity network may not be guaranteed in the networks with the high penetration of wind turbines. Therefore, given the significant share of wind energy in the total electricity production, the need of analysing the effect of WECSs on the grid network performance is essential.

1.2 Direct-driven PMSG-based WECS

WECSs consist of a wind turbine, generator and power electronic devices are used to harvest wind energy and convert it into the electrical energy. Generally, wind turbines are divided into the two main categories, fix-speed and variable-speed wind turbines where the latter one delivers more electric power into the grid because of the wider operating range. The variable-speed wind turbines can mainly be categorized based on the type of the generator used in the WECS. The two most common types are doubly-fed induction generator and permanent-magnet synchronous generator (PMSG)-based WECS wherein the former, the generator terminals are directly connected to the grid and the AC/DC/AC converters are in the half-scale of power rating, while in the latter one, the generator is connected to the grid terminal through the DC-link with the two full-scale back-to-back converters. A typical system configuration of a PMSG-based wind energy system is shown in Figure 1.

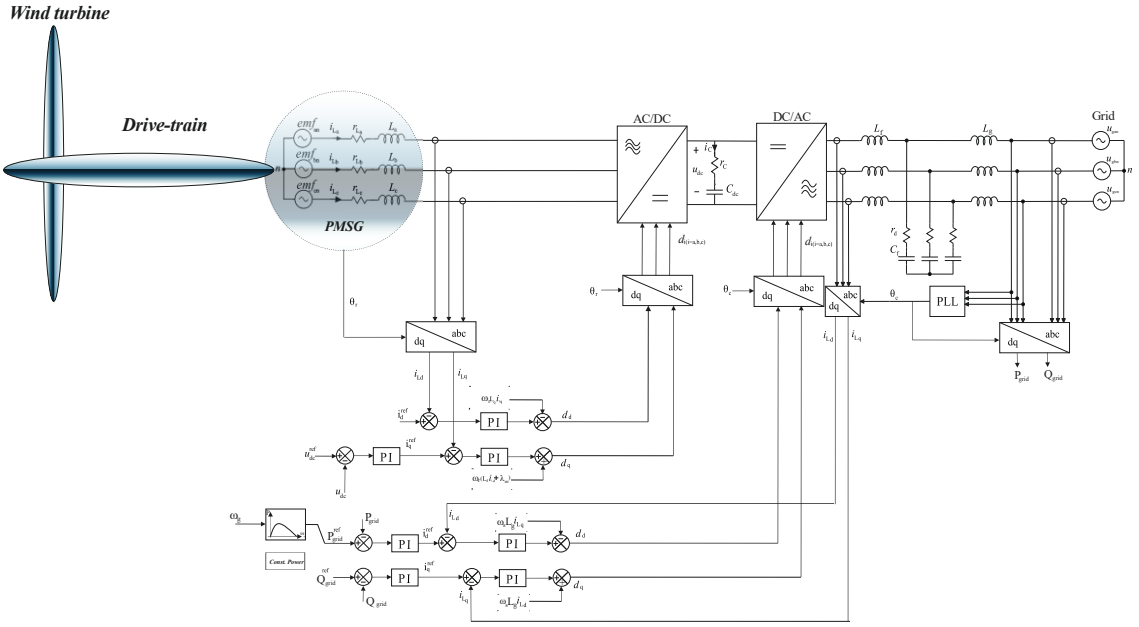

***Figure 1**. Configuration of a direct-driven PMSG-based WECS*

The nominal speed of the generators designed for wind energy application is higher than the wind turbine speed thus a gearbox is typically utilized in the drive-train system to step-up the turbine shaft speed. However, based on the findings in the literature [4], the most turbine mechanical failures which lead to downtime are caused by the gearbox and to avoid such shot downs and increase the WECS reliability, regular maintenance is needed. In addition to extra cost because of maintenance demand, higher weight and losses are also imposed to the WECS in which a gearbox is used. To overcome the disadvantages of using the gearbox, the idea of a direct-driven construction has been proposed in the recent years where the gearbox is eliminated from the WECS and the wind turbine shaft is directly connected to the generator rotor [5]. As mentioned earlier, the standard generators work at high speeds since the higher efficiency can be achieved. Therefore, these high-speed generators cannot be used in the direct-driven construction as the gearbox is not part of the drive-train to boost up the turbine shaft speed and a low-speed generator should be designed to comply with the low-speed applications as a large wind turbine typically rotates at 10-20 revolutions per minute (rpm). The gearless construction is normally recommended for the large wind turbines where the power production is in the megawatt range. Hence, the generator developed for this application must have a large rotor diameter to be capable of producing a high torque in a low shaft speed operation and a large number of poles to get the desired frequency.

Asynchronous and synchronous generators are the two most common standard AC generators utilize in the conventional WECSs. Based on the research conducted in [6], the asynchronous AC generators are not desired to be adopted to design requirements for

the direct-driven application since the generator with the high number of poles require a large amount of magnetizing current which leads to poor efficiency. However, synchronous AC generators are recommended as the only robust solution for the gearless construction.

Wound field synchronous generators (WFSG) and permanent-magnet synchronous generators (PMSG) are the well-known types of synchronous generators in wind energy applications. In the former, the DC excitation system provides magnetization while permanent magnets are used in the latter. From one hand, the WFSG type benefits from the adjustable DC excitation by which the unity power factor can be achieved and likewise, the size of AC/DC converter connected to the generator can be reduced as the converter is able to work at the same power rating that of the generator. On the other hand, the DC excitation system causes losses and requires maintenance due to using slip rings which increase costs and rises reliability concern.

Utilizing permanent magnets, the DC excitation system can be eliminated meaning low maintenance requirements and reduction in losses. Meanwhile, the use of permanent magnets in synchronous generators increase the cost as PM materials are very expensive. Moreover, the excitation system cannot be controlled according to the operating point [7]. Different types of the WECSs were compared based on the cost and energy yield model according to the survey conducted in [8] and it has been reported that the DDPMSG can be a promising solution for the large wind turbine despite the high price. Furthermore, to support the WECS concept based on PMSG, it should be mentioned that the permanent-magnet (PM) materials are expecting to become cheaper as the production of the rare-earth materials no longer relies on one single-source country which is China and some new resources have been discovered in Australia, Canada and the US [9]. Moreover, according to [1], PMSG-based WECSs with gearless construction are used in the most of the ongoing wind energy projects. Hence, the focus of this thesis is on the DDPMSG-based WECSs as it is expected that this type of WECS will be widely developed in the future. However, these modern WECS construction may bring some instability issues into the electricity network which need to be addressed thus in the next section, the issue on network instability-related DDPMSG-based WECS is shortly described.

1.3 Issues on the stability of DDPMSG-based WECSs

Due to climate change concerns, the renewable energy solution is becoming more attractive so that the contribution of WECSs into the grid networks has significantly in-

creased during the last decade. Although this trend is seen positively in terms of environmental matters, it also raises some challenges for electricity network designers as the stability of the grid with a high penetration of wind power will largely rely on the WECS dynamic characteristic. As discussed in the previous section, DDPMSG-based WECS are suggested in the literature as a promising solution for the large wind turbine application. However, increasing the size of the turbine in order to extract more energy and having a large rotor diameter in the direct-driven application with a low-speed operation affect the dynamic performance of the WECS which may result in instability in the WECS or in the power system due to interaction between the drive-train torsional modes and the low-frequency modes of the grid [10].

The first instability experiment caused by the drive-train modes occurred at the Rejsby Hede wind farm in Denmark where the contribution of wind energy in the electricity production was very high [3]. In many researches, the effect of the drive-train components and the structure of the generator on the torsional modes have been studied. It has been addressed in [11] that the shaft stiffness of a WECS drive-train is inversely proportional to the square of the number of pole pairs which means the stiffness is low for a high-pole PMSG. Hence, the dynamic of the electrical rotor angle can be affected by the mechanical torsion which may influence the dynamic performance of the whole WECS. The torsional modes produced by the drive-train system can lead to oscillation in the generator rotor speed and likewise, the fluctuation in the output power. Damping these oscillations is highly important as they typically oscillate in the frequency range of 0.1-10 Hz where there is a high risk of interaction with the low frequencies in power system [12]. Therefore, it is essential to consider the drive-train dynamic into the WECS model and it becomes even more important when it comes to a high-pole PMSG in which no damping windings are utilized. Consequently, damping techniques are required to be employed in the control system. Hence, the damping methods proposed in the literature are briefly discussed in the following section.

1.4 Damping methods

Given the dynamic effect of drive-train in the gearless construction on the WECS behaviour, the control scheme of the wind turbine needs to be adopted for the DDPMSG-based WECS to ensure the system stability in which a damping technique is added to the control system. The methods for eliminating torsional vibrations can be classified into the two major categories. The extenuation of torsional vibrations by means of additional mechanical attenuation through the use of rubber mounts or couplings and modified controller-based methods including pitch angle control (PAC) and modified power electronic

converter controllers. The former way of damping is less popular due to the extra cost associated with this approach. One of the damping methods based on modified controller is blade pitching in which a torque component produced using blades opposes the rotor speed changes to damp the vibrations. However, it has been reported that the blade pitching damping approach is an inefficient method as the extracted output power decreases. As it has been reported in the literature [13], the modified converter controller is found to be very robust and effective damping method. Hence, in this thesis, this approach will be used to overcome the oscillatory modes of the wind turbine drive-train.

The damping method based on the modified converter controller can be divided into the two categories depending on the control strategy utilized for the full-scale converter configuration. Generally, there are the two main control schemes for DDPMSG-based WECSs with full-scale power converter where the WECS consists of a wind turbine directly connected to the PMSG and the two back-to-back voltage-sourced converters, which link the PMSG to the grid. In the conventional control strategy, the machine-side converter is responsible to extract the maximum power from the wind turbine, which can be done using maximum power point tracking (MPPT) algorithms, and transfer the power to the grid-side inverter through the DC-link while the inverter connected to the grid is used to control the DC-link voltage. In the alternative control scheme, however, the machine-side converter regulates the DC-link voltage through controlling the PMSG electrical torque whilst the grid-connected inverter is used to set the maximum power point tracking and control the power flow into the grid. For damping technique, in the conventional control structure, an auxiliary generator torque component is used to attenuate the vibrations while the auxiliary attenuation can be obtained through the DC-link voltage controller in the alternative control scheme [14].

Many investigations regarding damping methods have been conducted and several approaches have been proposed in the literature. In [15], where the conventional control scheme is used and the auxiliary damping is applied using the generator torque controller, the proposed damping strategy to attenuate torsional vibrations in controlled power (CP) mode is based on extracting a damping signal from a high-pass filter measure of the rotor speed and augments the PMSG torque setpoint. However, the performance of the proposed approach is highly dependent on the filter parameters which can challenge the system reliability. As an alternative way to derive the ac component of the generator rotor speed, to avoid filtering, the estimated DC-link capacitor current is used in [16]. This approach is proved to be robust in simulations; however, no experimental evidence is reported. Although damping methods based on the conventional control scheme are proved to be effective, it has been reported in [14] that under this approach, the WECS

output power is sensitive to the power fluctuations caused by torsional modes. Moreover, it has been found that the alternative control scheme is more effective than the traditional structure in case of low-voltage ride-thorough (LVRT) condition as the PMSG has an inherent LVRT capability [17,18]. Recently, the application of the alternative control structure in the DDPMSG-based WTs has been widely addressed in the literature [19,20]. However, the focus of these investigations has been mostly on the LVRT capability of this control strategy so that its performance under the CP and the MPPT are critically missing. Since the main function of a WECS is extracting the maximum power from the wind energy, in this thesis, the dynamic behaviour of the generator-side converter under the MPPT mode is discussed where the alternative control structure is utilized. Furthermore, the WECS must be capable of operating under the CP mode as one of the grid code requirements. Therefore, the machine-side converter dynamics and control design are studied for the CP mode.

1.5 Thesis contributions and structure of thesis

The main contributions of this thesis can be summarized as follows:

- Frequency domain model of a PMSG-connected converter under the alternative control scheme is developed where it is found that the open-loop input impedance of the converter has negative resistor-like behaviour in the low frequency.
- Dynamic model of PMSG-connected converter is utilized for the design of DC-link voltage loop control. It is revealed that the worst-case scenario in controller design occurs at the maximum torque point for the highest operating wind speed where the right-half-plane zero has the lowest frequency.
- The effect of wind turbine drive-train dynamics on the PMSG-connected converter is studied where it is realized that the interconnected system is unstable due to electrical negative damping behaviour of the converter input impedance. Furthermore, besides the pair of complex RHP-zero caused by the drive-train torsional mode, one real right-half-plane zero appears in the transfer function of control-to-output voltage where the dynamic resistance of wind turbine is larger than the static resistance of the converter.
- The stability of the interconnected system is evaluated for the MPPT and CP operation modes when the PMSG-connected converter is under the DC-link voltage control. It is concluded that the WTG-coupled converter under the fast DC-link voltage control designed based on the electrical dynamics is stable under the MPPT mode. However, the same voltage controller leads to instability when the

operation mode switches to the controlled power. Therefore, the stability boundaries for tuning the proportional-integral (PI) controller parameters of the DC-link voltage controller is developed to ensure the stable operation under the controlled power mode.

The thesis is structured as follows. The system configuration of the PMSG-based WECS is introduced in Chapter 2. The small-signal model of the PMSG-connected converter is expressed in Chapter 3. The control strategy used for the WECS is described in Chapter 4. Chapter 5 presents the effect of the wind turbine dynamics on the PMSG-connected converter and the dynamic behaviour of the transfer function of the control-to-DC-link voltage is discussed. The stability of the output voltage-controlled WTG-coupled converter under the MPPT and CP modes is evaluated in Chapter 6. The final chapter is devoted to the conclusions.

2. SYSTEM CONFIGURATION OF DIRECT-DRIVEN PMSG-BASED WECS

The kinetic energy contained in wind can be converted into the electrical energy through the WECSs where the kinetic energy captured by the wind turbine blades rotates the drive-train shaft and consequently the coupled generator shaft that produces the electrical energy. In this Chapter, the wind energy conversion system components are explained as the following: the aerodynamic characteristic of the wind turbine is shortly discussed, the model of the two-mass drive-train system is presented, and the three-phase model of the PMSG in the abc-frame is expressed, respectively. The model of grid-connected inverter, the transformer and the grid are out of the scope of this thesis since the focus is on modelling and control of the machine-side converter.

2.1 Wind turbine characteristics

Generally, the wind turbine operation can be characterized by the extracted mechanical power from the wind power P_{w} which can be given as

$$P_{\mathrm{w}} = \frac{1}{2}\rho\pi \mathrm{R}^2 v_{\mathrm{w}}^3, \tag{2.1}$$

where ρ denotes the air density, R represents the radius of the rotor blade and v_{w} is the wind speed. Equation (2.1) reveals that the wind power is significantly sensitive to the wind speed. Moreover, as the wind power is proportional to the square of the wind turbine blade radius, one concludes that by doubling the radius the wind power can be four times that is the main reason why the use of large wind turbines are growing. The wind power expressed in (2.1) represents an ideal power that a WECS can capture. However, in practice, the power coefficient C_{p} determines the amount of the mechanical power that can be obtained from the wind power. The power coefficient can be given as

$$C_{\mathrm{p}}(\lambda, \beta) = \frac{P_{\mathrm{m}}}{\frac{1}{2}\rho\pi \mathrm{R}^2 v_{\mathrm{w}}^3}, \tag{2.2}$$

where P_{m} represents the mechanical power and power coefficient is shown as a function of the tip speed ratio λ and pitch angle β. Therefore, the actual mechanical power that can be extracted by the wind turbine is expressed as

$$P_{\mathrm{m}} = \frac{1}{2} C_{\mathrm{p}}(\lambda, \beta)\rho\pi \mathrm{R}^2 v^3. \tag{2.3}$$

The wind turbines characteristics can be differentiated by the power coefficient as

$$C_{\mathrm{p}}(\lambda,\beta) = c_0\left(\frac{c_1}{\lambda_{\mathrm{i}}} - c_2\beta - c_3\right)e^{\frac{c_4}{\lambda_{\mathrm{i}}}}, \tag{2.4}$$

$$\frac{1}{\lambda_{\mathrm{i}}} = \frac{1}{\lambda + \mathrm{c}_5\beta^2} - \frac{\mathrm{c}_6}{\beta^3+1}, \tag{2.5}$$

where it depends on the aerodynamic characteristics of blades defined by constant parameters $c_0, \ldots\ldots\ c_6$ [21]. It can be seen from the power coefficient equation that the tip speed ratio is an important factor in determining the efficiency of wind turbine. The tip speed ratio can be defined to be the ratio between the speed of the turbine blades and the wind speed as

$$\lambda = \frac{\mathrm{R}\omega_t}{v_{\mathrm{w}}}, \tag{2.6}$$

where ω_{t} is the turbine angular speed.

The blade pitch angle is basically used in mechanical controllers to regulate the captured power by the wind turbine through changing the alignment of the turbine blades with the wind. The pitch angle controllers are mostly utilized in the large wind turbine applications where their main responsibility is to keep the wind turbine during the gust condition. In this thesis, the operation of the pitch controller will not be discussed since the focus is on the operating points below the rated wind speed thus the pitch angle can be assumed to be zero.

By substituting (2.6) into (2.4) and (2.5), the coefficient power can be obtained as a function of the turbine angular speed. Hence, the $P_{\mathrm{m}} - \omega_{\mathrm{t}}$ curve in which the characteristic of the turbine power is as a function of the turbine angular speed can be derived for the different wind speeds as illustrated in Figure 2.

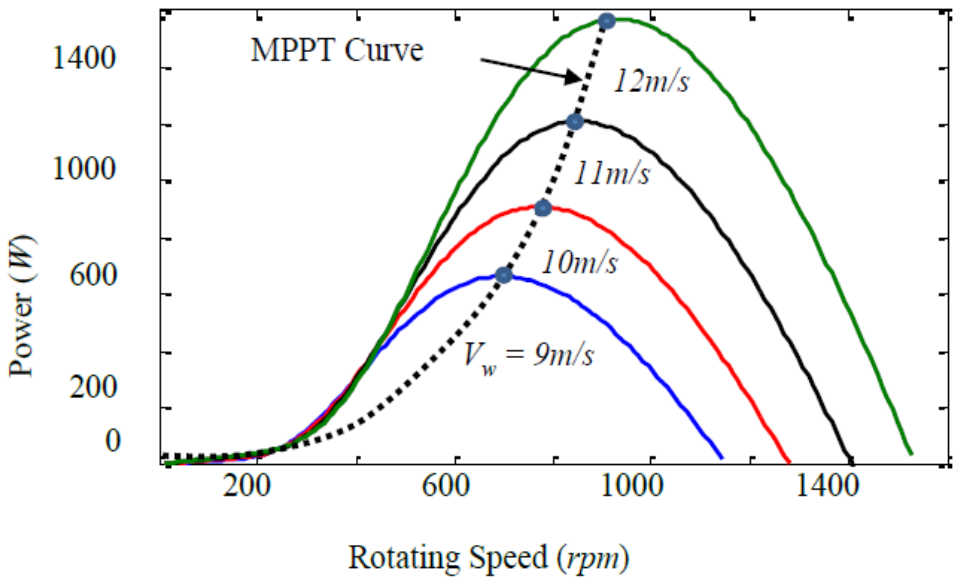

Figure 2. $\boldsymbol{P_m - \omega_t}$ *curve for different wind speed [22]*

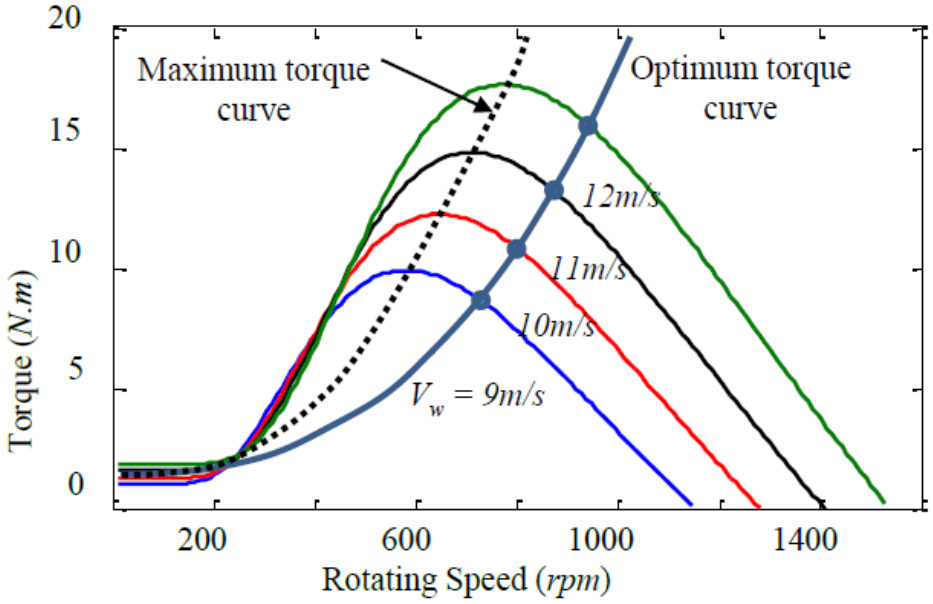

Figure 3. *$T_m - \omega_t$ curve for different wind speed [22]*

Using the mechanical power presented in (2.3), the turbine shaft torque of a wind turbine can be expressed as

$$T_{\mathrm{m}} = \frac{P_{\mathrm{m}}}{\omega_{\mathrm{t}}} = \frac{0.5C_{\mathrm{p}}(\lambda,\beta)\rho\pi\mathrm{R}^2 v_{\mathrm{w}}^3}{\omega_{\mathrm{t}}}. \tag{2.7}$$

Like the $P_{\mathrm{m}} - \omega_{\mathrm{t}}$ curve, the turbine torque can be depicted as a function of the turbine angular speed as shown in Figure 3 where it can be observed that the optimum torque at which the MPPT occurs is located in the right-hand side of the curve. It will be discussed later that the stable region for the WT operation is the right-hand side of the $T_{\mathrm{m}} - \omega_{\mathrm{t}}$ curve.

2.2 Drive-train model

The different types of the drive-train system of WECSs can be described based on the speed of the generator that is used in the transmission system. The most common types are a high-speed generator coupled to a three-stage gearbox, a medium-speed generator connected to a one/two-stage gearbox and a low-speed generator directly coupled to the turbine shaft known as a gearless construction. Due to the downtime issue caused by the gearbox components and the high demand for maintenance, the direct-driven technology has become popular during the recent decade.

Depending on the focus of the research, the complexity of the drive-train modelling can be determined. It has been suggested in the literature [10] that the two-mass model of the drive-train is necessary for the WECSs stability studies in which the effect of shaft flexibility and consequently the drive-train torsional modes accurately captured. Moreover, higher-order models have been proposed in the literature [23]. However, as they are

commonly utilized for the mechanical fatigue of the drive-train studies which is out of scope of this thesis, a two mass model drive-train is considered in this work that can be presented as

$$J_{\mathrm{t}}\frac{d\omega_{\mathrm{t}}}{dt} = T_{\mathrm{t}} - k_{\mathrm{s}}\theta_{\mathrm{s}} - B_{\mathrm{s}}\omega_{\mathrm{t}} + B_{\mathrm{s}}\omega_{\mathrm{g}}\,, \tag{2.8}$$

$$J_{\mathrm{g}}\frac{d\omega_{\mathrm{g}}}{dt} = k_{\mathrm{s}}\theta_{\mathrm{s}} - T_{\mathrm{g}} + B_{\mathrm{s}}\omega_{\mathrm{t}} - B_{\mathrm{s}}\omega_{\mathrm{g}}\,, \tag{2.9}$$

$$\frac{d\theta_{\mathrm{s}}}{dt} = \omega_{\mathrm{t}} - \omega_{\mathrm{g}}\,, \tag{2.10}$$

where, J_{t} and J_{g} are the inertia of the turbine and the generator, respectively. ω_{g} is the PMSG rotor speed, and ω_{t} is the speed of shaft. θ_{s} denotes the shaft angle, K_{s} and B_{s} respectively represent the shaft stiffness and damping coefficient. T_{t} is the input mechanical torque applied on the wind turbine rotor and the electromagnetic torque developed inside the PMSG is shown by T_{g}. Furthermore, the rotational frequency of the drive-train torsional mode in the two-mass model can be given as

$$\omega_{\mathrm{osc}} = \sqrt{\frac{K_{\mathrm{s}}(J_{\mathrm{t}} + J_{\mathrm{g}})}{J_{\mathrm{t}}J_{\mathrm{g}}}}\,. \tag{2.11}$$

2.3 Permanent-magnet synchronous generator model

An equivalent wye scheme of a PMSM model in abc-frame is derived according to [24] where all voltages and currents are instantaneous values. Using the stator instantaneous voltage equations, the PMSG model may be expressed in matrix form as

$$u_{\mathrm{abcs}} = \frac{d}{dt}\lambda_{\mathrm{abcs}} - r_{\mathrm{s}}i_{\mathrm{abcs}}\,, \tag{2.12}$$

where r_{s} is the stator winding resistance. The terminal stator phase-voltage and phase-current vectors are u_{abcs} and i_{abcs}, respectively. λ_{abcs} represent the stator flux linkages and $\frac{d}{dt}$ denotes derivate. As the wind energy is the study case in this thesis, the generator-mode convention is applied here; therefore, the direction of the stator current is chosen to be positive. The stator flux linkages can be given as

$$\lambda_{\mathrm{abcs}} = L_{\mathrm{s}}(\theta_{\mathrm{r}})i_{\mathrm{abcs}} + \lambda_{\mathrm{m,abcs}}(\theta_{\mathrm{r}}), \tag{2.13}$$

where

$$\lambda_{\mathrm{m,abcs}}(\theta_{\mathrm{r}}) = \left[\lambda_{\mathrm{m}}\cos\theta_{\mathrm{r}} \quad \lambda_{\mathrm{m}}\cos\left(\theta_{\mathrm{r}} - \tfrac{2\pi}{3}\right) \quad \lambda_{\mathrm{m}}\cos\left(\theta_{\mathrm{r}} + \tfrac{2\pi}{3}\right)\right]^{\mathrm{T}}. \tag{2.14}$$

Here, $\lambda_{\mathrm{m,abcs}}(\theta_{\mathrm{r}})$ is the flux linkage vector of the permanent magnets and λ_{m} is the maximum flux linkage produced by the rotor magnet. θ_{r} is the rotor angle which defines the

angle between magnetic axis of the rotor and the stator phase a winding. $L_{\mathrm{s}}(\theta_{\mathrm{r}})$ denotes the inductance matrix of the generator stator windings and can be expressed as

$$L_{\mathrm{s}}(\theta_{\mathrm{r}}) = \begin{bmatrix} L_{\mathrm{s}} & M_{\mathrm{s}} & M_{\mathrm{s}} \\ M_{\mathrm{s}} & L_{\mathrm{s}} & M_{\mathrm{s}} \\ M_{\mathrm{s}} & M_{\mathrm{s}} & L_{\mathrm{s}} \end{bmatrix} - L_{\mathrm{re}} \begin{bmatrix} \cos 2(\theta_{\mathrm{r}}) & \cos 2\left(\theta_{\mathrm{r}} - \frac{\pi}{3}\right) & \cos 2\left(\theta_{\mathrm{r}} - \frac{2\pi}{3}\right) \\ \cos 2\left(\theta_{\mathrm{r}} - \frac{\pi}{3}\right) & \cos 2\left(\theta_{\mathrm{r}} - \frac{2\pi}{3}\right) & \cos 2\left(\theta_{\mathrm{r}} - \frac{3\pi}{3}\right) \\ \cos 2\left(\theta_{\mathrm{r}} - \frac{2\pi}{3}\right) & \cos 2\left(\theta_{\mathrm{r}} - \frac{3\pi}{3}\right) & \cos 2\left(\theta_{\mathrm{r}} - \frac{4\pi}{3}\right) \end{bmatrix}. \quad (2.15)$$

The stator self-inductance and the mutual inductance are denoted by L_{s} and M_{s}, respectively. L_{re} represents the reluctance effect which depends on the rotor position. Substituting (2.15) to (2.12), the abc-frame model of the PMSG can be presented as

$$u_{\mathrm{abcs}} = \frac{d}{dt}\lambda_{\mathrm{m,abcs}}(\theta_{\mathrm{r}}) - r_{\mathrm{s}} i_{\mathrm{abcs}} - \frac{d}{dt}(L_{\mathrm{s}}(\theta_{\mathrm{r}}) i_{\mathrm{abcs}}), \quad (2.16)$$

where the first term represents the back-electromotive force (EMF) vector, induced by the magnet flux in the stator winding. The abc-frame three-phase model of the PMSG derived in this section will be used in the next Chapter for the small-signal modelling of the PMSG where it is connected to the DC-link through the AC/DC converter.

3. PMSG-CONNECTED CONVERTER DYNAMIC MODEL

In Chapter 2, the configuration of the direct-driven PMSG-based WECS was described. The aim of this chapter is deriving the small-signal model of the PMSG connected to the boost converter in rotor reference frame. The dynamic modelling method used in here is explicitly described in [25] where the frequency-domain model for a grid-connected inverter with a current source as the input in parallel with a capacitor is developed. However, in this thesis, the model of a PMSG-connected converter is presented similarly as a conventional voltage source boost converter connected with a current sink. In this way, considering the electrical dynamics much faster than mechanical ones, the back-EMF voltages of the PMSG are presented by the three-phase ac-voltage sources as the input terminals. The generator phase stator resistances and inductances are taken as the input filter inductances of a two-level AC/DC boost converter. The DC-link capacitor is connected to a current sink because of the alternative control scheme that is studied in this thesis.

Hence, in this Chapter, the well-known state-space averaging (SSA) technique is used to model the dynamic behaviour of the three-phase PMSG-connected boost converter. The averaged-model of the PMSG-connected converter is derived by averaging over the switching period. Then, the three-phase non-linearized average-model is transformed into the dq-domain using Park transformation. The model linearization is performed at the predefined steady-state operating point that can be obtained based on the control strategy of the wind turbine. The linearized time-domain state-space equations are transformed to the frequency-domain where the matrix of the transfer functions representing the dynamics of the PMSG-connected converter is presented.

3.1 Average model

The power stage of the PMSG-connected converter is illustrated in Figure 4 where the PMSG is modelled with a three-phase voltage in series with the stator resistances and inductances shown by r_{s} and L_{abc}, respectively. The generator terminals are connected to the two-level converter which includes six switches with Insulated-Gate Bipolar Transistor (IGBT) parallel with diode. The DC-link is represented by a current sink parallel with a capacitor C_{dc}. Since the focus of this study is on the control design and stability analysis, the ideal switches can be considered in the modelling where the effect of IGBTs

parallel with diodes are ignored. Considering the described power stage for the PMSG-connected converter, its average-model can be studied where the input variables are the back-EMF voltages e_{abc} generated by magnets and the output current i_{o} which can be determined by the output power. The output voltage u_{o} and the input currents $i_{\mathrm{in,abc}}$ are the output variables. And the state variables are the generator inductor current $i_{\mathrm{L,abc}}$ and the DC-link capacitor voltage u_{c}.

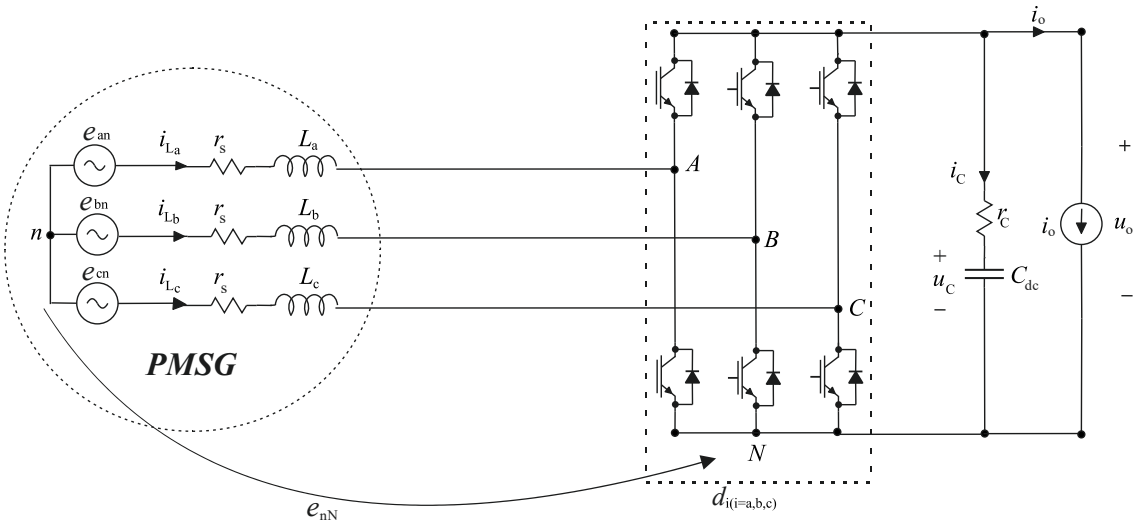

***Figure 4**. Power stage of PMSG-connected converter*

According to Figure 4, the voltage across the inductor in each phase can be obtained using Kirchhoff's voltage law (KVL) by multiplying equations with the duty ratio of $d_{i(\mathrm{A,B,C})}$. And the current flowing through the DC-link capacitor can be computed using Kirchhoff's current law (KCL). Therefore, with representing the average values with angle brackets, the average-model of the PMSG-coupled boost converter in three-phase system can be expressed as

$$\langle u_{\mathrm{La}}\rangle = \langle e_{\mathrm{an}}\rangle - \langle e_{\mathrm{nN}}\rangle - d_{\mathrm{A}}\langle u_{\mathrm{o}}\rangle - r_{\mathrm{eq}}\langle i_{\mathrm{La}}\rangle, \quad (3.1)$$
$$\langle u_{\mathrm{Lb}}\rangle = \langle e_{\mathrm{bn}}\rangle - \langle e_{\mathrm{nN}}\rangle - d_{\mathrm{B}}\langle u_{\mathrm{o}}\rangle - r_{\mathrm{eq}}\langle i_{\mathrm{Lb}}\rangle, \quad (3.2)$$
$$\langle u_{\mathrm{Lc}}\rangle = \langle e_{\mathrm{cn}}\rangle - \langle e_{\mathrm{nN}}\rangle - d_{\mathrm{C}}\langle u_{\mathrm{o}}\rangle - r_{\mathrm{eq}}\langle i_{\mathrm{Lc}}\rangle, \quad (3.3)$$
$$\langle i_{\mathrm{C}}\rangle = d_{\mathrm{A}}\langle i_{\mathrm{La}}\rangle + d_{\mathrm{B}}\langle i_{\mathrm{Lb}}\rangle + d_{\mathrm{C}}\langle i_{\mathrm{Lc}}\rangle - \langle i_{\mathrm{o}}\rangle, \quad (3.4)$$
$$\langle u_{\mathrm{o}}\rangle = \langle u_{\mathrm{c}}\rangle + r_{\mathrm{c}}\langle i_{\mathrm{c}}\rangle, \quad (3.5)$$
$$\langle i_{\mathrm{ina}}\rangle = \langle i_{\mathrm{La}}\rangle, \quad (3.6)$$
$$\langle i_{\mathrm{inb}}\rangle = \langle i_{\mathrm{Lb}}\rangle, \quad (3.7)$$
$$\langle i_{\mathrm{inc}}\rangle = \langle i_{\mathrm{Lc}}\rangle, \quad (3.8)$$

where the voltage equations over the inductors (3.1) - (3.3) are shown by $u_{\mathrm{L,abc}}$. The DC-link capacitor current i_{C} is calculated as in (3.4). The output voltage u_{o} is equal to the DC-link capacitor voltage plus the capacitor equivalent series resistance (ESR) r_{c} multiplied with the capacitor current. And the average-value of the input currents of the PMSG-connected converter $i_{\mathrm{in,abc}}$ are assumed to be equal to the machine phase inductors current $i_{\mathrm{L,abc}}$. The overall resistance in each phase during on-state switching is represented

by r_{eq} which includes the generator stator resistance r_{s} and the inductor ESR r_{L}. The time derivative of the inductor currents and the DC-link capacitor voltage can be given as

$$\frac{d\langle i_{\mathrm{La}}\rangle}{dt} = \frac{1}{L_{\mathrm{s}}}\left[\langle e_{\mathrm{an}}\rangle - \langle e_{\mathrm{nN}}\rangle - d_{\mathrm{A}}\langle u_{\mathrm{o}}\rangle - r_{\mathrm{eq}}\langle i_{\mathrm{La}}\rangle\right], \tag{3.9}$$

$$\frac{d\langle i_{\mathrm{Lb}}\rangle}{dt} = \frac{1}{L_{\mathrm{s}}}\left[\langle e_{\mathrm{bn}}\rangle - \langle e_{\mathrm{nN}}\rangle - d_{\mathrm{B}}\langle u_{\mathrm{o}}\rangle - r_{\mathrm{eq}}\langle i_{\mathrm{Lb}}\rangle\right], \tag{3.10}$$

$$\frac{d\langle i_{\mathrm{Lc}}\rangle}{dt} = \frac{1}{L_{\mathrm{s}}}\left[\langle e_{\mathrm{cn}}\rangle - \langle e_{\mathrm{nN}}\rangle - d_{\mathrm{C}}\langle u_{\mathrm{o}}\rangle - r_{\mathrm{eq}}\langle i_{\mathrm{Lc}}\rangle\right], \tag{3.11}$$

$$\frac{d\langle u_{\mathrm{c}}\rangle}{dt} = \frac{1}{C_{\mathrm{dc}}}\left[d_{\mathrm{A}}\langle i_{\mathrm{La}}\rangle + d_{\mathrm{B}}\langle i_{\mathrm{Lb}}\rangle + d_{\mathrm{C}}\langle i_{\mathrm{Lc}}\rangle - \langle i_{\mathrm{o}}\rangle\right]. \tag{3.12}$$

As the state-space model of the PMSG-connected converter in abc-domain includes three-phase sinusoidal terms, it can be transformed into the dq-domain using the Park's transformation given as

$$\begin{bmatrix} x_{\mathrm{d}} \\ x_{\mathrm{q}} \\ x_{0} \end{bmatrix} = \frac{2}{3}\begin{bmatrix} \cos\theta_{\mathrm{e}} & \cos\left(\theta_{\mathrm{e}} - \frac{2\pi}{3}\right) & \cos\left(\theta_{\mathrm{e}} - \frac{4\pi}{3}\right) \\ -\sin\theta_{\mathrm{e}} & -\sin\left(\theta_{\mathrm{e}} - \frac{2\pi}{3}\right) & -\sin\left(\theta_{\mathrm{e}} - \frac{4\pi}{3}\right) \\ \frac{1}{2} & \frac{1}{2} & \frac{1}{2} \end{bmatrix} \cdot \begin{bmatrix} x_{\mathrm{a}} \\ x_{\mathrm{b}} \\ x_{\mathrm{c}} \end{bmatrix}, \tag{3.13}$$

where θ_{e} represents the electrical rotor angle that can be obtained from $\theta_{\mathrm{e}} = n_p\theta_{\mathrm{r}}$ in which n_p denotes the number of pair poles and θ_{r} the mechanical rotor angle. Under symmetrical and balanced conditions, as it is assumed in this thesis, the zero sequence of the PMSG-coupled converter in dq-domain can be neglected. Therefore, the state-space model of the three-phase sinusoidal system can be presented in dq-domain as follows:

$$\frac{d\langle i_{\mathrm{Ld}}\rangle}{dt} = \frac{1}{L_{\mathrm{d}}}\left[\langle e_{\mathrm{d}}\rangle - d_{\mathrm{d}}\langle u_{\mathrm{o}}\rangle - r_{\mathrm{eq}}\langle i_{\mathrm{Ld}}\rangle + \omega_{\mathrm{e}}L_{\mathrm{q}}\langle i_{\mathrm{Lq}}\rangle\right], \tag{3.14}$$

$$\frac{d\langle i_{\mathrm{Lq}}\rangle}{dt} = \frac{1}{L_{\mathrm{q}}}\left[\langle e_{\mathrm{q}}\rangle - d_{\mathrm{q}}\langle u_{\mathrm{o}}\rangle - r_{\mathrm{eq}}\langle i_{\mathrm{Lq}}\rangle - \omega_{\mathrm{e}}L_{\mathrm{d}}\langle i_{\mathrm{Ld}}\rangle\right], \tag{3.15}$$

$$\langle i_{\mathrm{C}}\rangle = \frac{3}{2}\left[d_{\mathrm{d}}\langle i_{\mathrm{Ld}}\rangle + d_{\mathrm{q}}\langle i_{\mathrm{Lq}}\rangle\right] - \langle i_{\mathrm{o}}\rangle, \tag{3.16}$$

$$\frac{d\langle u_{\mathrm{C}}\rangle}{dt} = \frac{1}{C_{\mathrm{dc}}}\left[\frac{3}{2}\left(d_{\mathrm{d}}\langle i_{\mathrm{Ld}}\rangle + d_{\mathrm{q}}\langle i_{\mathrm{Lq}}\rangle\right) - \langle i_{\mathrm{o}}\rangle\right], \tag{3.17}$$

where ω_{e} denotes the electrical angular frequency. Substituting (3.16) into (3.5), the output voltage can be expressed by

$$\langle u_{\mathrm{o}}\rangle = \frac{3}{2}r_{\mathrm{C}}\,d_{\mathrm{d}}\langle i_{\mathrm{Ld}}\rangle + \frac{3}{2}r_{\mathrm{C}}\,d_{\mathrm{q}}\langle i_{\mathrm{Lq}}\rangle - r_{\mathrm{C}}\langle i_{\mathrm{o}}\rangle + \langle u_{\mathrm{C}}\rangle \tag{3.18}$$

The three-phase input current $i_{\mathrm{in(a,b,c)}}$ can be described in the dq-domain as

$$\langle i_{\mathrm{ind}}\rangle = \langle i_{\mathrm{Ld}}\rangle, \tag{3.19}$$

$$\langle i_{\mathrm{inq}}\rangle = \langle i_{\mathrm{Lq}}\rangle, \tag{3.20}$$

Substituting (3.18) into (3.14) and (3.15), the average-valued equations in the rotor reference frame can be given as

$$\frac{d\langle i_{\mathrm{Ld}}\rangle}{dt}=\frac{1}{L_{\mathrm{d}}}\Big[\langle e_{\mathrm{d}}\rangle-\Big(r_{\mathrm{eq}}+\frac{3}{2}r_{\mathrm{C}}d_{\mathrm{d}}^{2}\Big)\langle i_{\mathrm{Ld}}\rangle-\Big(-\omega_{\mathrm{e}}L_{\mathrm{q}}+\frac{3}{2}r_{\mathrm{C}}d_{\mathrm{d}}d_{\mathrm{q}}\Big)\langle i_{\mathrm{Lq}}\rangle+r_{\mathrm{C}}d_{\mathrm{d}}\langle i_{\mathrm{o}}\rangle - d_{\mathrm{d}}\langle u_{\mathrm{C}}\rangle\Big], \tag{3.21}$$

$$\frac{d\langle i_{\mathrm{Lq}}\rangle}{dt}=\frac{1}{L_{\mathrm{q}}}\Big[\langle e_{\mathrm{q}}\rangle-\Big(r_{\mathrm{eq}}+\frac{3}{2}r_{\mathrm{C}}d_{\mathrm{q}}^{2}\Big)\langle i_{\mathrm{Lq}}\rangle-\Big(\omega_{\mathrm{e}}L_{\mathrm{d}}+\frac{3}{2}r_{\mathrm{C}}d_{\mathrm{d}}d_{\mathrm{q}}\Big)\langle i_{\mathrm{Ld}}\rangle+r_{\mathrm{C}}d_{\mathrm{q}}\langle i_{\mathrm{o}}\rangle - d_{\mathrm{q}}\langle u_{\mathrm{C}}\rangle\Big], \tag{3.22}$$

$$\frac{d\langle u_{\mathrm{C}}\rangle}{dt}=\frac{1}{C_{\mathrm{dc}}}\Big[\frac{3}{2}\,d_{\mathrm{d}}\,\langle i_{\mathrm{Ld}}\rangle+\frac{3}{2}\,d_{\mathrm{q}}\,\langle i_{\mathrm{Lq}}\rangle-\langle i_{\mathrm{o}}\rangle\Big], \tag{3.23}$$

$$\langle i_{\mathrm{ind}}\rangle=\langle i_{\mathrm{Ld}}\rangle, \tag{3.24}$$

$$\langle i_{\mathrm{inq}}\rangle=\langle i_{\mathrm{Lq}}\rangle, \tag{3.25}$$

$$\langle u_{\mathrm{o}}\rangle=\Big(1+r_{\mathrm{C}}C_{\mathrm{dc}}\frac{d}{dt}\Big)\langle u_{\mathrm{C}}\rangle. \tag{3.26}$$

3.2 Steady-state operating point

As the average-valued model of the PMSG-connected converter is non-linear with respect to the duty ratios, it must be linearized around a steady-state operating point so that the dynamic model can be obtained. Since in steady-state condition derivatives are zero, the averaged model equations (3.21)-(3.26) can be used to derive the steady-state operating point equations by putting the derivatives be zero in which the upper case letters are used to show the steady-state values. Hence, the steady-state operating point equations can be given as

$$\frac{1}{L_{\mathrm{d}}}E_{\mathrm{d}}-\Big(\frac{r_{\mathrm{eq}}}{L_{\mathrm{d}}}+\frac{3}{2}\frac{r_{\mathrm{C}}D_{\mathrm{d}}^{2}}{L_{\mathrm{d}}}\Big)I_{\mathrm{Ld}}-\Big(\frac{3}{2}\frac{r_{\mathrm{C}}D_{\mathrm{d}}D_{\mathrm{q}}}{L_{\mathrm{d}}}-\omega_{\mathrm{e}}\frac{L_{\mathrm{q}}}{L_{\mathrm{d}}}\Big)I_{\mathrm{Lq}}+\frac{r_{\mathrm{C}}D_{\mathrm{d}}}{L_{\mathrm{d}}}I_{\mathrm{o}}-\frac{D_{\mathrm{d}}}{L_{\mathrm{d}}}U_{\mathrm{C}}=0, \tag{3.25}$$

$$\frac{1}{L_{\mathrm{q}}}E_{\mathrm{q}}-\Big(\frac{r_{\mathrm{eq}}}{L_{\mathrm{q}}}+\frac{3}{2}\frac{r_{\mathrm{C}}D_{\mathrm{q}}^{2}}{L_{\mathrm{q}}}\Big)I_{\mathrm{Lq}}-\Big(\frac{3}{2}\frac{r_{\mathrm{C}}D_{\mathrm{d}}D_{\mathrm{q}}}{L_{\mathrm{q}}}+\omega_{\mathrm{e}}\frac{L_{\mathrm{d}}}{L_{\mathrm{q}}}\Big)I_{\mathrm{Ld}}+\frac{r_{\mathrm{C}}D_{\mathrm{q}}}{L_{\mathrm{q}}}I_{\mathrm{o}}-\frac{D_{\mathrm{q}}}{L_{\mathrm{q}}}U_{\mathrm{C}}=0, \tag{3.26}$$

$$\frac{3}{2}\frac{D_{\mathrm{d}}}{C_{\mathrm{dc}}}I_{\mathrm{Ld}}+\frac{3}{2}\frac{D_{\mathrm{q}}}{C_{\mathrm{dc}}}I_{\mathrm{Lq}}-\frac{1}{C_{\mathrm{dc}}}I_{\mathrm{o}}=0, \tag{3.27}$$

$$U_{\mathrm{o}}=U_{\mathrm{C}}, \tag{3.28}$$

$$I_{\mathrm{ind}}=I_{\mathrm{Ld}}, \tag{3.29}$$

$$I_{\mathrm{inq}}=I_{\mathrm{Lq}}. \tag{3.30}$$

Assuming no saliency in the PMSG, which is a good approximation in case of utilizing a large surface-mounted PMSG, the inductances in both dq-channels can be assumed to be equal $(L_{\mathrm{d}}\approx L_{\mathrm{q}})$ thus in the rest of this thesis the machine inductance will be shown by L. Since the maximum torque per ampere control strategy is used in this thesis, by making the d-component stator current equal to zero, the electromagnetic torque of the PMSG will be entirely controlled through the q-component stator current. Therefore, as presented by

$$I_{\mathrm{Ld}}=0, \tag{3.31}$$

the steady-state value for the d-channel inductor current is equal to zero.

Moreover, the vector control of PMSG-connected boost converter highly relies on the rotor position and as the sensorless vector control is not part of this study, it is assumed that a position transducer is used to obtain the reference angle of the generator and the error angle is not considered into the model. Therefore, it can be assumed that the back-EMF is aligned with the q-axis and the d-axis back-EMF is equal to zero as expressed by

$$E_{\mathrm{d}} = 0. \tag{3.32}$$

By substituting (3.31) into (3.27), the operating point of the PMSG stator current for the q-component can be given as

$$I_{\mathrm{Lq}} = \frac{I_{\mathrm{o}}}{\frac{3}{2}D_{\mathrm{q}}}, \tag{3.33}$$

By substituting (3.31) and (3.33) in (3.26), the duty ratio of the q-component can be obtained as follows

$$D_{\mathrm{q}}^2 U_{\mathrm{o}} - D_{\mathrm{q}} E_{\mathrm{q}} + \frac{2}{3} r_{\mathrm{eq}} I_{\mathrm{o}} = 0, \tag{3.34}$$

and by solving (3.34), D_{q} can be given as

$$D_{\mathrm{q}} = \frac{E_{\mathrm{q}} \pm \sqrt{E_{\mathrm{q}}^2 - \left(\frac{8}{3} r_{\mathrm{eq}} U_{\mathrm{o}} I_{\mathrm{o}}\right)}}{2U_{\mathrm{o}}}. \tag{3.35}$$

By substituting (3.35) in (3.33), the operating point value of I_{Lq} can be obtained as

$$I_{\mathrm{Lq}} = \frac{4}{3} \frac{U_{\mathrm{o}} I_{\mathrm{o}}}{E_{\mathrm{q}} \pm \sqrt{E_{\mathrm{q}}^2 - \left(\frac{8}{3} r_{\mathrm{eq}} U_{\mathrm{o}} I_{\mathrm{o}}\right)}}. \tag{3.36}$$

Finally, by substituting (3.31), (3.32) and (3.36) in (3.25), D_{d} can be obtained as

$$D_{\mathrm{d}} = \frac{2}{3} \frac{\omega_{\mathrm{e}} L I_{\mathrm{o}}}{D_{\mathrm{q}} U_{\mathrm{o}}} = \frac{4}{3} \frac{\omega_{\mathrm{e}} L I_{\mathrm{o}}}{E_{\mathrm{q}} \pm \sqrt{E_{\mathrm{q}}^2 - \left(\frac{8}{3} r_{\mathrm{eq}} U_{\mathrm{o}} I_{\mathrm{o}}\right)}}. \tag{3.37}$$

3.3 Small-signal model

Now that the steady-state values for the PMSG-connected converter are obtained, the model can be linearized by first-order partial derivatives for the input, the state and the output variables presented by $(e_{\mathrm{d}}, e_{\mathrm{q}}, i_{\mathrm{o}}, d_{\mathrm{d}}, d_{\mathrm{q}})$, $(i_{\mathrm{Ld}}, i_{\mathrm{Lq}}, u_{\mathrm{C}})$, $(i_{\mathrm{ind}}, i_{\mathrm{inq}}, u_{\mathrm{o}})$ respectively.

$$\frac{d\hat{\imath}_{\mathrm{Ld}}}{dt} = -\left(\frac{r_{\mathrm{eq}}}{L} + \frac{3}{2}\frac{r_{\mathrm{C}}D_{\mathrm{d}}^2}{L}\right)\hat{\imath}_{\mathrm{Ld}} + \left(\omega_{\mathrm{e}} - \frac{3}{2}\frac{r_{\mathrm{C}}D_{\mathrm{d}}D_{\mathrm{q}}}{L}\right)\hat{\imath}_{\mathrm{Lq}} + I_{\mathrm{Lq}}\hat{\omega}_{\mathrm{e}} + \frac{1}{L}\hat{e}_{\mathrm{d}} - \frac{D_{\mathrm{d}}}{L}\hat{u}_{\mathrm{C}} + \frac{r_{\mathrm{C}}D_{\mathrm{d}}}{L}\hat{\imath}_{\mathrm{o}} + \frac{1}{L}\left(r_{\mathrm{C}}I_{\mathrm{o}} - \frac{3}{2}r_{\mathrm{C}}D_{\mathrm{q}}I_{\mathrm{Lq}} - 3r_{\mathrm{C}}D_{\mathrm{d}}I_{\mathrm{Ld}} - U_{\mathrm{o}}\right)\hat{d}_{\mathrm{d}} - \left(\frac{3}{2}\frac{r_{\mathrm{C}}D_{\mathrm{d}}I_{\mathrm{Lq}}}{L}\right)\hat{d}_{\mathrm{q}} \tag{3.38}$$

$$\frac{d\hat{\imath}_{\mathrm{Lq}}}{dt} = -\left(\omega_{\mathrm{e}} + \frac{3}{2}\frac{r_{\mathrm{C}}D_{\mathrm{d}}D_{\mathrm{q}}}{L}\right)\hat{\imath}_{\mathrm{Ld}} - I_{\mathrm{Ld}}\hat{\omega}_{\mathrm{e}} - \left(\frac{r_{\mathrm{eq}}}{L} + \frac{3}{2}\frac{r_{\mathrm{C}}D_{\mathrm{q}}^2}{L}\right)\hat{\imath}_{\mathrm{Lq}} + \frac{1}{L}\hat{e}_{\mathrm{q}} - \frac{D_{\mathrm{q}}}{L}\hat{u}_{\mathrm{C}} + \frac{r_{\mathrm{C}}D_{\mathrm{q}}}{L}\hat{\imath}_{\mathrm{o}} - \left(\frac{3}{2}\frac{r_{\mathrm{C}}D_{\mathrm{q}}I_{\mathrm{Ld}}}{L}\right)\hat{d}_{\mathrm{d}} + \frac{1}{L}\left(r_{\mathrm{C}}I_{\mathrm{o}} - \frac{3}{2}r_{\mathrm{C}}D_{\mathrm{d}}I_{\mathrm{Ld}} - 3r_{\mathrm{C}}D_{\mathrm{q}}I_{\mathrm{Lq}} - U_{\mathrm{o}}\right)\hat{d}_{\mathrm{q}} \tag{3.39}$$

$$\frac{d\hat{u}_{\mathrm{C}}}{dt} = \frac{3}{2}\frac{D_{\mathrm{d}}}{C_{\mathrm{dc}}}\hat{\imath}_{\mathrm{Ld}} + \frac{3}{2}\frac{D_{\mathrm{q}}}{C_{\mathrm{dc}}}\hat{\imath}_{\mathrm{Lq}} - \frac{1}{C_{\mathrm{dc}}}\hat{\imath}_{\mathrm{o}} + \frac{3}{2}\frac{I_{\mathrm{Ld}}}{C_{\mathrm{dc}}}\hat{d}_{\mathrm{d}} + \frac{3}{2}\frac{I_{\mathrm{Lq}}}{C_{\mathrm{dc}}}\hat{d}_{\mathrm{q}} \tag{3.40}$$

$$\hat{u}_{\mathrm{o}} = \left(1 + r_{\mathrm{C}}C_{\mathrm{dc}}\frac{d}{dt}\right)\hat{u}_{\mathrm{C}} \tag{3.41}$$

$$\hat{\imath}_{\mathrm{ind}} = \hat{\imath}_{\mathrm{Ld}} \tag{3.42}$$

$$\hat{\imath}_{\mathrm{inq}} = \hat{\imath}_{\mathrm{Lq}} \tag{3.43}$$

Considering $e_{\mathrm{q}} = \omega_{\mathrm{e}}\lambda_{\mathrm{m}}$, if the flux of the permanent magnets taken as a constant parameter, $\hat{e}_{\mathrm{q}} = \hat{\omega}_{\mathrm{e}}\lambda_{\mathrm{m}}$ thus in (3.38) and (3.39) $\hat{\omega}_{\mathrm{e}}$ can be substituted by $\hat{e}_{\mathrm{q}}/\lambda_{\mathrm{m}}$. Hence, the small-signal model of the PMSG-connected converter can be expressed as

$$\frac{d\hat{\imath}_{\mathrm{Ld}}}{dt} = -\left(\frac{r_{\mathrm{eq}}}{L} + \frac{3}{2}\frac{r_{C}D_{d}^2}{L}\right)\hat{\imath}_{\mathrm{Ld}} + \omega_{\mathrm{e}}\left(1 - \frac{r_{C}I_{\mathrm{o}}}{U_{\mathrm{o}}}\right)\hat{\imath}_{\mathrm{Lq}} + \frac{I_{\mathrm{Lq}}}{\lambda_{\mathrm{m}}}\hat{e}_{\mathrm{q}} + \frac{1}{L}\hat{e}_{\mathrm{d}} - \frac{D_{\mathrm{d}}}{L}\hat{u}_{\mathrm{C}} + \frac{r_{\mathrm{C}}D_{\mathrm{d}}}{L}\hat{\imath}_{\mathrm{o}} - \frac{1}{L}U_{\mathrm{o}}\hat{d}_{\mathrm{d}} - \frac{3}{2}\left(\frac{r_{\mathrm{C}}\omega_{\mathrm{e}}I_{\mathrm{o}}^2}{D_{\mathrm{q}}^2U_{\mathrm{o}}}\right)\hat{d}_{\mathrm{q}} \tag{3.44}$$

$$\frac{d\hat{\imath}_{\mathrm{Lq}}}{dt} = -\omega_{\mathrm{e}}\left(1 + \frac{r_{\mathrm{C}}I_{\mathrm{o}}}{U_{\mathrm{o}}}\right)\hat{\imath}_{\mathrm{Ld}} - \left(\frac{r_{\mathrm{eq}}}{L} + \frac{3}{2}\frac{r_{\mathrm{C}}D_{\mathrm{q}}^2}{L}\right)\hat{\imath}_{\mathrm{Lq}} - \frac{I_{\mathrm{Ld}}}{\lambda_{\mathrm{m}}}\hat{e}_{\mathrm{d}} + \frac{1}{L}\hat{e}_{\mathrm{q}} - \frac{D_{\mathrm{q}}}{L}\hat{u}_{\mathrm{C}} + \frac{r_{\mathrm{C}}D_{\mathrm{q}}}{L}\hat{\imath}_{\mathrm{o}} - \frac{1}{L}(U_{\mathrm{o}} + r_{\mathrm{C}}I_{\mathrm{o}})\hat{d}_{\mathrm{q}} \tag{3.45}$$

$$\frac{d\hat{u}_{\mathrm{C}}}{dt} = \frac{3}{2}\frac{D_{\mathrm{d}}}{C_{\mathrm{dc}}}\hat{\imath}_{\mathrm{Ld}} + \frac{3}{2}\frac{D_{\mathrm{q}}}{C_{\mathrm{dc}}}\hat{\imath}_{\mathrm{Lq}} - \frac{1}{C_{\mathrm{dc}}}\hat{\imath}_{\mathrm{o}} + \frac{I_{\mathrm{o}}}{C_{\mathrm{dc}}D_{\mathrm{q}}}\hat{d}_{\mathrm{q}} \tag{3.46}$$

The linearized state-space equations presented in (3.44) – (3.46) can be written using matrices as follows

$$\frac{d\hat{x}(t)}{dt} = \mathbf{A}\hat{x}(t) + \mathbf{B}\hat{u}(t), \tag{3.47}$$

$$\hat{y}(t) = \mathbf{C}\hat{x}(t) + \mathbf{D}\hat{u}(t), \tag{3.48}$$

where the state, input and output variable vectors are defined as

$$\hat{x} = \left[\hat{\imath}_{\mathrm{Ld}}\ \hat{\imath}_{\mathrm{Lq}}\ \hat{u}_{\mathrm{C}}\right]^{\mathrm{T}},\quad \hat{u} = \left[\hat{e}_{\mathrm{d}}\ \hat{e}_{\mathrm{q}}\ \hat{\imath}_{\mathrm{o}}\ \hat{d}_{\mathrm{d}}\ \hat{d}_{\mathrm{q}}\right]^{\mathrm{T}},\quad \hat{y} = \left[\hat{\imath}_{\mathrm{ind}}\ \hat{\imath}_{\mathrm{inq}}\ \hat{u}_{\mathrm{o}}\right]^{\mathrm{T}}, \tag{3.49}$$

and the state matrices $\mathbf{A}$, $\mathbf{B}$, $\mathbf{C}$ and $\mathbf{D}$ are defined as

$$\mathbf{A}=\begin{bmatrix} -\left(\frac{r_{\mathrm{eq}}}{L}+\frac{3}{2}\frac{r_{\mathrm{C}}D_{\mathrm{d}}^2}{L}\right) & \omega_{\mathrm{e}}\left(1-\frac{r_{\mathrm{C}}I_{\mathrm{o}}}{U_{\mathrm{o}}}\right) & -\frac{D_{\mathrm{d}}}{L} \\ -\omega_{\mathrm{e}}\left(1+\frac{r_{\mathrm{C}}I_{\mathrm{o}}}{U_{\mathrm{o}}}\right) & -\left(\frac{r_{\mathrm{eq}}}{L}+\frac{3}{2}\frac{r_{\mathrm{C}}D_{\mathrm{q}}^2}{L}\right) & -\frac{D_{\mathrm{q}}}{L} \\ \frac{3}{2}\frac{D_{\mathrm{d}}}{C} & \frac{3}{2}\frac{D_{\mathrm{q}}}{C} & 0 \end{bmatrix},\quad \mathbf{C}=\begin{bmatrix} 0 & 0 & 1+r_{\mathrm{C}}C_{\mathrm{dc}}\frac{d}{dt} \\ 1 & 0 & 0 \\ 0 & 1 & 0 \end{bmatrix},$$

$$\mathbf{B}=\begin{bmatrix} \frac{1}{L} & \frac{I_{\mathrm{Lq}}}{\lambda_{\mathrm{m}}} & \frac{r_{\mathrm{C}}D_{\mathrm{d}}}{L} & -\frac{U_{\mathrm{o}}}{L} & -\frac{3}{2}\left(\frac{r_{\mathrm{C}}\omega_{\mathrm{e}}I_{\mathrm{o}}^2}{D_{\mathrm{q}}^2U_{\mathrm{o}}}\right) \\ 0 & \frac{1}{L} & \frac{r_{\mathrm{C}}D_{\mathrm{q}}}{L} & 0 & -\frac{U_{\mathrm{o}}+r_{\mathrm{C}}I_{\mathrm{o}}}{L} \\ 0 & 0 & -\frac{1}{C_{\mathrm{dc}}} & 0 & \frac{I_{\mathrm{o}}}{C_{\mathrm{dc}}D_{\mathrm{q}}} \end{bmatrix},\qquad \mathbf{D}=0. \tag{3.50}$$

The linearized time-domain state-space expressed in (3.47) and (3.48) can be transformed into the Laplace domain where relationship between the input variables $\mathbf{U}(s)$ and the output variables $\mathbf{Y}(s)$ can be calculated as presented in (3.51) - (3.54).

$$s\boldsymbol{X}(s)=\mathbf{A}\boldsymbol{X}(s)+\mathbf{B}\boldsymbol{U}(s) \tag{3.51}$$
$$\boldsymbol{Y}(s)=\mathbf{C}\boldsymbol{X}(s)+\mathbf{D}\boldsymbol{U}(s) \tag{3.52}$$
$$\boldsymbol{X}(s)=(s\mathbf{I}-\mathbf{A})^{-1}\mathbf{B}\boldsymbol{U}(s) \tag{3.53}$$
$$\boldsymbol{Y}(s)=[\mathbf{C}(s\mathbf{I}-\mathbf{A})^{-1}\mathbf{B}+\mathbf{D}]\,\boldsymbol{U}(s)=\mathbf{G}\boldsymbol{U}(s) \tag{3.54}$$

Consequently, 15 transfer functions can be found in matrix $\mathbf{G}$ as

$$\begin{bmatrix} \hat{\imath}_{\mathrm{ind}} \\ \hat{\imath}_{\mathrm{inq}} \\ \hat{u}_{\mathrm{o}} \end{bmatrix}=\begin{bmatrix} Y_{\mathrm{in-d}} & G_{\mathrm{cr-qd}} & T_{\mathrm{oi-d}} & G_{\mathrm{ci-d}} & G_{\mathrm{ci-qd}} \\ G_{\mathrm{cr-dq}} & Y_{\mathrm{in-q}} & T_{\mathrm{oi-q}} & G_{\mathrm{ci-dq}} & G_{\mathrm{ci-q}} \\ G_{\mathrm{io-d}} & G_{\mathrm{io-q}} & -Z_{\mathrm{o}} & G_{\mathrm{co-d}} & G_{\mathrm{co-q}} \end{bmatrix}\begin{bmatrix} \hat{e}_{\mathrm{d}} \\ \hat{e}_{\mathrm{q}} \\ \hat{\imath}_{\mathrm{o}} \\ \hat{d}_{\mathrm{d}} \\ \hat{d}_{\mathrm{q}} \end{bmatrix}, \tag{3.55}$$

in which the dynamics of the PMSG-connected converter are represented by the transfer functions.

To simplify the calculation, the parasitic resistances of the converter including the stator resistance are neglected at this stage. Therefore, the input admittances Y_{in} and the cross-coupling G_{cr} transfer functions can be given as

$$Y_{\mathrm{in-d}}=\frac{\hat{\imath}_{\mathrm{ind}}}{\hat{e}_{\mathrm{d}}}=\frac{1}{L}\left(s^2+\frac{3}{2}\frac{D_{\mathrm{q}}^2}{LC_{\mathrm{dc}}}\right)\frac{1}{\Delta}, \tag{3.55}$$
$$Y_{\mathrm{in-q}}=\frac{\hat{\imath}_{\mathrm{inq}}}{\hat{e}_{\mathrm{q}}}=\frac{1}{L}\left(s-\frac{\omega_{\mathrm{e}}LI_{\mathrm{Lq}}}{\lambda_{\mathrm{m}}}\right)\frac{s}{\Delta}, \tag{3.56}$$
$$G_{\mathrm{cr-qd}}=\frac{\hat{\imath}_{\mathrm{ind}}}{\hat{e}_{\mathrm{q}}}=\frac{I_{\mathrm{Lq}}}{\lambda_{\mathrm{m}}}\left(s+\frac{E_{\mathrm{q}}}{LI_{\mathrm{Lq}}}\right)\frac{s}{\Delta}, \tag{3.57}$$
$$G_{\mathrm{cr-dq}}=\frac{\hat{\imath}_{\mathrm{inq}}}{\hat{e}_{\mathrm{d}}}=-\frac{\omega_{\mathrm{e}}}{L}\left(s+\frac{I_{\mathrm{o}}}{C_{\mathrm{dc}}U_{\mathrm{o}}}\right)\frac{1}{\Delta}. \tag{3.58}$$

The transfer functions between the control variables $(d_{\mathrm{d}}, d_{\mathrm{q}})$ and input currents $(i_{\mathrm{ind}}, i_{\mathrm{inq}})$ shown by G_{ci} can be given by

$$G_{\mathrm{ci-d}} = \frac{\hat{\imath}_{\mathrm{ind}}}{\hat{d}_{\mathrm{d}}} = -\frac{U_{\mathrm{o}}}{L}\left(s^2 + \frac{3}{2}\frac{D_{\mathrm{q}}^2}{LC_{\mathrm{dc}}}\right)\frac{1}{\Delta} \quad , \tag{3.59}$$

$$G_{\mathrm{ci-q}} = \frac{\hat{\imath}_{\mathrm{inq}}}{\hat{d}_{\mathrm{q}}} = -\frac{U_{\mathrm{o}}}{L}\left(s + \frac{I_{\mathrm{o}}}{C_{\mathrm{dc}}U_{\mathrm{o}}}\right)\frac{s}{\Delta} \quad , \tag{3.60}$$

$$G_{\mathrm{ci-dq}} = \frac{\hat{\imath}_{\mathrm{inq}}}{\hat{d}_{\mathrm{d}}} = \frac{U_o\omega_{\mathrm{e}}}{L}\left(s + \frac{I_o}{C_{\mathrm{dc}}U_o}\right)\frac{1}{\Delta} \, , \tag{3.61}$$

$$G_{\mathrm{ci-qd}} = \frac{\hat{\imath}_{\mathrm{ind}}}{\hat{d}_{\mathrm{q}}} = -\left(\frac{U_{\mathrm{o}}\omega_{\mathrm{e}}}{L} + \frac{2}{3}\frac{\omega_{\mathrm{e}}I_{\mathrm{o}}^2}{D_{\mathrm{q}}^2C_{\mathrm{dc}}U_{\mathrm{o}}}\right)\frac{s^2}{\Delta} \, . \tag{3.62}$$

The output impedance of the PMSG-connected converter Z_{o} can be given by

$$Z_{\mathrm{o}} = \frac{\hat{u}_{\mathrm{o}}}{\hat{\imath}_{\mathrm{o}}} = \frac{1}{C_{\mathrm{dc}}}\,(s^2 + \omega_{\mathrm{e}}^2)\frac{1}{\Delta} \, . \tag{3.63}$$

The transfer functions between the output voltage u_{o} and the control variables $(d_{\mathrm{d}}\,, d_{\mathrm{q}})$ presented by G_{co}, can be expressed by

$$G_{\mathrm{co-d}} = \frac{\hat{u}_{\mathrm{o}}}{\hat{d}_{\mathrm{d}}} = -\frac{3}{2}\frac{\omega_{\mathrm{e}}I_{\mathrm{Lq}}}{C_{\mathrm{dc}}}\left(s - \frac{E_{\mathrm{q}}}{LI_{\mathrm{Lq}}}\right)\frac{1}{\Delta} \, , \tag{3.64}$$

$$G_{\mathrm{co-q}} = \frac{\hat{u}_{\mathrm{o}}}{\hat{d}_{\mathrm{q}}} = \frac{3}{2}\frac{I_{\mathrm{Lq}}}{C_{\mathrm{dc}}}\left(s - \frac{E_{\mathrm{q}}}{LI_{\mathrm{Lq}}}\right)\frac{s}{\Delta} \, . \tag{3.65}$$

The denominator of the transfer functions indicated by Δ can be given as

$$\Delta = s\left(s^2 + \frac{3}{2}\frac{D_{\mathrm{d}}^2 + D_{\mathrm{q}}^2}{LC_{\mathrm{dc}}} + \omega_{\mathrm{e}}^2\right). \tag{3.66}$$

The resonant behaviour of the PMSG-connected converter can be realized from the determinant Δ which has a duty ratio dependant resonance. Moreover, as the roots of the denominator introduce the system poles, it can be found that the PMSG-connected converter is stable for all the operating points as the determinant does not contain any roots with positive real part. In the input admittance of the q-channel $Y_{\mathrm{in-q}}$, one real RHP-zero can be observed which is dependent on the operating point. The effect of this RHP-zero on the stability of the interconnected system will be discussed later. However, it is worth mentioning that the zero introduces negative resistor-like behaviour in the low frequency for the converter that can lead to instability when the drive-train model is considered. The control-to-input current transfer function $G_{\mathrm{ci-q}}$ has no RHP-zero. Hence, in case of current control, there will be no design constraints while $G_{\mathrm{co-q}}$ contains a RHP-zero which is dependent on the operating point and imposes bandwidth limitation in case of controlling the output variable. In the next chapter, the dynamic model of the PMSG-connected converter derived in this part will be used to design the current and output voltage controllers.

4. WIND TURBINE CONTROL

As shortly explained in Chapter 1, the typical control strategies in the DDPMSG-based WECSs can be divided into the two main structures, the conventional control scheme, and the alternative control strategy. In the former, the machine-side converter, which is called the PMSG-connected converter in this study, is utilized to control the active power delivery to the grid where the reference active power is determined either based on the maximum power point tracker (MPPT) or the controlled power (CP) assigned by the supervisory control. The power control can be applied via the PMSG torque control. In this control strategy, the grid-connected inverter is responsible to regulate the DC-link voltage where it can be applied through the inverter output current. In the alternative control scheme, the function of the PMSG-connected converter and the grid-connected inverter are switched. Hence, the former one is responsible for regulating the DC-link voltage via controlling the PMSG torque and the latter can be used to control the power delivery to the grid through the controlling the inverter output current. In this thesis, the alternative control scheme is employed for the WECS control.

In this chapter, the current controllers are designed for the PMSG-connected converter based on the open-loop transfer functions obtained in the previous chapter and design guidelines for a stable DC-link voltage control loop are expressed.

4.1 Generator-side converter control

The control strategy utilized for the generator-side converter in this thesis is illustrated in Figure 5. As can be seen, the control scheme consists of a cascaded control scheme in which the inner loops are the current controllers and the outer loop is the DC-link voltage controller. Since the alternative control scheme is employed for the WECS, the PMSG-connected converter is used to control the DC-link voltage. Therefore, the reference torque is obtained from the DC-link voltage controller. In the following, the dynamic model of the PMSG-connected converter is used for designing the control loops.

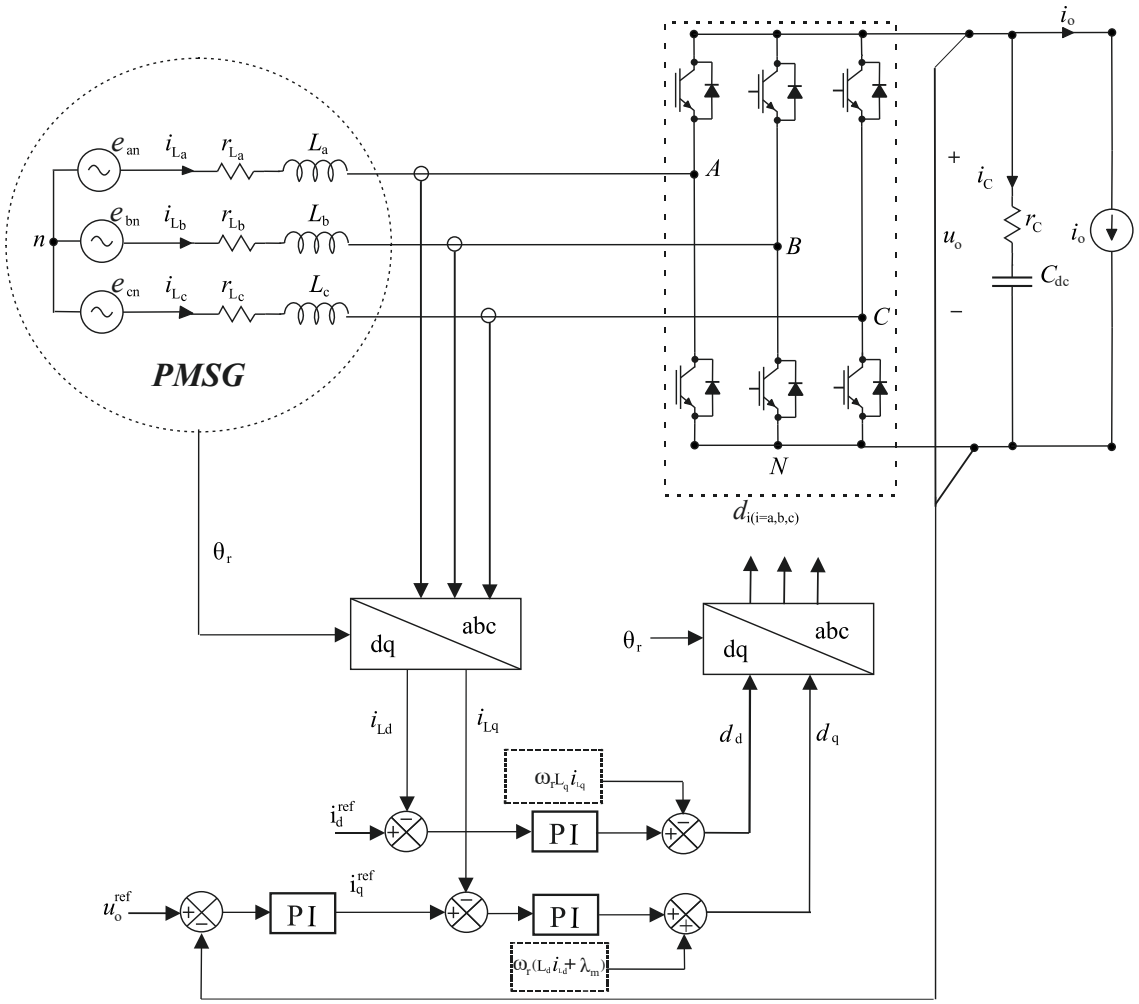

***Figure 5**. Control diagram for the alternative control structure*

4.1.1 PMSG torque control

Different strategies can be applied to the PMSG-connected converter to control the electromagnetic torque. In this work, the maximum torque per ampere control scheme is applied where the electromagnetic torque of the PMSG can be given as

$$T_{\mathrm{g}} = \frac{3}{2} n_{\mathrm{p}} \left[\lambda_{\mathrm{m}} + (L_{\mathrm{d}} - L_{\mathrm{q}}) i_{\mathrm{d}}\right] i_{\mathrm{q}} \,. \tag{4.1}$$

However, as explained in the previous chapter in surface-mounted PMSGs the d-and q-axis of stator inductance can be taken equal $L_{\mathrm{d}} \approx L_{\mathrm{q}}$. Therefore, the electromagnetic torque reduces to

$$T_{\mathrm{g}} = n_{\mathrm{p}} \lambda_{\mathrm{m}} i_{\mathrm{q}} \,. \tag{4.2}$$

Hence, the electromagnetic torque can be controlled only through the control-to-inductor current of the q-axis of the PMSG-connected converter $G_{\mathrm{ci-q}}$. As the plant transfer function in this case $G_{\mathrm{ci-q}}$ does not contain any RHP-zeros, there will be no control design

constraints imposed by the dynamic behaviour of the control-to- inductor current. However, it can be realized from the transfer function that it has negative sign which means that the phase angle starts from 180°. Hence, the current controller must be inverted. Furthermore, the denominator of control-to-inductor current contains an operating point dependent term which has to be considered in designing the controller. Using Loop-shaping technique, the current controller can be tuned. The structure of the current controller used in here can be given as

$$G_{\mathrm{cc}} = K_{\mathrm{c}} \frac{\left(\frac{s}{\omega_{\mathrm{zc}}} + 1\right)}{s\left(\frac{s}{\omega_{\mathrm{pc}}} + 1\right)}, \tag{4.3}$$

where ω_{zc} represents the angular frequency of the controller zero and K_{c} is the controller gain. ω_{pc} denotes the angular frequency of the controller pole that is used to attenuate the high-frequency noises caused by switching network.

Since there exists no RHP-zero in the plant transfer function, the bandwidth of the current control loop is only dependent on the angular switching frequency of the converter. It is worth noting that the deadtime, which includes the model of the controller computational delay and the Pulse Width Modulation switching, can impose limitation on the bandwidth of the current control loop. In [26], it is reported that a high bandwidth can cause instability in case of a salient PMSG regulated with a current controlled voltage-source-converter. However, in this thesis, the deadtime is not included in the PMSG-connected converter model because the focus is on the low frequency instabilities caused by mechanical dynamics and a round PMSG is considered.

The current control loop of the PMSG-connected converter requires to meet the following criteria:

- The bandwidth of the control loop must be high enough so that the electrical dynamics can be decoupled from the mechanical dynamics of the wind turbine. It is recommended that current control loop bandwidth should be ten times faster than the DC-link voltage loop.
- The current control loop must have a good stability margins which can be obtained by achieving at least gain margin = 6 and phase margin = 40°.
- The percentage overshoot of the closed-loop current control should be less than 20%.
- It is recommended that the current control loop bandwidth is designed to be smaller than $0.2\omega_{\mathrm{sw}}$, where ω_{sw} is the switching frequency (rad/s) [27].

The current control loops can be presented based on the block diagrams shown in Figure 6.

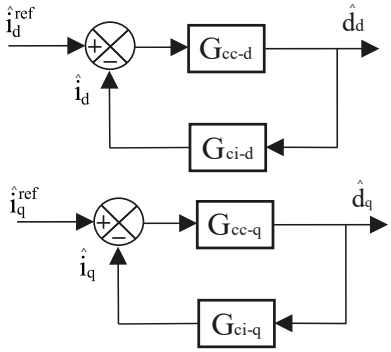

***Figure 6**. Control-block diagram for current control loops*

In which $\hat{\imath}_{\mathrm{ref-d}}$ and $\hat{\imath}_{\mathrm{ref-q}}$ represent the d-channel current reference and the q-channel current reference, respectively. And the controllers can be expressed as

$$G_{\mathrm{cc-d}} = K_{\mathrm{cd}} \frac{\left(\frac{s}{\omega_{\mathrm{zc-d}}} + 1\right)}{s\left(\frac{s}{\omega_{\mathrm{pc-d}}} + 1\right)}, \tag{4.4}$$

$$G_{\mathrm{cc-q}} = K_{\mathrm{cq}} \frac{\left(\frac{s}{\omega_{\mathrm{zc-q}}} + 1\right)}{s\left(\frac{s}{\omega_{\mathrm{pc-q}}} + 1\right)}, \tag{4.5}$$

where $G_{\mathrm{cc-d}}$ denote the current controller for the d-channel and $G_{\mathrm{cc-q}}$ indicates the q-channel current controller. According to the control diagram presented in Figure 6, the current loop gains and the closed-loop transfer functions of the current control can be obtained as

$$\begin{aligned} L_{\mathrm{in-d}} &= G_{\mathrm{cc-d}}\, G_{\mathrm{ci-d}} \\ L_{\mathrm{in-q}} &= G_{\mathrm{cc-q}}\, G_{\mathrm{ci-q}} \end{aligned}, \tag{4.6}$$

$$\frac{\hat{i}_{\mathrm{d}}}{\hat{i}_{\mathrm{ref-d}}} = \frac{L_{\mathrm{in-d}}}{1 + L_{\mathrm{in-d}}}, \qquad \frac{\hat{i}_{\mathrm{q}}}{\hat{i}_{\mathrm{ref-q}}} = \frac{L_{\mathrm{in-q}}}{1 + L_{\mathrm{in-q}}}. \tag{4.7}$$

Applying the control design criteria explained earlier, the current control loop gain and the closed-loop current control for the q-channel are illustrated in Figure 7. As can be observed, the stability margin is high as gain margin = ∞ and phase margin = 65° and the bandwidth is designed to be fast. Moreover, the step response of the closed-loop current control is shown in Figure 8 and as can be seen, the percentage overshoot is less than 20% which is reasonable.

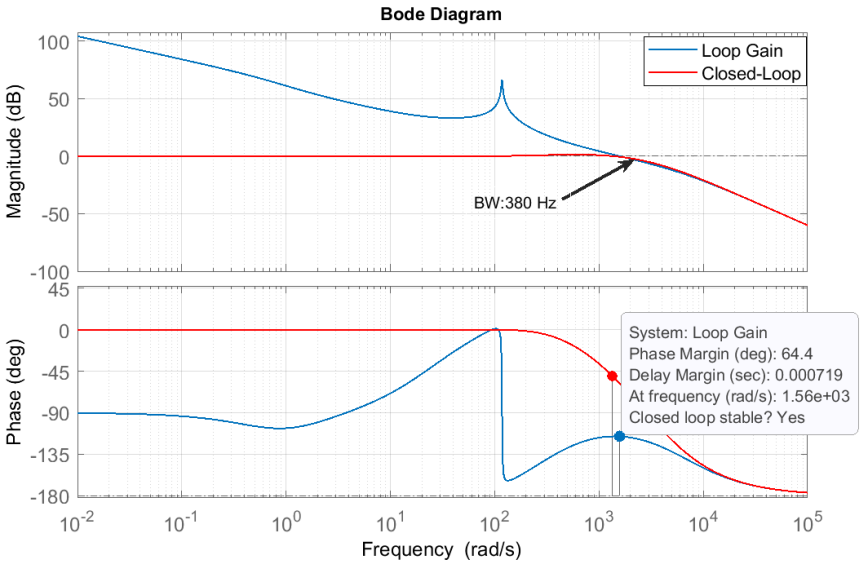

***Figure 7**. Closed-loop current control and Loop gain for q-component*

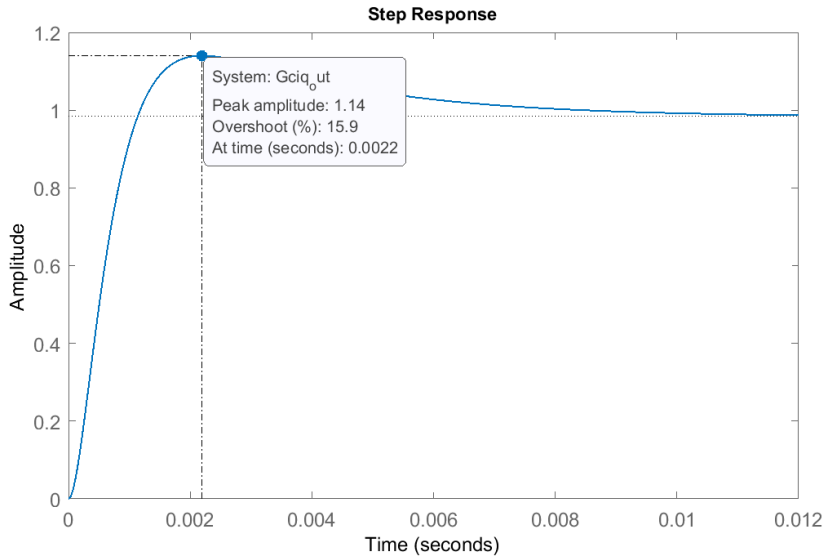

***Figure 8**. Closed-loop current control step response*

Considering the current control loops, the control variables of the PMSG-connected converter are not the duty ratios anymore and can be replaced by the current control references as

$$\hat{d}_{\mathrm{d}} = G_{\mathrm{cc-d}}\left(\hat{\imath}_{\mathrm{ref-d}} - \hat{\imath}_{\mathrm{d}}\right) \Rightarrow \quad \hat{d}_{\mathrm{d}} = \frac{G_{\mathrm{cc-d}}}{1 + L_{\mathrm{in-d}}}\hat{\imath}_{\mathrm{ref-d}}, \tag{4.8}$$

$$\hat{d}_{\mathrm{q}} = G_{\mathrm{cc-q}}\left(\hat{\imath}_{\mathrm{ref-q}} - \hat{\imath}_{\mathrm{q}}\right) \Rightarrow \quad \hat{d}_{\mathrm{d}} = \frac{G_{\mathrm{cc-q}}}{1 + L_{\mathrm{in-d}}}\hat{\imath}_{\mathrm{ref-q}}. \tag{4.9}$$

Hence, by substituting the duty ratios that are calculated based on the current control references as shown in (4.8) and (4.9), into the open-loop dynamic model presented in (3.54), the matrix of the closed-loop transfer functions of the PMSG-connected converter under the current control can be derived as

$$\begin{bmatrix} \hat{\imath}_{\mathrm{ind}} \\ \hat{\imath}_{\mathrm{inq}} \\ \hat{u}_{\mathrm{o}} \end{bmatrix} = \begin{bmatrix} Y_{\mathrm{in-d-c}} & G_{\mathrm{cr-qd-c}} & T_{\mathrm{oi-d-c}} & G_{\mathrm{ci-d-c}} & G_{\mathrm{ci-qd-c}} \\ G_{\mathrm{cr-dq-c}} & Y_{\mathrm{in-q-c}} & T_{\mathrm{oi-q-c}} & G_{\mathrm{ci-dq-c}} & G_{\mathrm{ci-q-c}} \\ G_{\mathrm{io-d-c}} & G_{\mathrm{io-q-c}} & -Z_{\mathrm{o-c}} & G_{\mathrm{co-d-c}} & G_{\mathrm{co-q-c}} \end{bmatrix} \begin{bmatrix} \hat{e}_{\mathrm{d}} \\ \hat{e}_{\mathrm{q}} \\ \hat{\imath}_{\mathrm{o}} \\ \hat{\imath}_{\mathrm{ref-d}} \\ \hat{\imath}_{\mathrm{ref-q}} \end{bmatrix}, \tag{4.10}$$

where the closed-loop current control transfer functions are shown by the subscript extension 'c'. The transfer functions representing the dynamic model of the PMSG-connected converter under the closed-loop current control are presented in Appendix A. The closed-loop transfer function of the input admittance of the q-channel can be expressed as

$$Y_{\mathrm{in-q-c}} = \left[\frac{Y_{\mathrm{in-q}}}{1 + L_{\mathrm{in-q}}} - \frac{G_{\mathrm{ci-dq}} L_{\mathrm{in-d}}}{G_{\mathrm{ci-d}}(1 + L_{\mathrm{in-q}})} \cdot \frac{G_{\mathrm{cr-qd}}}{(1 + L_{\mathrm{in-d}})} \right] \frac{1}{1 - \frac{G_{\mathrm{ci-dq}} L_{\mathrm{in-d}}}{G_{\mathrm{ci-d}}(1 + L_{\mathrm{in-q}})} \cdot \frac{G_{\mathrm{ci-qd}} L_{\mathrm{in-q}}}{G_{\mathrm{ci-q}}(1 + L_{\mathrm{in-d}})}}, \tag{4.11}$$

where the effect of the cross-coupling between d-channel and q-channel is considered in the model. Figure 9. shows the effect of the cross-coupling transfer functions on the input admittance of the q-channel under the closed-loop current control. It reveals that the cross-coupling has mostly affected the phase angle of the input admittance in the low frequency.

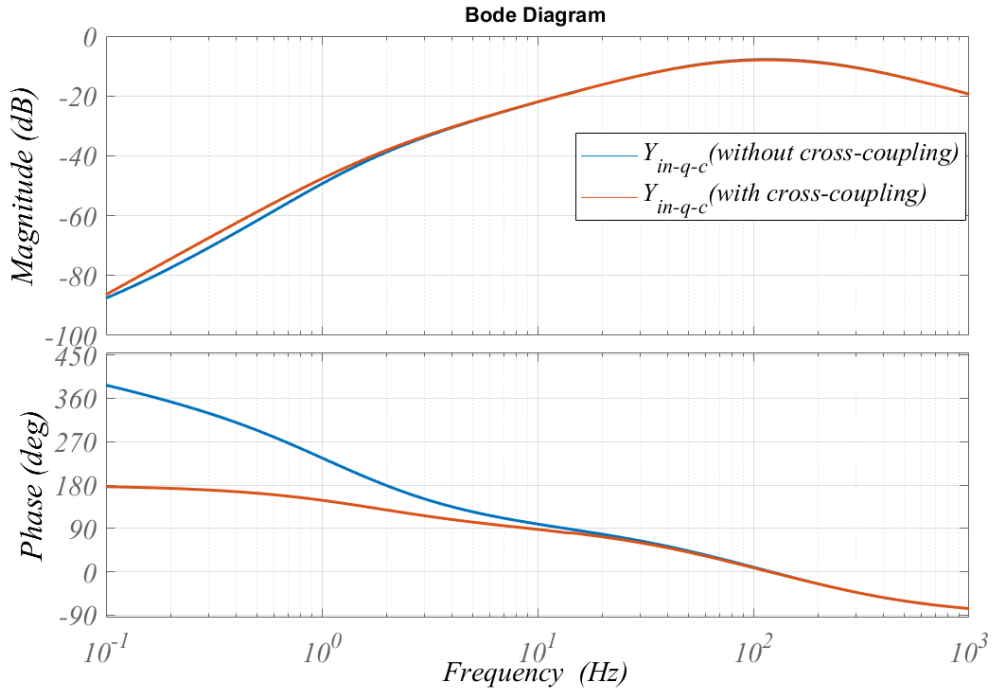

***Figure 9**. Input admittance of the q-channel under the closed-loop current control*

The transfer function between the q-channel current reference and the DC-link voltage can be presented as

$$G_{\mathrm{co-q-c}} = \frac{G_{\mathrm{co-q}}}{G_{\mathrm{ci-q}}} L_{\mathrm{in-q}} - \frac{G_{\mathrm{co-d}}}{G_{\mathrm{ci-d}}} L_{\mathrm{in-d}} G_{\mathrm{ci-qd-c}} - \frac{G_{\mathrm{co-q}}}{G_{\mathrm{ci-q}}} L_{\mathrm{in-q}} G_{\mathrm{ci-q-c}}\,, \tag{4.12}$$

in which besides the current loop gains, the closed-loop current control of the q-channel $G_{\mathrm{ci-q-c}}$ and the cross-coupling of $G_{\mathrm{ci-qd-c}}$ affect the dynamic behaviour of $G_{\mathrm{co-q-c}}$.

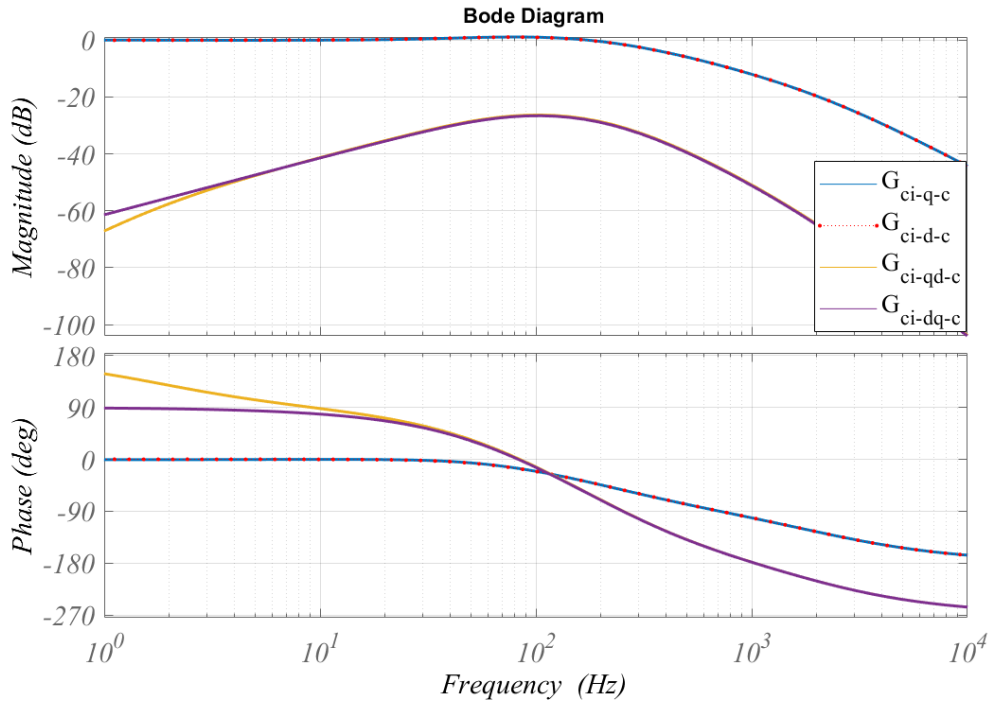

***Figure 10**. Frequency response of control-to-input currents transfer functions*

The dynamic behaviour of the control-to-input currents transfer functions are shown in Figure 10. It can be observed that the magnitudes of the cross-coupling transfer functions are much lower than the closed-loop current control transfer functions. Hence, the effect of cross-coupling on the q-channel control-to-output voltage transfer function can be ignored. The control-to-output voltage transfer function will be used in the next section for designing the DC-link voltage controller. Moreover, the input admittance of the q-channel will be used later for the stability assessment of the interconnected system when the PMSG-connected converter is under the closed-loop current control.

4.1.2 DC-link voltage control

The transfer function of the control variable to output voltage under the current control presented in (4.12) can be approximated as

$$G_{\mathrm{co-q-c}} \approx \frac{3}{2}\frac{-sLI_{\mathrm{q}} + E_{\mathrm{q}}}{C_{\mathrm{dc}}sU_{\mathrm{o}} + I_{\mathrm{o}}}\frac{L_{\mathrm{in-q}}}{1 + L_{\mathrm{in-q}}} \approx \frac{3}{2}\frac{LI_{\mathrm{q}}}{C_{\mathrm{dc}}U_{\mathrm{o}}}\frac{-s + \dfrac{E_{\mathrm{q}}}{LI_{\mathrm{q}}}}{s + \dfrac{I_{\mathrm{o}}}{C_{\mathrm{dc}}U_{\mathrm{o}}}}\frac{\alpha_{\mathrm{I}}}{s + \alpha_{\mathrm{I}}}$$

$$= K\frac{\omega_{\mathrm{z}} - s}{\omega_{\mathrm{p}} + s}\frac{\alpha_{\mathrm{I}}}{s + \alpha_{\mathrm{I}}}, \tag{4.13}$$

where the cross-coupling effects are neglected. In (4.13), ω_{z} represents the angular frequency of the RHP-zero $\frac{E_{\mathrm{q}}}{LI_{\mathrm{q}}}$. ω_{p} expresses the angular frequency of the LHP-pole $\frac{I_{\mathrm{o}}}{C_{\mathrm{dc}}U_{\mathrm{o}}}$.

K denotes $\frac{3}{2}\frac{LI_q}{C_{dc}U_o}$ and the bandwidth of the current control is shown by α_I. It can be observed from (4.13) that the transfer function has a non-minimal phase behaviour as one RHP-zero appears in the nominator. This zero is dependent on the operating point and can impose design limitations on the DC-link voltage controller. Therefore, in this work, the location of the RHP-zero is studied carefully and the operating point in which the worst-case scenario occurs is determined. Moreover, based on the Routh-Hurwitz criterion, the stability boundary for tuning the PI controller parameters are proposed.

The validity of the control-to-the DC-link voltage of the q-channel transfer function under the closed-loop current control should be verified before controller design process begins. Hence, the frequency response of G_{co-q-c} is measured using broadband excitation signals [28] where the perturbations are injected into the q-channel current reference and the output voltage is measured according to the block diagram depicted in Figure 11. It can be concluded from Figure 12 that the validity of the predicted model is verified by the frequency response of the simulation model in Matlab.

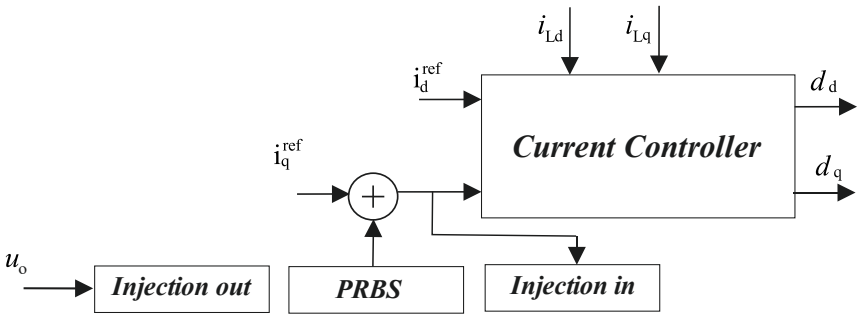

***Figure 11**. Block diagram of $\hat{\imath}_{ref-q}$ to $\hat{u}_o$ frequency response measurement*

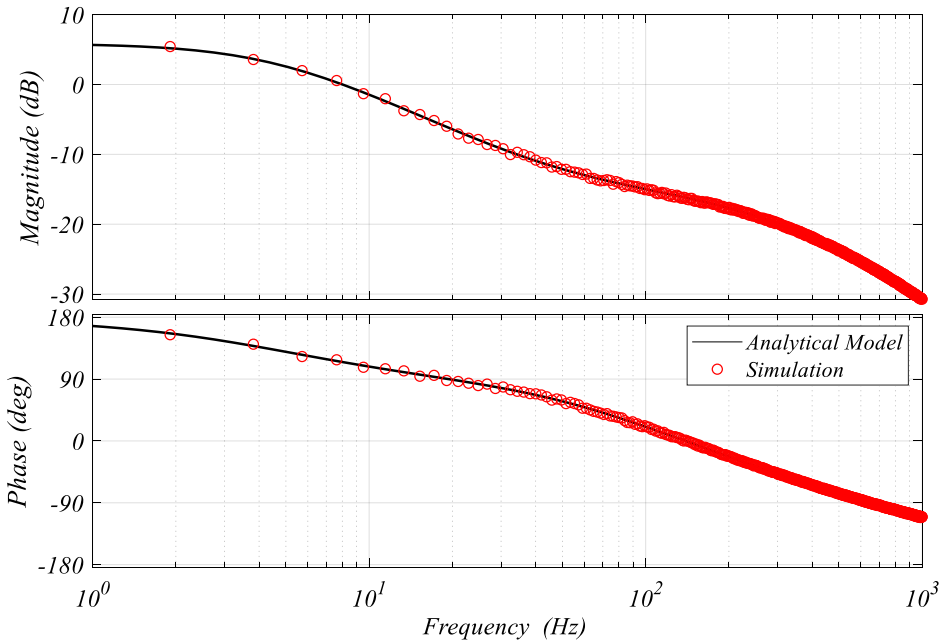

***Figure 12**. Control variable of q-channel to DC-link voltage*

Now that the validity of the plant transfer function for the output voltage control is verified, the controller design can be conducted using a standard proportional-plus-integral (PI) controller for the DC-link voltage control as

$$G_{\mathrm{cv}} = K_{\mathrm{pv}}\left(\frac{s + \omega_{\mathrm{zv}}}{s}\right), \tag{4.14}$$

where $\omega_{\mathrm{zv}} = \frac{K_{\mathrm{iv}}}{K_{\mathrm{pv}}}$. The loop gain of the DC-link voltage control L_{v} can be expressed as

$$L_{\mathrm{v}} = G_{\mathrm{co-q-c}}\, G_{\mathrm{cv}} = K\,\frac{\omega_{\mathrm{z}} - s}{\omega_{\mathrm{p}} + s}\,\frac{\alpha_{\mathrm{I}}}{s + \alpha_{\mathrm{I}}}\,K_{\mathrm{pv}}\left(\frac{s + \omega_{\mathrm{zv}}}{s}\right). \tag{4.15}$$

Given the loop gain defined in (4.15), the transfer function of the closed-loop output voltage control can be obtained as

$$\frac{\hat{u}_{\mathrm{o}}}{\hat{u}_{\mathrm{o-ref}}} = \frac{L_{\mathrm{v}}}{1 + L_{\mathrm{v}}}, \tag{4.16}$$

where $\hat{u}_{\mathrm{o-ref}}$ denotes the setpoint for the DC-link voltage controller. The denominator of the closed-loop transfer function can be expressed as

$$1 + L_{\mathrm{v}} = s^3 + \underbrace{\left(\omega_{\mathrm{p}} + \alpha_{\mathrm{I}} - KK_{\mathrm{pv}}\alpha_{\mathrm{I}}\right)}_{a_1}s^2 + \underbrace{\left(\omega_{\mathrm{p}}\alpha_{\mathrm{I}} + KK_{\mathrm{pv}}\alpha_{\mathrm{I}}(\omega_{\mathrm{z}} - \omega_{\mathrm{zv}})\right)}_{a_2}s + \underbrace{KK_{\mathrm{pv}}\alpha_{\mathrm{I}}\omega_{\mathrm{zv}}\omega_{\mathrm{z}}}_{a_3}, \tag{4.17}$$

where it can be used for degeminating the stability boundaries based on the Routh-Hurwitz criterion. Hence, a third order system is stable if all the coefficients of the polynomial are positive for all the operating points and the inequality given as

$$a_1 a_2 - a_3 > 0, \tag{4.18}$$

is satisfied. Since the closed-loop current control is designed to be much faster than the DC-link dynamics, the closed-loop current control can be approximated as $\frac{\alpha_{\mathrm{I}}}{s + \alpha_{\mathrm{I}}} \approx 1$. Hence, the denominator of the DC-link voltage closed-loop transfer function can be simplified as

$$1 + L_v = \left(C_{dc}U_o - {}^3/_2\, LI_qK_{pv}\right)s^2 + \left({}^3/_2\left(E_qK_{pv} - LI_qK_{iv}\right) + I_o\right)s + {}^3/_2\, E_qK_{iv}. \tag{4.19}$$

Therefore, to guarantee the stability of the closed-loop system under the DC-link voltage control, the inequalities presented as

$$\begin{gathered} K_{\mathrm{pv}} < \frac{2}{3}\frac{C_{\mathrm{dc}}U_{\mathrm{o}}}{LI_{\mathrm{q}}} \\ {}^3/_2\left(E_{\mathrm{q}}K_{\mathrm{pv}} - LI_{\mathrm{q}}K_{\mathrm{iv}}\right) + I_{\mathrm{o}} > 0 \end{gathered}, \tag{4.20}$$

must be satisfied at all operating points. The above constraints explain the critical values of the PI controller and no stability margin is considered which may result in poor transient performance. Therefore, for selection of the output voltage PI controller parameters, the following guidelines should be taken into account:

- According to [29], to ensure the stability of a loop gain in which there is a RHP-zero in the plant transfer function, the gain crossover frequency ω_{nc} must be smaller than $\omega_{\mathrm{z}}/2$ where

$$\omega_{\mathrm{z}} \simeq \frac{E_{\mathrm{q}}/I_{\mathrm{q}}}{L}. \tag{4.21}$$

As can be seen from (4.21), the frequency of the RHP-zero exits in the control-to-output voltage is the operating point dependant. Hence, in this thesis, the effect of the wind energy on the location of the zero is studied so that the worst-case scenario in which ω_{z} has the smallest value can be considered in the controller design. Taking the machine inductance as constant parameter, the location of ω_{z} only depends on the back-EMF voltage of the PMSG and the stator current of the q-channel. Therefore, according to the $T_m - \omega_t$ curve, it can be predicted that the lowest frequency of the RHP-zero occurs that the maximum torque point for a certain wind speed. Furthermore, the wind velocity variations change the location of ω_{z}. The relationships between the wind speed and the input current and the back-EMF voltage can be extracted from the wind turbine equations as

$$\begin{aligned} E_{\mathrm{q}} &\propto v_{\mathrm{w}} \\ I_{\mathrm{q}} &\propto {v_{\mathrm{w}}}^2, \end{aligned} \tag{4.22}$$

where it can be found that the location of the RHP-zero inversely proportional to the wind velocity. Clearly, it can be found from Figure 13 that the higher is the wind velocity the lower is the frequency of the RHP zero. Therefore, the lowest frequency of ω_{z} can be obtained at the maximum torque operating point where the wind velocity operates at the highest operating speed.

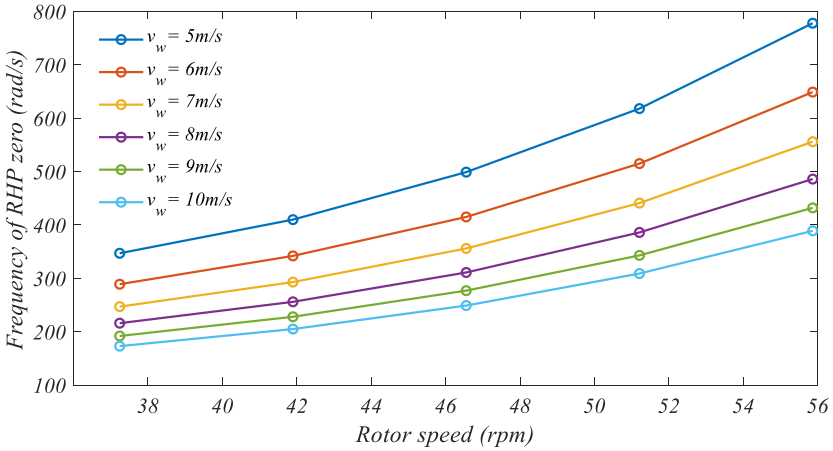

***Figure 13**. Variation of the frequency of RHP-zero as a function of rotor speed for different wind velocity*

- Based on the controller designing constraint given in (4.20), the maximum limitation on choosing K_{pv} is dependent on the electromagnetic torque of the PMSG. Hence, to meet the constraint for all operating points, K_{pv} must be smaller than

the smallest value of $\frac{2}{3}\frac{C_{dc}U_o}{LI_q}$ which can be calculated based on the maximum operating torque of the machine which occurs at the highest wind speed.

- For tuning K_{iv} of the PI controller, the following inequality must be satisfied for achieving a loop gain with good stability margin

$$K_{iv} < \frac{\left({}^{\omega_z}/_2\right)^2\left(C_{dc}U_o - {}^{3}/_2\, LI_q K_{pv}\right)}{1.5\, E_q} \tag{4.23}$$

Consequently, applying the above guidelines in designing the DC-link voltage controller, the frequency response of the DC-link voltage loop gain predicted by the analytical model has to be verified. The same method as for the plant transfer function is used here and the frequency response measurement setup for the loop gain is illustrated in Figure 14. As can be seen, in this case, the excitation signal is injected into the output of the DC-link voltage controller and the measurements are taken from both sides of the injection point. The measured frequency response of the loop gain obtained from the simulation demonstrates the validity of the analytical model as shown in Figure 15.

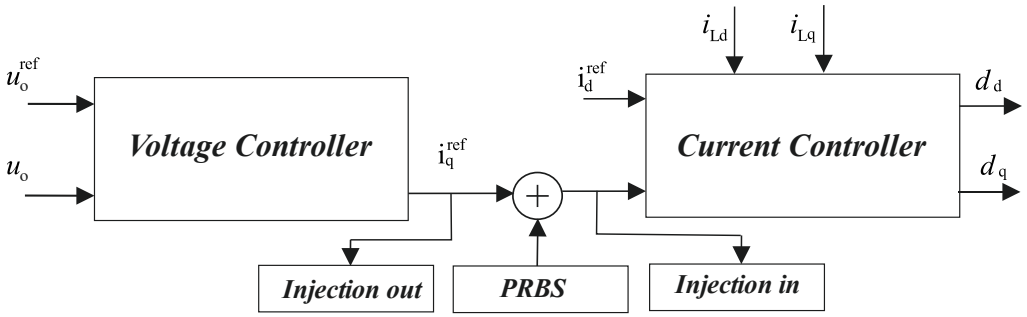

***Figure 14**. Block diagram for loop gain frequency response measurement*

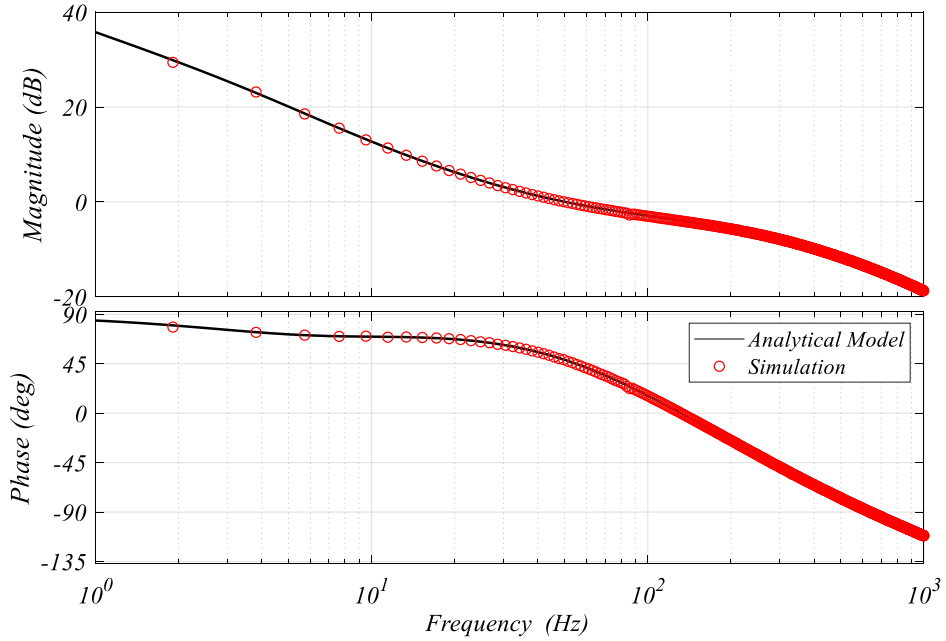

***Figure 15**. DC-link voltage control loop gain*

Now the DC-link voltage loop gain can be included into the closed-loop current control transfer functions of the PMSG-connected converter presented in (4.10). In that way, the control variable for the q-channel can be given as

$$\hat{\imath}_{\mathrm{ref-q}} = G_{\mathrm{cv}}\,(\hat{u}_{\mathrm{o-ref}} - \hat{u}_{\mathrm{o}}) \;\Rightarrow\quad \hat{\imath}_{\mathrm{ref-q}} = \frac{G_{\mathrm{cv}}}{1 + L_{\mathrm{v}}}\hat{u}_{\mathrm{o-ref}}, \tag{4.24}$$

where the q-channel current reference is replaced by $\hat{u}_{\mathrm{o-ref}}$.

By substituting (4.24) into the matrix of closed-loop current control transfer functions presented in (4.10), the transfer functions describing the dynamic behaviour of the PMSG-connected converter under the closed-loop of both current and DC-link voltage can be expressed as

$$\begin{bmatrix}\hat{\imath}_{\mathrm{ind}}\\ \hat{\imath}_{\mathrm{inq}}\\ \hat{u}_{\mathrm{o}}\end{bmatrix} = \begin{bmatrix} Y_{\mathrm{in-d-cv}} & G_{\mathrm{cr-qd-cv}} & T_{\mathrm{oi-d-cv}} & G_{\mathrm{ci-d-cv}} & G_{\mathrm{ci-qd-cv}}\\ G_{\mathrm{cr-dq-cv}} & Y_{\mathrm{in-q-cv}} & T_{\mathrm{oi-q-cv}} & G_{\mathrm{ci-dq-cv}} & G_{\mathrm{ci-q-cv}}\\ G_{\mathrm{io-d-cv}} & G_{\mathrm{io-q-cv}} & -Z_{\mathrm{o-cv}} & G_{\mathrm{co-d-cv}} & G_{\mathrm{co-q-cv}}\end{bmatrix}\begin{bmatrix}\hat{e}_{\mathrm{d}}\\ \hat{e}_{\mathrm{q}}\\ \hat{\imath}_{\mathrm{o}}\\ \hat{\imath}_{\mathrm{ref-d}}\\ \hat{u}_{\mathrm{o-ref}}\end{bmatrix}, \tag{4.25}$$

where the subscript extension 'cv' represents the transfer functions of the PMSG-connected converter dynamic model when both the current control and the DC-link voltage control loops are closed.

The transfer functions of the matrix (4.25) are expressed in Appendix B. However, here the transfer function of the q-channel input admittance, which will be used for the stability studies, is discussed. The q-channel input admittance under the cascaded control scheme can be presented as

$$Y_{\mathrm{in-q-cv}} = \frac{Y_{\mathrm{in-q-c}}}{1 + L_{\mathrm{v}}} + \frac{L_{\mathrm{v}}}{1 + L_{\mathrm{v}}}\,Y_{\mathrm{in-q-inf}}, \tag{4.26}$$

where $Y_{\mathrm{in-q-inf}}$ represents the ideal (infinite bandwidth) input admittance and can be defined as

$$Y_{\mathrm{in-q-inf}} = Y_{\mathrm{in-q}} - \frac{G_{\mathrm{io-d}}G_{\mathrm{ci-q}}}{G_{\mathrm{co-q}}}. \tag{4.27}$$

As can be observed from Figure 16, the dynamic behaviour of the ideal input admittance for the low frequency is like a negative conductance. Furthermore, Figure 17 shows the frequency response of the first term in (4.26) in comparison with the q-channel input admittance under the closed-loop current control. It can be realized that the magnitude of $Y_{\mathrm{in-q-c}}$ which is small within the low frequency range becomes smaller when the DC-link voltage loop control is applied. The reason is that the loop gain is much larger than 1 ($L_{\mathrm{v}} \gg 1$) at the frequencies below the crossover frequency of the DC-link voltage controller. Therefore, the closed-loop dynamic of the q-channel input admittance of the PMSG-connected converter under the DC-link voltage control can be approximated by the second term in (4.26).

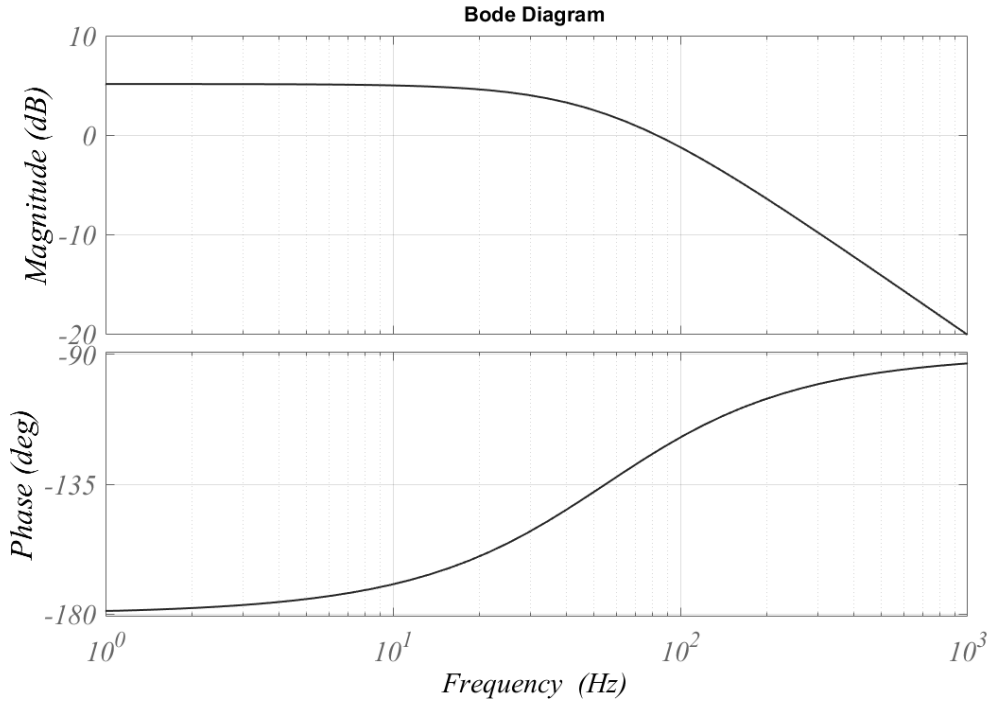

***Figure 16**. Frequency response of Ideal input admittance for the q-channel*

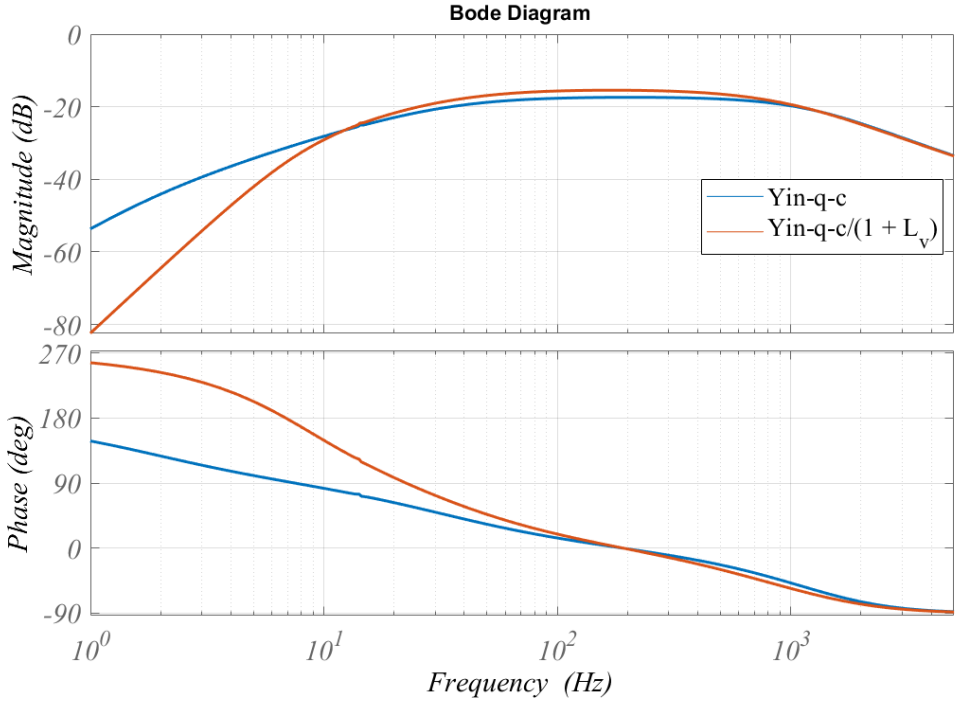

***Figure 17**. Closed-loop current control Input admittance versus* $\frac{Y_{in-q-c}}{1+L_v}$

The validity of the analytical model is verified as shown in Figure 18 where the frequency response of the q-channel input impedance $\left(Z_{\text{in}-\text{q}-\text{c}} = 1/Y_{\text{in}-\text{q}-\text{c}}\right)$ is measured as this term will be used in the stability studies. As can be seen, within the low frequencies the input impedance of PMSG-connected converter in the q-channel has a negative resistor impedance like behaviour when both the current and voltage loop controls are closed. This negative resistance behaviour can lead to instability when the wind turbine is connected

to the PMSG. The effect of this dynamic behaviour on the stability analysis will be discussed later.

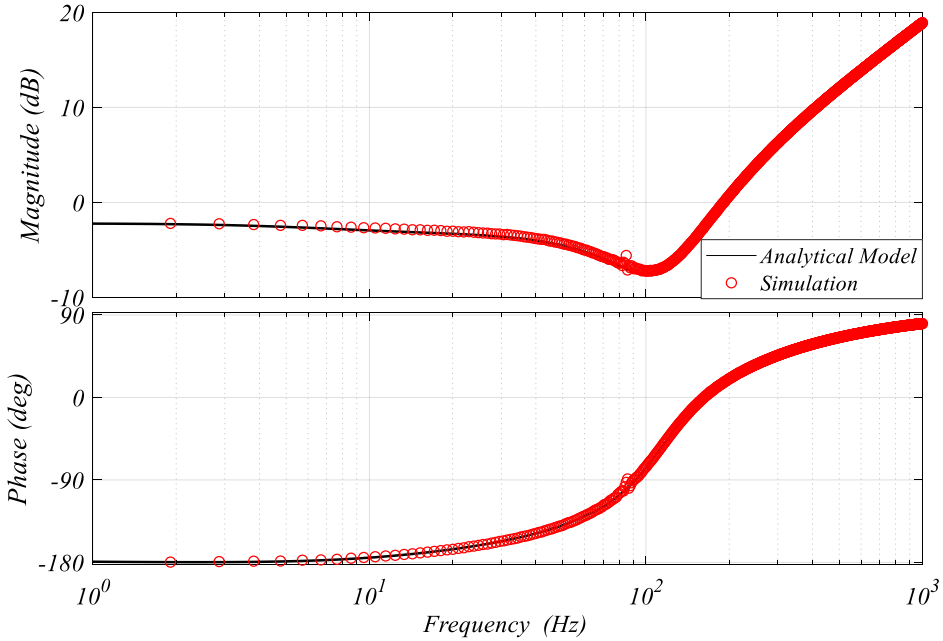

***Figure 18**. Input impedance of the PMSG-connected converter for the q-channel under the output voltage closed-loop control.*

4.2 Grid-side inverter control

The control scheme for the grid-connected converter is illustrated in Figure 19 where the DC-side of the inverter is connected to a voltage source. Because it is assumed that the machine-side converter regulates the DC-link voltage. The grid-connected inverters are typically controlled in the grid voltage-oriented reference frame where the d-channel is aligned with the grid-connected inverter output voltage. Hence, the active power can be independently controlled through the d-channel current of the inverter and the q-channel can be used to control the reactive power. The reference value for the reactive power can be taken to be zero when there is no need for reactive power injection. However, under grid voltage disturbances, the setpoint of the reactive power controller can be determined by a grid voltage controller as an outer control loop. As for the active power, its setpoint can be determined either by a supervisory control operator or a MPPT controller. The main function of the grid-connected inverter, under the alternative control strategy, is to extract the maximum power of the wind turbine thus the active power reference value is typically assigned by the MPPT mode. However, because of the new grid codes requirements, the power supply needs to be controlled so that the active power reference can be set to a constant value which is known as controlled-power mode.

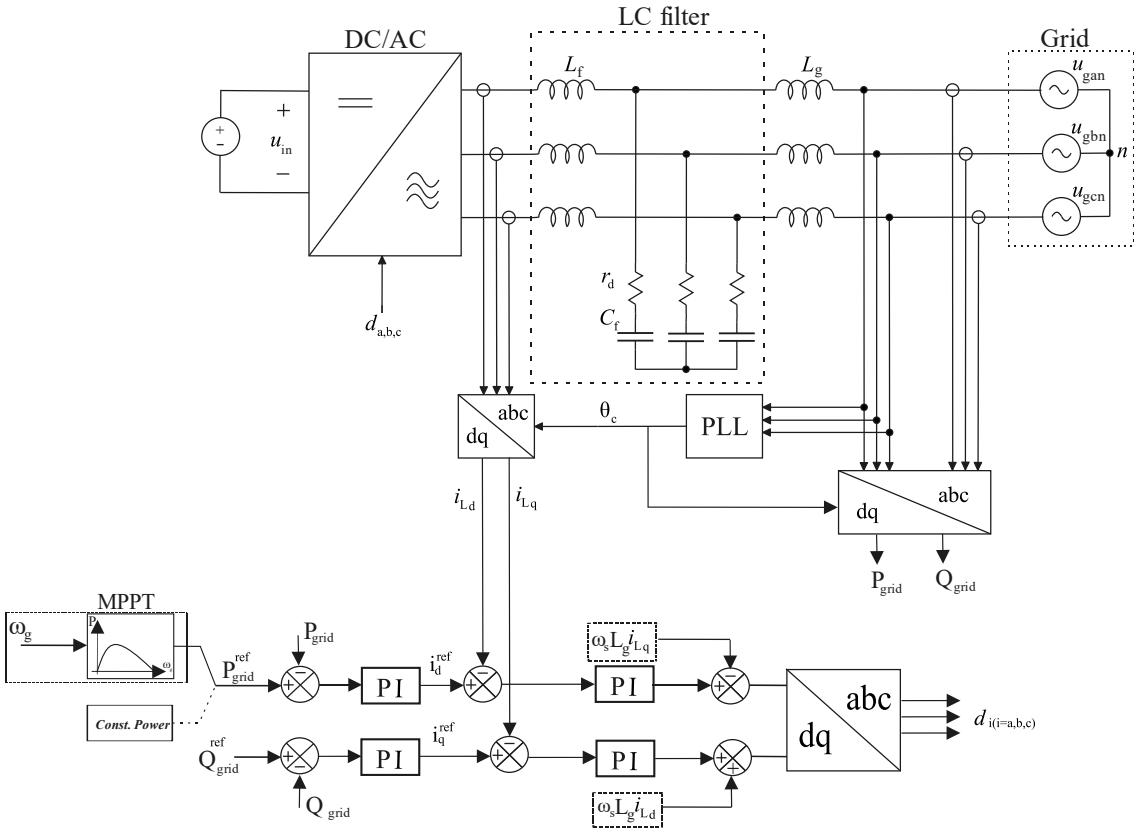

***Figure 19**. Control scheme for grid-side inverter*

Both the active power and the reactive power are controlled through a cascaded control scheme where the output of the power loops set the reference values of the current controllers. The current control loop for both the dq-channels can be designed based on the same method that used in the previous section for the PMSG-connected converter. The PI controller parameters of the current controllers should be tuned so that the band-width of the current control loop is high enough as it results in a high-output impedance which is desired for the grid-connected inverters.

Since the focus of this thesis is on the machine-side converter control strategy, the grid-side inverter is not studied in detail. It is assumed that the inverter dynamics can be simplified and modelled by a sink current from the PMSG-connected converter point of view as the closed-loop bandwidth of the grid-side inverter is designed to be fast enough. The active power setpoint when the grid-connected inverter operates under the MPPT mode can be employed by an optimal reference power curve [30]. Based on this method, a pre-defined power-speed curve can be obtained where the optimum active power ref-erence for a certain wind speed can be assigned. In practice, this curve can be extracted by experimental tests or through simulations and can be used as a look-up table. In this thesis, the active power setpoint is determined by

$$P_{\mathrm{MPPT}} = K_{\mathrm{opt}}\omega_{\mathrm{g}}^{3}, \tag{4.28}$$

where K_{opt} which is a constant parameter depending on the wind turbine construction and characteristic can be obtained as

$$K_{\mathrm{opt}} = \frac{0.5Rr^5\rho}{\lambda_{\mathrm{opt}}^3} C_{\mathrm{p}}\left(\lambda_{\mathrm{opt}}, \beta_{\mathrm{min}}\right). \tag{4.29}$$

The optimal tip-speed ratio shown by λ_{opt} can be achieved where the power coefficient is at its peak value and the pitch angle at its minimum. By assuming a fast power control, the output power transferred to the grid can be taken equal to the P_{MPPT} if the converter is considered as a lossless component. Therefore, the active power setpoint can be determined as follows:

$$P_{\mathrm{grid}}^{\mathrm{ref}} = \begin{cases} P_{\mathrm{MPPT}} & \omega_{\mathrm{g}} < \omega_{\mathrm{g-max}} \\ P_{\mathrm{max}} & \omega_{\mathrm{g}} \geq \omega_{\mathrm{g-max}} \end{cases}, \tag{4.30}$$

where $P_{\mathrm{grid}}^{\mathrm{ref}}$ represents the active power reference. The maximum power that can be extracted from the wind turbine is shown by P_{max} and the maximum angular rotor speed of the generator is expressed by $\omega_{\mathrm{g-max}}$.

5. WTG-COUPLED CONVERTER DYNAMIC MODEL

In this chapter, the dynamic model of the two-mass drive-train of the wind turbine is derived where the dynamic behaviour of the model for different operating point is discussed. Then, the interconnected stability of the WT and the interfacing PMSG-connected converter is evaluated. Moreover, the effect of the wind turbine dynamic is included into the PMSG-connected converter model so that the WTG-coupled converter model is utilized to study the stability analysis and control loop design.

5.1 Dynamic properties of the wind turbine drive-train

The dynamic model of turbine drive-train considering the aerodynamic torque can be given as

$$J_{\mathrm{t}}\frac{d\widehat{\omega}_{\mathrm{t}}}{dt} = \hat{T}_{\mathrm{t}} - K_{\mathrm{s}}\hat{\theta}_{\mathrm{s}} - B_{\mathrm{s}}\widehat{\omega}_{\mathrm{t}} + B_{\mathrm{s}}\widehat{\omega}_{\mathrm{g}}, \tag{5.1}$$

$$J_{\mathrm{g}}\frac{d\widehat{\omega}_{\mathrm{g}}}{dt} = K_{\mathrm{s}}\hat{\theta}_{\mathrm{s}} - \hat{T}_{\mathrm{g}} + B_{\mathrm{s}}\widehat{\omega}_{\mathrm{t}} - B_{\mathrm{s}}\widehat{\omega}_{\mathrm{g}}, \tag{5.2}$$

$$\frac{d\hat{\theta}_{\mathrm{s}}}{dt} = \widehat{\omega}_{\mathrm{t}} - \widehat{\omega}_{\mathrm{g}}, \tag{5.3}$$

$$A = \begin{bmatrix} \frac{\gamma - B_{\mathrm{s}}}{J_{\mathrm{t}}} & \frac{B_{\mathrm{s}}}{J_{\mathrm{t}}} & -\frac{K_{\mathrm{s}}}{J_{\mathrm{t}}} \\ \frac{B_{\mathrm{s}}}{J_{\mathrm{g}}} & -\frac{B_{\mathrm{s}}}{J_{\mathrm{g}}} & \frac{K_{\mathrm{s}}}{J_{\mathrm{g}}} \\ 1 & -1 & 0 \end{bmatrix}, B = \begin{bmatrix} 0 & 0 \\ 0 & -\frac{1}{J_{\mathrm{g}}} \\ 0 & 0 \end{bmatrix}, C = \begin{bmatrix} 1 & 0 & 0 \\ 0 & 1 & 0 \end{bmatrix}, D = \begin{bmatrix} 0 & 0 \\ 0 & 0 \end{bmatrix}, \tag{5.4}$$

where $\gamma = \partial T_{\mathrm{t}}/\partial \omega_{\mathrm{t}}$. From $T_{\mathrm{t}} - \omega_{\mathrm{t}}$ curve, it can be found that γ has a negative sign while moving within the right-hand side of the curve. This shows the negative resistance-like behaviour in which the rotor speed increases with the torque decreasing. However, the sign of γ is positive when moving within the left-hand side of the curve thus the sign of γ is dependent on the operating point of the wind turbine for a certain wind velocity.
From the state-space model of the wind turbine drive-train, the transfer function between the rotational speed of generator and the electromechanical torque can be derived as

$$\frac{\widehat{\omega}_{\mathrm{g}}}{\hat{T}_{\mathrm{g}}} = -\frac{1}{J_{\mathrm{g}}}\frac{s^2 + \frac{B_{\mathrm{s}} - \gamma}{J_{\mathrm{t}}}s + \frac{K_{\mathrm{s}}}{J_{\mathrm{t}}}}{s^3 + \left(\frac{B_{\mathrm{s}}(J_{\mathrm{t}} + J_{\mathrm{g}})}{J_{\mathrm{t}}J_{\mathrm{g}}} - \frac{\gamma}{J_{\mathrm{t}}}\right)s^2 + \left(\frac{K_{\mathrm{s}}(J_{\mathrm{t}} + J_{\mathrm{g}})}{J_{\mathrm{t}}J_{\mathrm{g}}} + \frac{B_{\mathrm{s}}\gamma(J_{\mathrm{t}} + J_{\mathrm{g}})}{J_{\mathrm{t}}^2 J_{\mathrm{g}}}\right)s - \frac{K_{\mathrm{s}}\gamma}{J_{\mathrm{t}}J_{\mathrm{g}}}}. \tag{5.7}$$

The transfer function in (5.7) contains a pair of complex zeros which can be approximated as

$$\omega_{z1,2} \approx \frac{(B_s - \gamma)}{2J_t} \pm j\sqrt{\frac{K_s}{J_t}}, \tag{5.8}$$

and the roots of its denominator with reasonable values can be estimated as

$$\omega_{p1} \approx \frac{\gamma}{J_t + J_g}, \tag{5.9}$$

$$\omega_{p2,3} \approx \left(-\frac{B_s(J_t + J_g)}{J_t J_g} + \left(\frac{\gamma}{J_t} - \frac{\gamma}{J_t + J_g}\right) \pm j\sqrt{\frac{4K_s(J_t + J_g)}{J_t J_g} + \frac{B_s\gamma(J_t + J_g)}{J_t^2 J_g}}\right)\Big/2$$

$$\approx \left(-\frac{B_s(J_t + J_g)}{J_t J_g} \pm j\sqrt{\frac{4K_s(J_t + J_g)}{J_t J_g}}\right)\Big/2. \tag{5.10}$$

As can be found from (5.9) - (5.10), there is a real pole representing the dynamic of the aerodynamic torque of the wind turbine which is located in the very low due to the large overall inertia of the drive-train. Furthermore, the oscillatory modes of the drive-train system appear in the dynamic model as a pair of complex poles where the effect of the aerodynamic torque dynamic can be neglected due to the large turbine inertia. Clearly, the low frequency real-pole can become a RHP-pole when the operating point moves into the left-hand side of $T_t - \omega_t$ curve where with increasing the aerodynamic torque the rotational speed increases. Therefore, one can conclude that the wind turbine drive-train subsystem can be unstable for γ with the positive slope.

Furthermore, it can be realized that the torsional resonance frequency ω_{n-res} can be defined as

$$\omega_{n-res} \approx \sqrt{\frac{K_s(J_t + J_g)}{J_t J_g}}. \tag{5.11}$$

Since the real part of the complex poles are directly proportional to B_s, the damping ratio of the torsional resonance ζ_{res} is also directly dependent on the value of the damping coefficient of the drive-train where it can be given as

$$\zeta_{res} = \frac{B_s(J_t + J_g)}{J_t J_g}\Big/\left(2\sqrt{\frac{K_s(J_t + J_g)}{J_t J_g}}\right). \tag{5.12}$$

From the numerator of the transfer function in (5.7), the so-called anti-resonance frequency $\omega_{anti-res}$ can be extracted as

$$\omega_{anti-res} \approx \sqrt{\frac{K_s}{J_t}}, \tag{5.13}$$

where it can be realized that $\omega_{anti-res}$ is dependent on the shaft stiffness and the turbine inertia thus it always occurs at the lower frequencies than ω_{n-res}.

From (5.12), it can be found that the real part of the pair of complex zeros are dependent on both operating point and the damping coefficient. Hence, the damping ratio of the anti-resonance frequency can be given by

$$\zeta_{\text{anti-resonance}} = \frac{(B_s - \gamma)}{J_t} \Big/ \left(4\sqrt{\frac{K_s}{J_t}}\right). \tag{5.14}$$

According to [31], the mechanical component of the WT drive-train can be modelled as the electrical equipment through dividing the mechanical parameters by the square of the machine torque constant K_T which can be obtained as

$$K_T^2 = \left(1.5 n_p \lambda_m\right)^2. \tag{5.15}$$

Hence, the transfer function of (5.7) can be presented by

$$Z_{oS} = \frac{C_t s^2 + s/r_{dyn} + L_t}{C_t C_g s^3 + C_g/r_{dyn} s^2 + L_t(C_t + C_g)s + L_t/r_{dyn}}, \tag{5.16}$$

where C_t and C_g represent the turbine and generator inertias, respectively. L_t denotes the shaft stiffness and r_{dyn} indicates the inverse of γ. The damping coefficient is ignored in (5.16). As can be seen, all the mechanical components are described by the equivalent electrical equipment so that the interconnected stability can be evaluated using the impedance-based method. Therefore, for the rest of the thesis, Z_{oS} will be considered as the output impedance of the WT.

The output impedance of the wind turbine is illustrated in Figure 20 for different operating points in the region that γ has a negative slope where the wind speed considered as a constant. The γ is roughly the only parameter affected by operating point variations so that its minimum value occurs where the maximum aerodynamic torque at a certain wind speed and γ increases with decrease at torque and increase at the rotor speed.

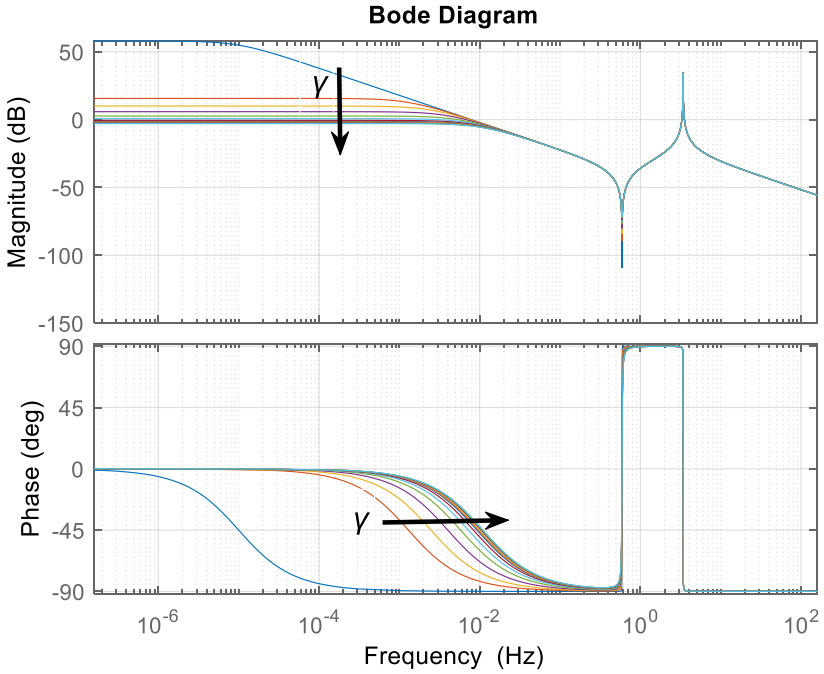

***Figure 20**. Output impedance of wind turbine*

5.2 Interconnected system stability assessment

Considering Z_{oS} as the output impedance of the wind turbine and $\mathrm{Y}_{\mathrm{in-q}}$ representing the input impedance of the PMSG-connected converter, the stability of the interconnected system can be assured if the impedance ratio $Z_{\mathrm{oS}}\mathrm{Y}_{\mathrm{in-q}}$ does not contain any RHP-zeros. However, this approach is only valid when the wind turbine small-signal model and the dynamic model of PMSG-connected converter are both stable on their own [32]. As discussed before, the wind turbine dynamic model can be unstable only if the operating point moves to the right-hand side of the torque-rotor speed curve. Therefore, considering that the machine operates in the region where γ has negative slope, it can be concluded that the wind turbine model is stable for all the operating points. As for the stability of the interfacing converter, it can be realized that the PMSG-connected converter subsystem is always stable as no RHP-zeros can be found in the denominator of the PMSG-connected converter transfer functions presented in (3.66). Thus, for any operating point at the below rated wind speed, the input admittance $Y_{\mathrm{in-q}}$ can be used for the impedance ratio stability assessment method.

The input admittance of the PMSG-connected converter for q-component where the stator resistance is ignored can be given by

$$Y_{\mathrm{in-q}} = \frac{1}{L}\frac{s^2 - \frac{\omega_{\mathrm{e}}LI_{\mathrm{q}}}{\lambda_{\mathrm{m}}}s + \frac{3}{2LC_{\mathrm{dc}}}\left(D_{\mathrm{d}}^2 - \frac{D_{\mathrm{d}}D_{\mathrm{q}}LI_{\mathrm{q}}}{\lambda_{\mathrm{m}}}\right)}{s\left(s^2 + \omega_{\mathrm{e}}^2 + \frac{3}{2}\frac{D_{\mathrm{d}}^2 + D_{\mathrm{q}}^2}{LC_{\mathrm{dc}}}\right)}. \tag{5.17}$$

As $D_{\mathrm{d}}^2 - \frac{D_{\mathrm{d}}D_{\mathrm{q}}LI_{\mathrm{q}}}{\lambda_{\mathrm{m}}} \approx 0$ where the stator resistance and the converter losses are neglected, $Y_{\mathrm{in-q}}$ can be simplified as

$$Y_{\mathrm{in-q}} = \frac{1}{L}\frac{s - \frac{\omega_{\mathrm{e}}LI_{\mathrm{q}}}{\lambda_{\mathrm{m}}}}{s^2 + \omega_{\mathrm{e}}^2 + \frac{3}{2}\frac{D_{\mathrm{d}}^2 + D_{\mathrm{q}}^2}{LC_{\mathrm{dc}}}}. \tag{5.18}$$

The low frequency behaviour of the input admittance can be approximated by setting $s \approx 0$ in (5.18) yielding

$$Y_{\mathrm{in-q}} \approx \frac{-\frac{\omega_{\mathrm{e}}LI_{\mathrm{q}}}{\lambda_{\mathrm{m}}}}{\omega_{\mathrm{e}}^2 + \frac{3}{2}\frac{D_{\mathrm{d}}^2 + D_{\mathrm{q}}^2}{LC_{\mathrm{dc}}}}. \tag{5.19}$$

The input impedance of the q-channel $Z_{\mathrm{in-q}} = 1/Y_{\mathrm{in-q}}$ is shown in Figure 21. As can be observed, the phase angle starts from -180° which means that the input impedance of the PMSG-connected converter behaves like a negative resistance for the low frequency.

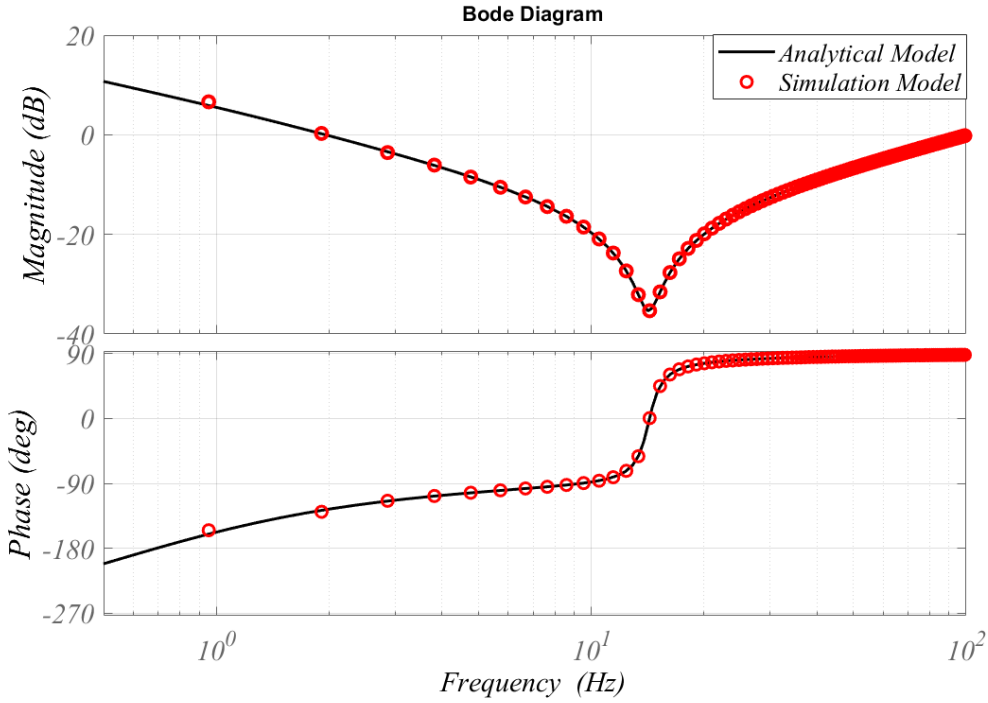

***Figure 21**. Input impedance of PMSG-connected converter for q-channel*

The parasitic parameters including the stator resistance were ignored so far to simplify the calculations. However, in practice, considering a PMSG with zero stator resistance is unrealistic thus by adding the machine stator resistance in the model, the input admittance of the q-component can be reformulated and given by

$$Y_{\mathrm{in-q}} = \frac{1}{L}\frac{s^2 + \left(\frac{R_\mathrm{s}}{L} - \frac{\omega_\mathrm{e} L I_\mathrm{q}}{\lambda_\mathrm{m}}\right)s + \frac{3}{2LC}\left(D_\mathrm{d}^2 - \frac{D_\mathrm{d} D_\mathrm{q} L I_\mathrm{q}}{\lambda_\mathrm{m}}\right)}{s^3 + 2\frac{R_\mathrm{s}}{L}s^2 + \left(\left(\frac{R_\mathrm{s}}{L}\right)^2 + \omega_\mathrm{e}^2 + \frac{3}{2}\frac{D_\mathrm{d}^2 + D_\mathrm{q}^2}{LC_\mathrm{dc}}\right)s + \frac{3}{2}\frac{D_\mathrm{d}^2 + D_\mathrm{q}^2}{LC_\mathrm{dc}}R_\mathrm{s}}. \quad (5.20)$$

The roots of the numerator of (5.20) can be obtained as

$$s_{1,2} = \frac{-\left(\frac{R_\mathrm{s}}{L} - \frac{\omega_\mathrm{e} L I_\mathrm{q}}{\lambda_\mathrm{m}}\right) \pm \sqrt{\left(\frac{R_\mathrm{s}}{L} - \frac{\omega_\mathrm{e} L I_\mathrm{q}}{\lambda_\mathrm{m}}\right)^2 - \frac{6}{LC_\mathrm{dc}}\left(D_\mathrm{d}^2 - \frac{D_\mathrm{d} D_\mathrm{q} L I_\mathrm{q}}{\lambda_\mathrm{m}}\right)}}{2}. \quad (5.21)$$

From (5.21), it can be found that there exist two zeros in the input admittance of q-channel of the PMSG-connected converter where depending on the value of the stator resistance and the operating point, the real part of the zeros can be located in RHP or LHP of the complex plane and they can be real or complex.

$$R_\mathrm{s} > \omega_\mathrm{e} L^2 I_\mathrm{q} / \lambda_\mathrm{m} \quad (5.22)$$

Hence, it can be realized from (5.21) that if the value of the stator resistance is high enough so that the inequality of (5.22) holds true, the zeros will be located in LHP and the electrical damping will be positive. To guarantee the positive damping behaviour for the all operating points, the stator resistance needs to be larger than the maximum value of $\omega_\mathrm{e} L^2 I_\mathrm{q} / \lambda_\mathrm{m}$ which can be obtained at the maximum power point of the $P_\mathrm{m} - \omega_\mathrm{t}$ curve for

the highest operating wind speed in the WECS if the machine parameters are considered as constant. The input impedances of the PMSG at the maximum power point for the different wind velocities are shown in Figure 22 where the inequality of (5.22) meet for the MPP at the highest working wind velocity. As it can be observed, the electrical damping is positive for the input impedances as the phase angle started from 0 degree in all cases.

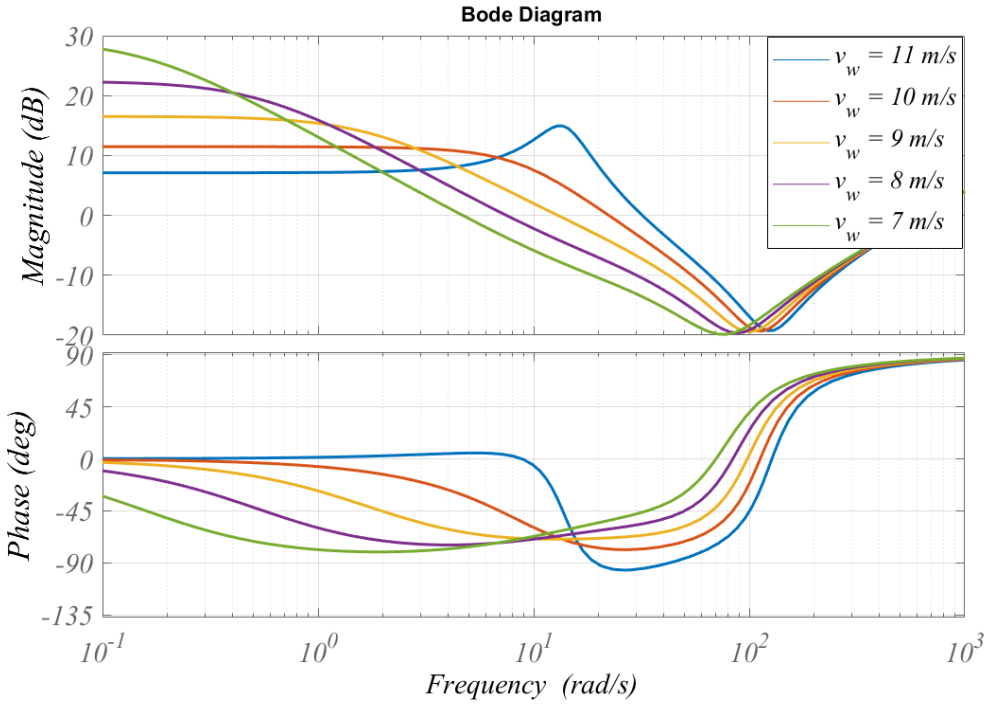

***Figure 22**. Input impedance of PMSG-connected converter for different wind speeds at MPP*

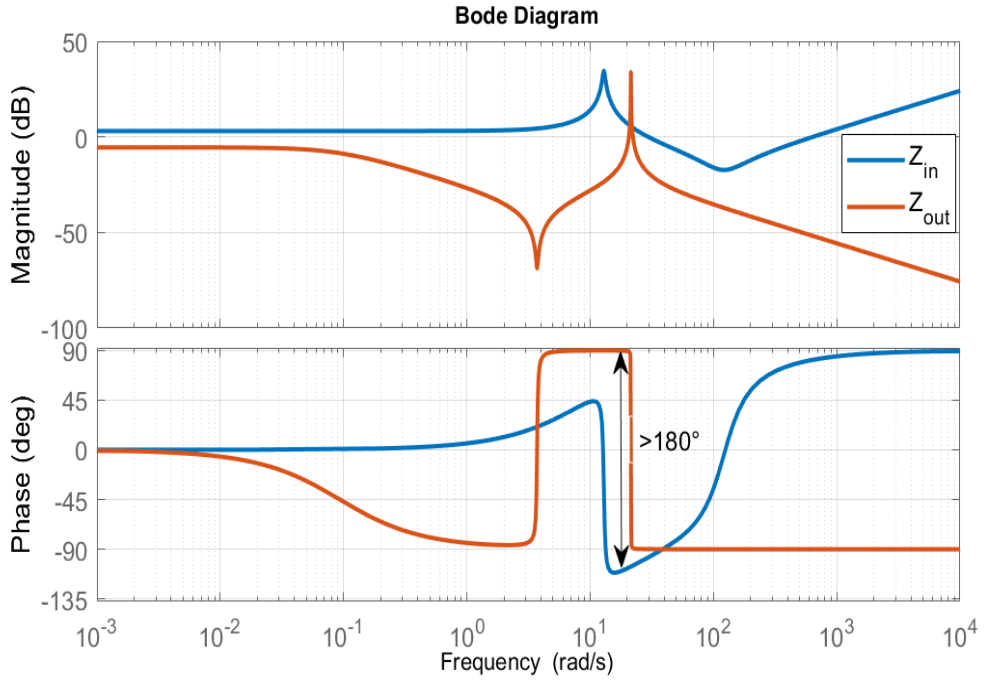

***Figure 23**. Input impedance of the converter and output impedance of the source*

Figure 23 shows the output impedance of the wind turbine drive-train against the input impedance of the PMSG-connected converter where the stator resistance is considered to be large enough so that the inequality of (5.22) is kept true. However, as can be seen, the interfacing converter with the source leads to instability as within the natural frequency of the wind turbine drive-train in which the magnitude of the output impedance is larger than the input impedance of the converter, the phase angle difference between $Z_{\mathrm{in-q}}$ and Z_{oS} (shown by Z_{out} in Figure 23) exceeds 180 degree.

In order to avoid the instability of the interconnected system, either the damping coefficient B_{s} must be very large so that the peak of the torsional resonance magnitude becomes lower than the input impedance of the converter or the resonance frequency occurs where the phase angle of the input impedance behaves between ±90°. However, the former is unrealistic as B_{s} is normally very small where it can be ignored in stability studies and the latter one does not sound practical since the frequency of the oscillatory modes can be considered as constant because of the drive-train components. Therefore, the only way to guarantee the interconnected stability is to shape the input impedance of the PMSG-connected converter in the way that its phase angle behaves within ±90° like a passive circuit. Hence, no matter how the output impedance of the source behaves, there won't be any exceeds from the phase angle difference. In order to do that, if the stator resistance is designed so that the damping ratio of the input impedance denominator for the MPP at the highest operating wind speed becomes equal to 0.7, then it can be ensured that the input impedance phase angle behaves within ±90°. Therefore, the damping ratio of the input admittance can be defined as

$$\zeta = \frac{\frac{R_{\mathrm{s}}}{L} - \frac{\omega_{\mathrm{e}} L I_{\mathrm{q}}}{\lambda_{\mathrm{m}}}}{2\sqrt{\frac{3}{2}\frac{I_{\mathrm{q}}^2 \omega_{\mathrm{e}} L}{C_{\mathrm{dc}} U_{\mathrm{o}} \lambda_{\mathrm{m}}}\left(\frac{\omega_{\mathrm{e}} \lambda_{\mathrm{m}}}{U_{\mathrm{o}}} - D_{\mathrm{q}}\right)}}. \tag{5.23}$$

The sign of ζ is dependent on the numerator as $\frac{\omega_{\mathrm{e}} \lambda_{\mathrm{m}}}{U_{\mathrm{o}}} - D_{\mathrm{q}} \geq 0$, thus if the inequality of (5.23) holds true, ζ will be positive which means the input impedance has positive electrical damping at the low frequencies. Hence, to guarantee the passive electrical behaviour of the input impedance for all operating points, the inequality expressed by

$$\frac{R_{\mathrm{s}}}{L} > 1.4\sqrt{\frac{3}{2}\frac{I_{\mathrm{q}}^2 \omega_{\mathrm{e}} L}{C_{\mathrm{dc}} U_{\mathrm{o}} \lambda_{\mathrm{m}}}\left(\frac{\omega_{\mathrm{e}} \lambda_{\mathrm{m}}}{U_{\mathrm{o}}} - D_{\mathrm{q}}\right)} + \frac{\omega_{\mathrm{e}} L I_{\mathrm{q}}}{\lambda_{\mathrm{m}}} \tag{5.24}$$

should hold true. To meet the inequality of (5.24), an unrealistically large R_s is needed as normally $R_{\mathrm{s}} \ll \omega_{\mathrm{e}} L$ according to [33]. Besides that, in the direct-driven wind turbine applications where the large multipole PMSGs are used, the stator resistance is smaller, and the rotor angular speed is higher. Therefore, one can conclude that the input impedance of the PMSG-connected converter under the open-loop condition has the negative

electrical damping behaviour which leads to instability when it is connected to the wind turbine drive-train.

5.3 Stability assessment under open-loop

The effect of the WT drive-train dynamics can be included into the PMSG-connected converter dynamic model according to the method proposed in [34] where the dynamic representation of a cascaded connection of the source and converter is presented. Therefore, in this case, the transfer functions of the WT output impedance presented in (5.16) can be considered as the source dynamic and the PMSG-connected converter dynamic model presented in (3.50) can be taken as the converter. Hence, the dynamic characteristic of the control-to-output voltage transfer function of the PMSG-connected converter when the wind turbine dynamics is included can be expressed as

$$G_{\mathrm{co-q}}^{\mathrm{S}} = \frac{1 + Z_{\mathrm{oS}} Y_{\mathrm{in-q-inf}}}{1 + Z_{\mathrm{oS}} Y_{\mathrm{in-q}}} G_{\mathrm{co-q}}, \tag{5.25}$$

where the superscript 'S' refers to the dynamic of the WT. For the low frequencies $Y_{\mathrm{in-q-inf}}$ and $Y_{\mathrm{in-q}}$ can be approximated by setting $s \approx 0$. Hence, the transfer function of the control-to-output voltage $G_{\mathrm{co-q}}^{\mathrm{S}}$ can be obtained as

$$G_{\mathrm{co-q}}^{\mathrm{S}} = \frac{s^3 + \left(\frac{1}{R_{\mathrm{fc}}}\frac{(C_{\mathrm{t}}+C_{\mathrm{g}})}{C_{\mathrm{t}}C_{\mathrm{g}}} - \frac{1}{r_{\mathrm{dyn}}C_{\mathrm{t}}} + \frac{1}{R_{\mathrm{st}}C_{\mathrm{g}}}\right)s^2 + \left(\frac{L_{\mathrm{t}}(C_{\mathrm{t}}+C_{\mathrm{g}})}{C_{\mathrm{t}}C_{\mathrm{g}}} + \frac{\frac{1}{R_{\mathrm{fc}}} - \frac{1}{r_{\mathrm{dyn}}}}{R_{\mathrm{st}}C_{\mathrm{t}}C_{\mathrm{g}}}\right)s - \frac{L_{\mathrm{t}}}{r_{\mathrm{dyn}}C_{\mathrm{t}}C_{\mathrm{g}}} + \frac{L_{\mathrm{t}}}{R_{\mathrm{st}}C_{\mathrm{t}}C_{\mathrm{g}}}}{s^3 + \left(\frac{1}{R_{\mathrm{fc}}}\frac{(C_{\mathrm{t}}+C_{\mathrm{g}})}{C_{\mathrm{t}}C_{\mathrm{g}}} - \frac{1}{r_{\mathrm{dyn}}C_{\mathrm{t}}} + \frac{1}{R_{\mathrm{in}}C_{\mathrm{g}}}\right)s^2 + \left(\frac{L_{\mathrm{t}}(C_{\mathrm{t}}+C_{\mathrm{g}})}{C_{\mathrm{t}}C_{\mathrm{g}}} + \frac{\frac{1}{R_{\mathrm{fc}}} - \frac{1}{r_{\mathrm{dyn}}}}{R_{\mathrm{in}}C_{\mathrm{t}}C_{\mathrm{g}}}\right)s - \frac{L_{\mathrm{t}}}{r_{\mathrm{dyn}}C_{\mathrm{t}}C_{\mathrm{g}}} + \frac{L_{\mathrm{t}}}{R_{\mathrm{in}}C_{\mathrm{t}}C_{\mathrm{g}}}} G_{\mathrm{co-q}}, \tag{5.26}$$

where R_{st} represents the approximated value of the ideal input impedance $(1/\,Y_{\mathrm{in-q-inf}})$ for the low frequencies which is called static resistance. r_{dyn} denotes the dynamic resistance of the $T_t - \omega_t$ curve and the converter input impedance estimated for the low frequency is shown by R_{in}. The damping coefficient is indicated by $1/R_{\mathrm{fc}}$.

Considering $\frac{L_{\mathrm{t}}(C_{\mathrm{t}}+C_{\mathrm{g}})}{C_{\mathrm{t}}C_{\mathrm{g}}} \gg \frac{\frac{1}{R_{\mathrm{fc}}} - \frac{1}{r_{\mathrm{dyn}}}}{R_{\mathrm{in}}C_{\mathrm{t}}C_{\mathrm{g}}}$ and $\frac{L_{\mathrm{t}}(C_{\mathrm{t}}+C_{\mathrm{g}})}{C_{\mathrm{t}}C_{\mathrm{g}}} \gg \frac{\frac{1}{R_{\mathrm{fc}}} - \frac{1}{r_{\mathrm{dyn}}}}{R_{\mathrm{st}}C_{\mathrm{t}}C_{\mathrm{g}}}$, (5.26) simplifies as

$$G_{\mathrm{co-q}}^{\mathrm{S}} = \frac{s^3 + \left(\frac{1}{R_{\mathrm{fc}}}\frac{(C_{\mathrm{t}}+C_{\mathrm{g}})}{C_{\mathrm{t}}C_{\mathrm{g}}} - \frac{1}{r_{\mathrm{dyn}}C_{\mathrm{t}}} + \frac{1}{R_{\mathrm{st}}C_{\mathrm{g}}}\right)s^2 + \left(\frac{L_{\mathrm{t}}(C_{\mathrm{t}}+C_{\mathrm{g}})}{C_{\mathrm{t}}C_{\mathrm{g}}}\right)s + \frac{L_{\mathrm{t}}}{C_{\mathrm{t}}C_{\mathrm{g}}}\left(\frac{1}{R_{\mathrm{st}}} - \frac{1}{r_{\mathrm{dyn}}}\right)}{s^3 + \left(\frac{1}{R_{\mathrm{fc}}}\frac{(C_{\mathrm{t}}+C_{\mathrm{g}})}{C_{\mathrm{t}}C_{\mathrm{g}}} - \frac{1}{r_{\mathrm{dyn}}C_{\mathrm{t}}} + \frac{1}{R_{\mathrm{in}}C_{\mathrm{g}}}\right)s^2 + \left(\frac{L_{\mathrm{t}}(C_{\mathrm{t}}+C_{\mathrm{g}})}{C_{\mathrm{t}}C_{\mathrm{g}}}\right)s + \frac{L_{\mathrm{t}}}{C_{\mathrm{t}}C_{\mathrm{g}}}\left(\frac{1}{R_{\mathrm{in}}} - \frac{1}{r_{\mathrm{dyn}}}\right)} G_{\mathrm{co-q}}. \tag{5.27}$$

From (5.27), the low frequency poles and zeros of the control-to-output voltage transfer function, correspond to the drive-train of the wind turbine coupled to the PMSG-connected converter, can be estimated as

$$\omega_{\mathrm{Lp1}} \approx \frac{\left(\frac{1}{R_{\mathrm{in}}} - \frac{1}{r_{\mathrm{dyn}}}\right)}{C_{\mathrm{t}} + C_{\mathrm{g}}},$$
$$\omega_{\mathrm{Lz1}} \approx \frac{\left(\frac{1}{R_{\mathrm{st}}} - \frac{1}{r_{\mathrm{dyn}}}\right)}{C_{\mathrm{t}} + C_{\mathrm{g}}}, \tag{5.28}$$

$$\omega_{\mathrm{Lp2,3}} \approx \frac{\frac{1}{R_{\mathrm{fc}}}\frac{\left(C_{\mathrm{t}} + C_{\mathrm{g}}\right)}{C_{\mathrm{t}}C_{\mathrm{g}}} - \frac{1}{r_{\mathrm{dyn}}C_{\mathrm{t}}} + \frac{1}{R_{\mathrm{in}}C_{\mathrm{g}}}}{2} \pm j\sqrt{\frac{L_{\mathrm{t}}\left(C_{\mathrm{t}} + C_{\mathrm{g}}\right)}{C_{\mathrm{t}}C_{\mathrm{g}}}},$$
$$\omega_{\mathrm{Lz2,3}} \approx \frac{\frac{1}{R_{\mathrm{fc}}}\frac{\left(C_{\mathrm{t}} + C_{\mathrm{g}}\right)}{C_{\mathrm{t}}C_{\mathrm{g}}} - \frac{1}{r_{\mathrm{dyn}}C_{\mathrm{t}}} + \frac{1}{R_{\mathrm{st}}C_{\mathrm{g}}}}{2} \pm j\sqrt{\frac{L_{\mathrm{t}}\left(C_{\mathrm{t}} + C_{\mathrm{g}}\right)}{C_{\mathrm{t}}C_{\mathrm{g}}}}, \tag{5.29}$$

where the roots of the numerator are shown by ω_{Lz}, and ω_{Lp} is used to describe the denominator roots for the low frequencies. As can be seen from (5.28), the real pole and zero shown by ω_{Lp1} and ω_{Lz1} respectively, are directly dependent on the operating point and they can be shifted to the left-half or the right-half of the complex plane.

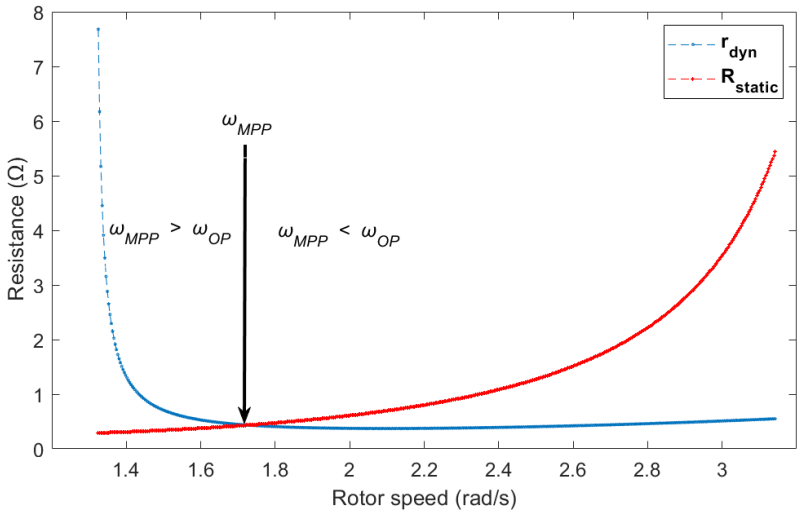

***Figure 24**. Dynamic resistance and static resistance of WTG-coupled converter within the generator region of $T_t - \omega_t$ curve*

According to Figure 24, the location of ω_{Lz1} changes as

$$\begin{aligned} &\omega_{\mathrm{MPP}} < \omega_{\mathrm{OP}} \quad r_{\mathrm{dyn}} < R_{\mathrm{st}} \Rightarrow \omega_{\mathrm{Lz1}} < 0 \ \ \mathrm{LHP} \\ &\omega_{\mathrm{MPP}} = \omega_{\mathrm{OP}} \quad r_{\mathrm{dyn}} = R_{\mathrm{st}} \Rightarrow \omega_{\mathrm{Lz1}} = 0 \ \ \mathrm{Origin}, \\ &\omega_{\mathrm{MPP}} > \omega_{\mathrm{OP}} \quad r_{\mathrm{dyn}} > R_{\mathrm{st}} \Rightarrow \omega_{\mathrm{Lz1}} > 0 \ \ \mathrm{RHP} \end{aligned} \tag{5.30}$$

where ω_{MPP} represents the rotor speed in which the maximum power occurs for a certain wind speed and ω_{OP} is the operating point rotor speed. Changes in the operating point shifts the location of ω_{Lp1} where it can be a right-half-plane, or a left-half-plane pole as described by

$$\begin{aligned} &r_{\mathrm{dyn}} < R_{\mathrm{in}} \Rightarrow \omega_{\mathrm{Lp1}} < 0 \ \ \mathrm{LHP} \\ &r_{\mathrm{dyn}} = R_{\mathrm{in}} \Rightarrow \omega_{\mathrm{Lp1}} = 0 \ \ \mathrm{Origin}, \\ &r_{\mathrm{dyn}} > R_{\mathrm{in}} \Rightarrow \omega_{\mathrm{Lp1}} > 0 \ \ \mathrm{RHP} \end{aligned} \tag{5.31}$$

In addition, the sign of the transfer function of $G_{\mathrm{co-q}}^{\mathrm{S}}$ for the low frequency range can be determined as follows:

$$\frac{\frac{1}{R_{\mathrm{st}}}-\frac{1}{r_{\mathrm{dyn}}}}{\frac{1}{R_{\mathrm{in}}}-\frac{1}{r_{\mathrm{dyn}}}}, \tag{5.32}$$

where R_{st} can be given as

$$R_{\mathrm{st}}=-\frac{E_{\mathrm{q}}}{I_{\mathrm{q}}}, \tag{5.33}$$

and R_{in} where the parasitic parameters are neglected can be approximated as

$$R_{\mathrm{in}} \approx \frac{\omega_e^2+\frac{3}{2}\frac{D_{\mathrm{d}}^2+D_{\mathrm{q}}^2}{LC_{\mathrm{dc}}}}{-\frac{\omega_{\mathrm{e}}I_{\mathrm{q}}}{\lambda_{\mathrm{m}}}}. \tag{5.34}$$

It is worth noting that, considering (5.33) and (5.34), if the DC-link capacitor is assumed to be very high or a voltage source considered to be the output of the converter, then it can be concluded that $R_{\mathrm{st}} \approx R_{\mathrm{in}}$ so that the real zero and real pole exits in $G_{\mathrm{co-q}}^{\mathrm{S}}$ will cancel each other.

As estimated in (5.29), the resonance frequency of $G_{\mathrm{co-q}}^{\mathrm{S}}$ caused by the drive-train torsional modes only relies on the natural frequency of the drive-train and the effect of operating point can be neglected. However, the real part of $\omega_{\mathrm{Lp2,3}}$ and $\omega_{\mathrm{Lz2,3}}$ are dependent on the operating point. In (5.29), the damping coefficient can be ignored in the WECS dynamic stability because its value is negligible due to regular lubrication conducted during routine maintenance service. Moreover, it can be assumed that the turbine inertia is much higher compared to the machine inertia ($J_{\mathrm{t}} \gg J_{\mathrm{g}}$), which is a reasonable assumption in the case of the large direct-driven WECSs. Hence, the real part of $\omega_{\mathrm{Lp2,3}}$ and $\omega_{\mathrm{Lz2,3}}$ can be approximated as

$$\left(\frac{1}{2R_{\mathrm{fc}}C_{\mathrm{g}}}-\frac{1}{2r_{\mathrm{dyn}}C_{\mathrm{t}}}\right) \ll \frac{1}{2R_{\mathrm{st}}C_{\mathrm{g}}}, \qquad \left(\frac{1}{2R_{\mathrm{fc}}C_{\mathrm{g}}}-\frac{1}{2r_{\mathrm{dyn}}C_{\mathrm{t}}}\right) \ll \frac{1}{2R_{\mathrm{in}}C_{\mathrm{g}}}. \tag{5.35}$$

Therefore, one concludes that if the inequality of (5.35) holds true, there will be a pair of complex RHP-zeros and a pair of complex RHP-poles for all the operating points which means the WTG-coupled converter is inherently unstable because of the torsional modes.

Analysing the effect of the WT dynamics on the control-to-output voltage transfer function and deriving the poles and zeros can be used to design a stable and robust controller for the DC-link voltage. According to [35], to ensure the stable operation of a control loop with a reasonable performance, the crossover frequency of the control loop must be

greater than a RHP-pole and smaller than the RHP-zero frequency. However, as expressed in (5.29), RHP-zeros and RHP-poles appear at the same frequency in $G_{\mathrm{co-q}}^{\mathrm{S}}$. Hence, controlling the DC-link voltage through $G_{\mathrm{co-q}}^{\mathrm{S}}$ because of its dynamic behavior cannot be practical.

5.4 Stability assessment under current-control loop

As discussed in the previous section, the control-to-output voltage cannot be used to control the DC-link voltage under the open-loop. Hence, the aim in this part is to study the WTG-connected converter dynamic under the closed-loop current control. The control-to-inductor current of the WTG-coupled converter for the q-channel $G_{\mathrm{ci-q}}^{\mathrm{S}}$ can be defined as

$$G_{\mathrm{ci-q}}^{\mathrm{S}} = \frac{G_{\mathrm{ci-q}}}{1 + Z_{\mathrm{oS}} Y_{\mathrm{in-q}}}. \tag{5.36}$$

In Chapter 4, the current controllers are designed based on the control-to-inductor current transfer function $G_{\mathrm{ci-q}}$ where the effect of the wind turbine dynamics are not included into the PMSG-connected converter dynamic model. However, it can be seen from (5.36) that the transfer function can be affected by the wind turbine dynamics. Based on the same assumptions as considered in (5.27), $G_{\mathrm{ci-q}}^{\mathrm{S}}$ can be approximated for the low frequencies as

$$G_{\mathrm{ci-q}}^{\mathrm{S}} = \frac{s^3 + \left(\frac{1}{R_{\mathrm{fc}}}\frac{(C_{\mathrm{t}} + C_{\mathrm{g}})}{C_{\mathrm{t}}C_{\mathrm{g}}} - \frac{1}{r_{\mathrm{dyn}}C_{\mathrm{t}}}\right)s^2 + \left(\frac{L_{\mathrm{t}}(C_{\mathrm{t}} + C_{\mathrm{g}})}{C_{\mathrm{t}}C_{\mathrm{g}}}\right)s - \frac{L_{\mathrm{t}}}{r_{\mathrm{dyn}}C_{\mathrm{t}}C_{\mathrm{g}}}}{s^3 + \left(\frac{1}{R_{\mathrm{fc}}}\frac{(C_{\mathrm{t}} + C_{\mathrm{g}})}{C_{\mathrm{t}}C_{\mathrm{g}}} - \frac{1}{r_{\mathrm{dyn}}C_{\mathrm{t}}} + \frac{1}{R_{\mathrm{in}}C_{\mathrm{g}}}\right)s^2 + \left(\frac{L_{\mathrm{t}}(C_{\mathrm{t}} + C_{\mathrm{g}})}{C_{\mathrm{t}}C_{\mathrm{g}}}\right)s + \frac{L_{\mathrm{t}}}{C_{\mathrm{t}}C_{\mathrm{g}}}\left(\frac{1}{R_{\mathrm{in}}} - \frac{1}{r_{\mathrm{dyn}}}\right)} G_{\mathrm{ci-q}}. \tag{5.37}$$

The roots of the denominator will be the same as the control-to-output voltage transfer function in the WTG-coupled converter, but the nominator will be different as the ideal input admittance is not part of it. Therefore, the complex RHP-poles appears in $G_{\mathrm{co-q}}^{\mathrm{S}}$ can be seen in the transfer function of the control-to-inductor current as they share the same denominator. However, $G_{\mathrm{ci-q}}^{\mathrm{S}}$ does not contain the complex RHP-zeros as appears in $G_{\mathrm{co-q}}^{\mathrm{S}}$ thus the control-to-inductor current transfer function of the WTG-coupled converter can be stabilized if the bandwidth of the current control loop is designed to be larger than the frequency of RHP-poles. As can be observed in the nominator of (5.37), the same real zero and a pair of complex zeros as derived from the output impedance of the source can be extracted here which means that there will be a pair of complex LHP-zeros in the nominator that is close to the imaginary axe.

The control-to-inductor current of the q-channel in the WTG-coupled converter does not contain any RHP-zero thus there will be no maximum constraint on the bandwidth of the

current control loop. Hence, the current controller design rules used in Chapter 4 will be valid even with considering the effect of the wind turbine dynamics and the stability of the interconnected system under the current control-loop can be evaluated.

Figure 25 illustrates the output impedance of the wind turbine against the input impedance of the PMSG-connected converter under open-loop condition $Z_{\mathrm{in-q}} = 1/Y_{\mathrm{in-q}}$ and the input impedance under the closed-loop current control $Z_{\mathrm{in-q-c}} = 1/Y_{\mathrm{in-q-c}}$. As shown, under the current control, the magnitude of the input impedance significantly increases while the phase angle approximately remains the same within the low frequency range. Therefore, although the phase difference between the output impedance and the input impedance exceeds 180°, the magnitude of $Z_{\mathrm{in-q-c}}$ is larger than Z_{oS} (indicated by Z_{out} in Figure 25). Hence, it can be concluded that the under the current loop control, the interconnected system can be stabilized as long as the crossover frequency of the loop gain is high enough to damp the torsional resonance.

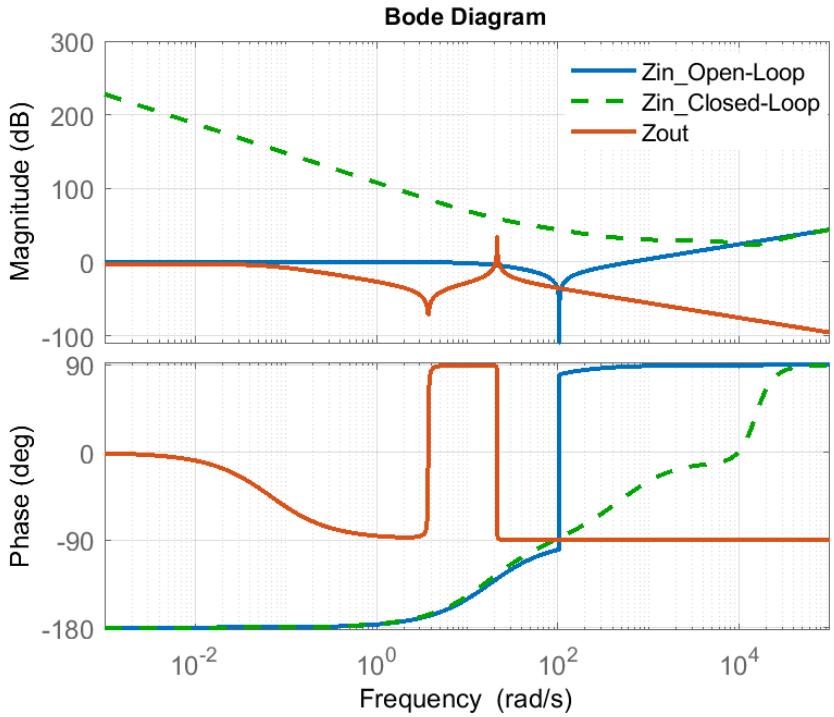

***Figure 25**. Bode diagram of WT output impedance versus input impedance of PMSG*

Now the current controlled control-to-output voltage transfer function of the WTG-coupled converter can be given as

$$G^{\mathrm{S}}_{\mathrm{co-q-c}} = \frac{1 + Z_{\mathrm{oS}} Y_{\mathrm{in-q-inf}}}{1 + Z_{\mathrm{oS}} Y_{\mathrm{in-q-c}}} G_{\mathrm{co-q-c}} \,. \tag{5.38}$$

Considering $\frac{L_{\mathrm{in-q}}}{1+L_{\mathrm{in-q}}} \approx 1$ as the current control loop is designed to be fast enough, the control-to-output voltage transfer function under the closed-loop current control can be approximated as

$$G^{S}_{\mathrm{co-q-c}} \approx \frac{s^3 + \left(\frac{1}{R_{\mathrm{fc}}}\frac{(C_{\mathrm{t}} + C_{\mathrm{g}})}{C_{\mathrm{t}}C_{\mathrm{g}}} - \frac{1}{r_{\mathrm{dyn}}C_{\mathrm{t}}} + \frac{1}{R_{\mathrm{st}}C_{\mathrm{g}}}\right) s^2 + \left(\frac{L_{\mathrm{t}}(C_{\mathrm{t}} + C_{\mathrm{g}})}{C_{\mathrm{t}}C_{\mathrm{g}}}\right) s + \frac{L_{\mathrm{t}}}{C_{\mathrm{t}}C_{\mathrm{g}}}\left(\frac{1}{R_{\mathrm{st}}} - \frac{1}{r_{\mathrm{dyn}}}\right)}{s^3 + \left(\frac{1}{R_{\mathrm{fc}}}\frac{(C_{\mathrm{t}} + C_{\mathrm{g}})}{C_{\mathrm{t}}C_{\mathrm{g}}} - \frac{1}{r_{\mathrm{dyn}}C_{\mathrm{t}}}\right) s^2 + \left(\frac{L_{\mathrm{t}}(C_{\mathrm{t}} + C_{\mathrm{g}})}{C_{\mathrm{t}}C_{\mathrm{g}}}\right) s - \frac{L_{\mathrm{t}}}{r_{\mathrm{dyn}}C_{\mathrm{t}}C_{\mathrm{g}}}} G_{\mathrm{co-q-c}} \cdot (5.39)$$

From (5.39), it can be realized that the RHP-poles in the transfer function are disappeared due to closed-loop current control and the roots of the denominator are exactly the same as the output impedance of the wind turbine. However, the roots of the nominator are the same as the control-to-output voltage under the open-loop condition which means the transfer function contains a real-RHP zero in high frequency and a pair of complex RHP-zeros in the low frequency. Therefore, it can be concluded that the control-to-output voltage of the WTG-coupled converter can be used to regulate the DC-link voltage when the current control is applied because there are only RHP-zeros in the transfer function that can be stabilized through cascade control scheme. Hence, in the next chapter, the dynamic of the WTG-coupled converter under the DC-link voltage control loop will be discussed.

6. WTG-COUPLED CONVERTER UNDER DC-LINK VOLTAGE CONTROL

In the previous chapter, the dynamic behaviour of the control-to-output voltage transfer function under open-loop condition and the current control was discussed where it revealed that unlike the open-loop condition, the transfer function can be used for the DC-link voltage control when the closed-loop current control is applied. However, to sufficiently damp the drive-train oscillations and to ensure the stable operation for all the operating conditions, a cascaded control scheme is needed. Moreover, the stability of the WTG-coupled converter under the output voltage closed-loop control must be studied for both the maximum power point tracking (MPPT) and controlled power (CP) modes.

6.1 Stable operation under MPPT mode

According to [34], to assess the stability of the PMSG-connected converter, the effect of the load dynamics on the converter stability must also be considered. Therefore, the dynamic of P_{MPPT} which is directly connected to the generator rotor speed needs to be considered into the study.

The dynamic model of the DC-link can be expressed as

$$C_{\mathrm{dc}}\frac{du_{\mathrm{o}}}{dt}=\frac{P_{\mathrm{in}}}{u_{\mathrm{o}}}-\frac{P_{\mathrm{out}}}{u_{\mathrm{o}}}, \tag{6.1}$$

where P_{in} represents the power generated by wind turbine and transferred into the generator-connected converter and P_{out} is the grid power which is determined by the active power controller of the grid-side inverter. The small-signal model of the DC-link under the MPPT mode can be given as

$$C_{\mathrm{dc}}\frac{d\hat{u}_{\mathrm{o}}}{dt}=\frac{\hat{p}_{\mathrm{in}}}{U_{\mathrm{o}}}-\frac{P_{\mathrm{in}}}{U_{\mathrm{o}}^2}\hat{u}_{\mathrm{dc}}-\frac{\hat{p}_{\mathrm{out}}}{U_{\mathrm{o}}}+\frac{P_{\mathrm{out}}}{U_{\mathrm{o}}^2}\hat{u}_{\mathrm{o}}\,. \tag{6.2}$$

Neglecting power losses in the converter and generator, the power transformed to the grid can be taken equal to the extracted power from the wind turbine that is $P_{\mathrm{in}}\approx P_{\mathrm{out}}$. Therefore, (6.2) can be simplified as

$$C_{\mathrm{dc}}\frac{d\hat{u}_{\mathrm{o}}}{dt}=\frac{\hat{p}_{\mathrm{in}}}{U_{\mathrm{o}}}-\frac{\hat{p}_{\mathrm{out}}}{U_{\mathrm{o}}}\,. \tag{6.3}$$

Since the MPPT mode is the case in this section, as explained in Chapter 4, P_{MPPT} can be taken as the grid power if the active power control loop in the grid-side inverter is assumed to be fast. Hence, P_{out} can be substituted by P_{MPPT} where the dynamics of the output power can be obtained as

$$\hat{p}_{\mathrm{out}}=\hat{p}_{\mathrm{MPPT}}=3K_{\mathrm{opt}}\omega_{\mathrm{g0}}^2\hat{\omega}_{\mathrm{g}}\,, \tag{6.4}$$

where $\widehat{\omega}_{\mathrm{g}}$ can be eliminated by substituting (5.7) into (6.4), so that the dynamic of the output power can be extracted as

$$\hat{p}_{\mathrm{MPPT}} = 3K_{\mathrm{opt}}\omega_{\mathrm{g0}}^{2}\frac{-(J_{\mathrm{t}}s^{2} + \gamma s + K_{\mathrm{s}})}{J_{\mathrm{t}}J_{\mathrm{g}}s^{3} + J_{\mathrm{g}}\gamma\, s^{2} + K_{\mathrm{s}}(J_{\mathrm{t}} + J_{\mathrm{g}})s + K_{\mathrm{s}}\gamma}\hat{T}_{\mathrm{g}}\,. \tag{6.5}$$

Considering the dynamics of the output power into the WTG-coupled converter under the current control, the control-to-output voltage control $G_{\mathrm{co-q-c}}^{\mathrm{S}}$ derived in Chapter 5 can be presented as

$$G_{\mathrm{co-q-c}}^{\mathrm{SL}} = \left(\frac{1 + Z_{\mathrm{oS}}Y_{\mathrm{in-q-inf}}}{1 + Z_{\mathrm{oS}}Y_{\mathrm{in-q-c}}} - 3K_{\mathrm{opt}}\omega_{\mathrm{g0}}^{2}Z_{\mathrm{oS}}\right)G_{\mathrm{co-q-c}}\,, \tag{6.6}$$

where the superscript 'L' represents the effect of the active power reference in the MPPT mode. As the bandwidth of the current control loop is assumed to be high, $(1 + Z_{\mathrm{oS}}Y_{\mathrm{in-q-c}}) \approx 1$ and can be neglected thus the transfer function of (6.6) can be simplified as

$$G_{\mathrm{co-q-c}}^{\mathrm{SL}} = \left(1 + (Y_{\mathrm{in-q-inf}} - 3K_{\mathrm{opt}}\omega_{\mathrm{g0}}^{2})Z_{\mathrm{oS}}\right)G_{\mathrm{co-q-c}}\,. \tag{6.7}$$

For the low frequency, $G_{\mathrm{co-q-c}}^{\mathrm{SL}}$ can be approximated as

$$G_{\mathrm{co-q-c}}^{\mathrm{SL}} \approx \frac{s^{3}+\left(\frac{1}{R_{\mathrm{fc}}}\frac{(C_{\mathrm{t}}+C_{\mathrm{g}})}{C_{\mathrm{t}}C_{\mathrm{g}}}-\frac{1}{r_{\mathrm{dyn}}C_{\mathrm{t}}}+\frac{1}{C_{\mathrm{g}}}\left(\frac{1}{R_{\mathrm{st}}}+\frac{1}{r_{\mathrm{mppt}}}\right)\right)s^{2}+\left(\frac{L_{\mathrm{t}}(C_{\mathrm{t}}+C_{\mathrm{g}})}{C_{\mathrm{t}}C_{\mathrm{g}}}+\frac{1}{C_{\mathrm{g}}}\left(\frac{1}{R_{\mathrm{st}}}+\frac{1}{r_{\mathrm{mppt}}}\right)\frac{\frac{1}{R_{\mathrm{fc}}}-\frac{1}{r_{\mathrm{dyn}}}}{R_{\mathrm{st}}C_{\mathrm{t}}C_{\mathrm{g}}}\right)s-\frac{L_{\mathrm{t}}}{C_{\mathrm{t}}}\left(\frac{1}{r_{\mathrm{dyn}}C_{\mathrm{g}}}-\frac{1}{C_{\mathrm{g}}}\left(\frac{1}{R_{\mathrm{st}}}+\frac{1}{r_{\mathrm{mppt}}}\right)\right)}{s^{3}+\left(\frac{1}{R_{\mathrm{fc}}}\frac{(C_{\mathrm{t}}+C_{\mathrm{g}})}{C_{\mathrm{t}}C_{\mathrm{g}}}-\frac{1}{r_{\mathrm{dyn}}C_{\mathrm{t}}}\right)s^{2}+\left(\frac{L_{\mathrm{t}}(C_{\mathrm{t}}+C_{\mathrm{g}})}{C_{\mathrm{t}}C_{\mathrm{g}}}\right)s-\frac{L_{\mathrm{t}}}{r_{\mathrm{dyn}}C_{\mathrm{t}}C_{\mathrm{g}}}}, \tag{6.8}$$

where the dynamic resistance of the MPPT can be defined as

$$r_{\mathrm{mppt}} = \frac{K_{\mathrm{T}}^{2}}{3K_{\mathrm{opt}}\omega_{g0}^{2}}\,. \tag{6.9}$$

Furthermore, the following assumptions can be taken

$$\frac{L_{\mathrm{t}}(C_{\mathrm{t}} + C_{\mathrm{g}})}{C_{\mathrm{t}}C_{\mathrm{g}}} \gg \frac{1}{C_{\mathrm{g}}}\left(\frac{1}{R_{\mathrm{st}}} + \frac{1}{r_{\mathrm{mppt}}}\right)\frac{\frac{1}{R_{\mathrm{fc}}} - \frac{1}{r_{\mathrm{dyn}}}}{R_{\mathrm{st}}C_{\mathrm{t}}C_{\mathrm{g}}}\ ,\ \frac{1}{R_{\mathrm{fc}}}\frac{(C_{\mathrm{t}} + C_{\mathrm{g}})}{C_{\mathrm{t}}C_{\mathrm{g}}} - \frac{1}{r_{\mathrm{dyn}}C_{\mathrm{t}}} \ll \frac{1}{C_{\mathrm{g}}}\left(\frac{1}{R_{\mathrm{st}}} + \frac{1}{r_{\mathrm{mppt}}}\right). \tag{6.10}$$

Hence, $G_{\mathrm{co-q-c}}^{\mathrm{SL}}$ can be given as

$$G_{\mathrm{co-q-c}}^{\mathrm{SL}} \approx \frac{s^{3} + \left(\frac{1}{R_{\mathrm{st}}} + \frac{1}{r_{\mathrm{mppt}}}\right)s^{2} + \left(\frac{L_{\mathrm{t}}(C_{\mathrm{t}} + C_{\mathrm{g}})}{C_{\mathrm{t}}C_{\mathrm{g}}}\right)s - \frac{L_{\mathrm{t}}}{C_{\mathrm{t}}C_{\mathrm{g}}}\left(\frac{1}{r_{\mathrm{dyn}}} - \left(\frac{1}{R_{\mathrm{st}}} + \frac{1}{r_{\mathrm{mppt}}}\right)\right)}{s^{3} + \left(\frac{1}{R_{\mathrm{fc}}}\frac{(C_{\mathrm{t}} + C_{\mathrm{g}})}{C_{\mathrm{t}}C_{\mathrm{g}}} - \frac{1}{r_{\mathrm{dyn}}C_{\mathrm{t}}}\right)s^{2} + \left(\frac{L_{\mathrm{t}}(C_{\mathrm{t}} + C_{\mathrm{g}})}{C_{\mathrm{t}}C_{\mathrm{g}}}\right)s - \frac{L_{\mathrm{t}}}{r_{\mathrm{dyn}}C_{\mathrm{t}}C_{\mathrm{g}}}}. \tag{6.11}$$

It can be concluded from the approximated transfer function in (6.11) that as long as the dynamic resistance of the MPPT is smaller than the static resistance, the pair of complex RHP-zeros corresponding to the torsional mode of the drive-train dynamics are located in the left-half of the complex plane where they won't imposed any design limitations on the maximum bandwidth of the DC-link voltage control loop. However, $G_{\mathrm{co-q-c}}^{\mathrm{SL}}$ has a resonant behaviour at the torsional frequency that impose minimum limitations on the crossover frequency of the loop gain. Therefore, to ensure the stable operation under MPPT mode with a good transient performance, the crossover frequency of the DC-link voltage

control loop should be designed to be larger than the frequency of the oscillatory modes. Moreover, the real RHP-zero caused by the slow dynamic of the WT aerodynamic torque disappears if the following inequality holds true:

$$\frac{1}{r_{\mathrm{dyn}}C_{\mathrm{g}}}-\frac{1}{C_{\mathrm{g}}}\left(\frac{1}{R_{\mathrm{st}}}+\frac{1}{r_{\mathrm{mppt}}}\right)\leq 0\,. \tag{6.12}$$

Therefore, considering r_{mppt} is small enough that the transfer function of $G_{\mathrm{co-q-c}}^{\mathrm{SL}}$ contains no RHP-zero, the maximum possible bandwidth for the DC-link voltage control loop can be determined based on the frequency of the RHP-zero related to the electrical dynamic of the PMSG-connected converter. Consequently, one can conclude that the design rules explained in the chapter 4 can be valid when the output voltage-controlled WTG-coupled converter operates under the MPPT mode. The frequency response of the loop gain for the DC-link voltage-controlled WTG-coupled converter under the MPPT is illustrated in Figure 26 where it is verified through the simulation model.

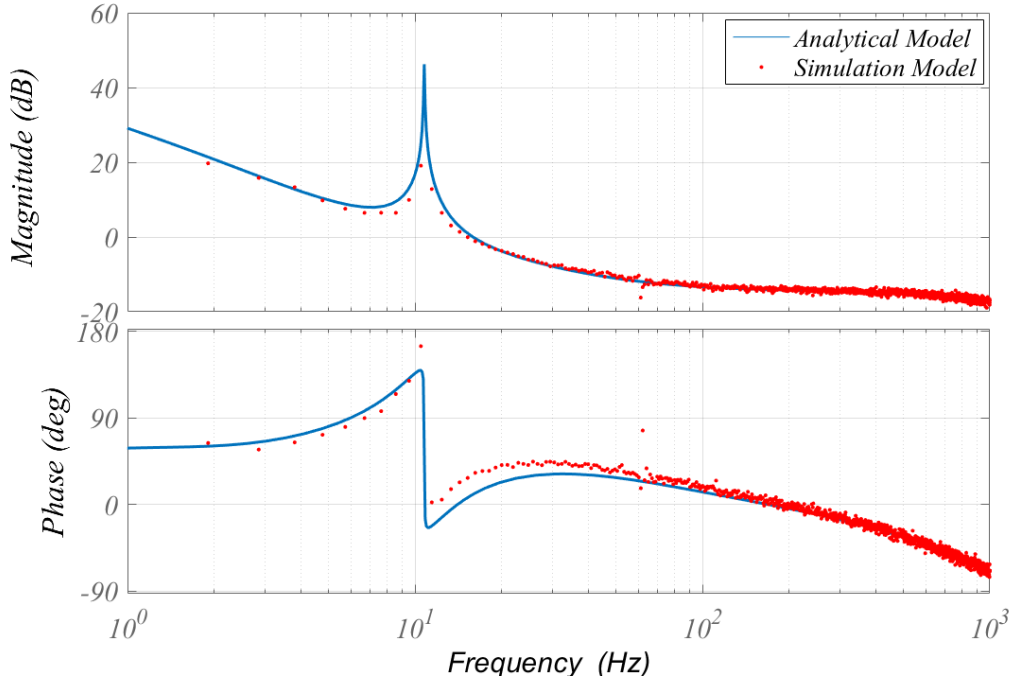

***Figure 26**. DC-Link voltage loop-gain under MPPT mode*

In the following, the simulation results of the output voltage-controlled WTG-coupled converter under the MPPT mode implemented in Matlab Simulink are demonstrated. The parameters of the case study are presented in Appendix C.

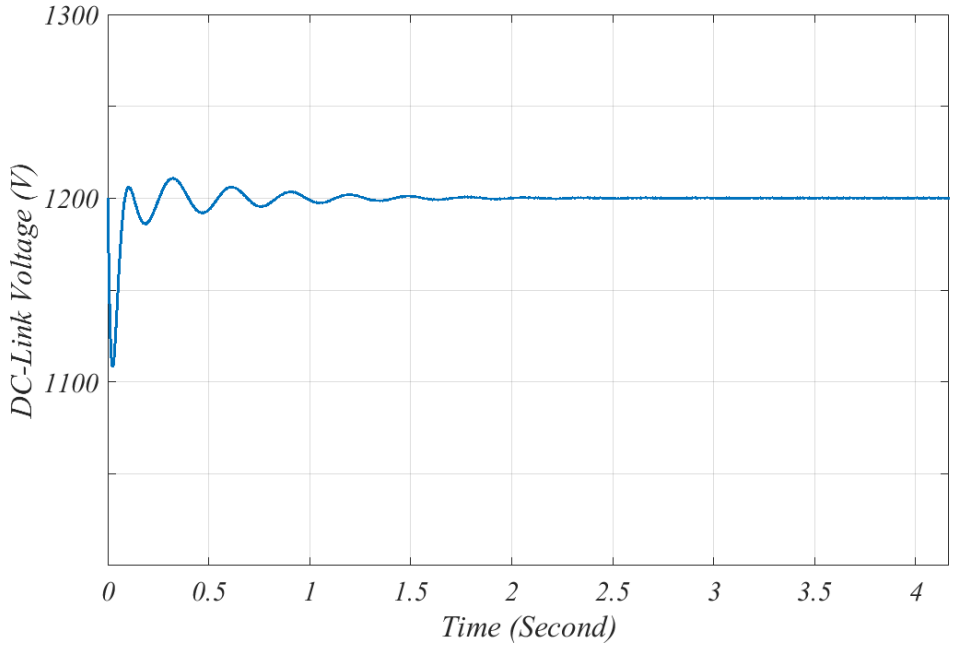

***Figure 27**. DC-Link voltage response during starting transient*

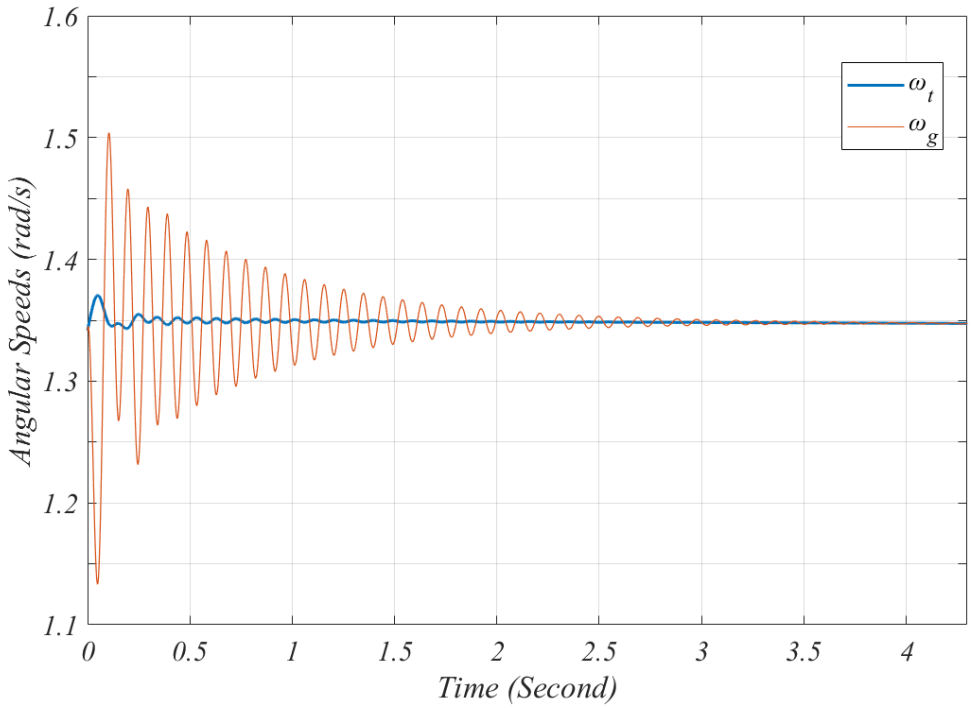

***Figure 28**. Turbine shaft and generator rotor speeds during starting transient*

The transient behaviour of the control system is tested under the step changes in wind speed. The wind turbine is initially started at 6 m/s where the oscillations caused by drive-train can be seen in the DC-link voltage transient performance illustrated in Figure 27. The oscillatory behaviour is mitigated after 1.5 s where the DC-link voltage settles down around the setpoint value which is in this case 1200 V. Figure 28 shows the oscillations with the natural frequency of the drive-train which appears in the transient behaviour of the angular speeds. As can be observed, the oscillatory behaviour is damped effectively

after a short time. So far, the wind speed is considered in the steady condition at the speed of 6 m/s where no disturbances are involved but afterwards, the wind speed is subjected to several step changes. First, at t = 5 s, the wind speed increases to 8 m/s and at t = 30 s when the angular speeds are settled down around $\omega_{\mathrm{MPP}(v_{\mathrm{w}}=8\ \mathrm{m/s})}$ then it steps up further to 10 m/s which is close to the maximum operating speed of the wind turbine. At t = 60 s where the wind turbine is almost producing its maximum power, the wind velocity decreases to 9 m/s and after 20 s it reduces further to 7 m/s.

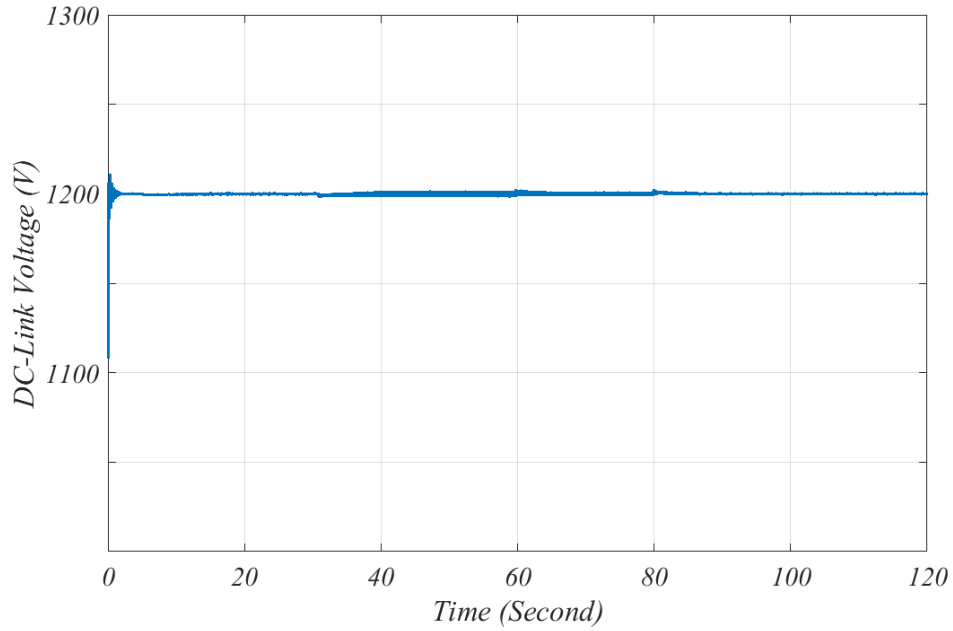

***Figure 29**. DC-Link voltage response under step changes in wind speed*

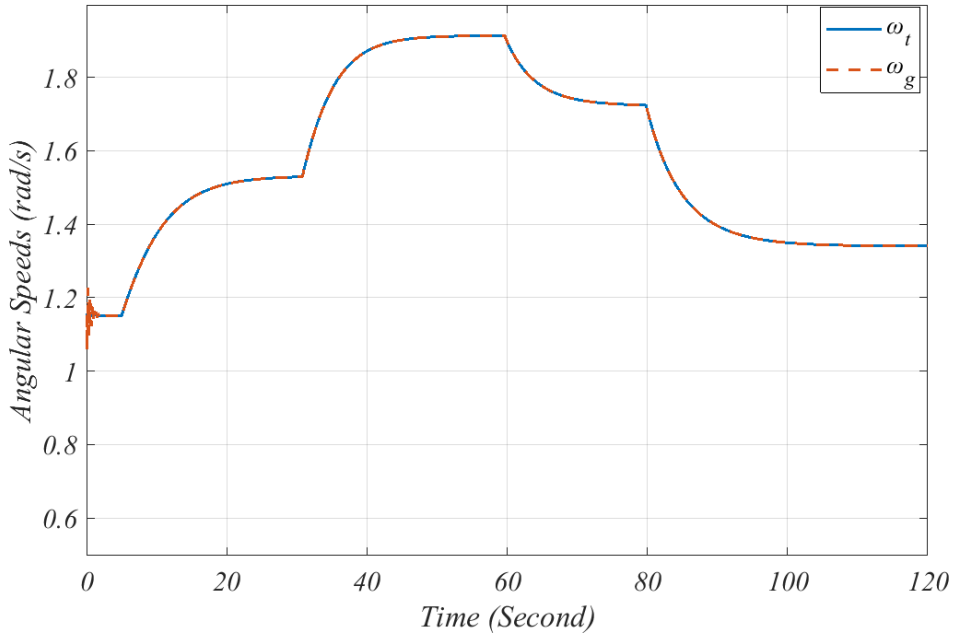

***Figure 30**. Turbine shaft and generator rotor speeds under step changes in wind speed*

Figure 29 indicates the DC-link voltage behaviour when the step changes apply to the wind speed and it can be seen that the effect of wind velocity variations on the voltage of the DC-link is negligible when the WTG-coupled converter operates under the MPPT mode. The response of the turbine angular speed and the generator rotor speed to the wind speed variations are illustrated in Figure 30. As can be realized, the angular speeds settle down at the steady-state point after changes in the wind velocity. However, the transient time response of the angular speeds to the wind speed step changes is much longer than the DC-link voltage due to the large inertia.

The initial response of the output voltage-controlled WTG-coupled converter under the MPPT mode is presented where the designed control system proved to be effective. Moreover, the performance of the control system when the wind turbine is subjected to the wind speed variations is demonstrated and the effectiveness of the controller can be concluded based on the simulation results.

6.2 Stable operation under CP mode

In the previous section, the stability of the output voltage-controlled WTG-coupled converter under the MPPT mode was evaluated where it was realized that the interconnected system is stable for the DC-link voltage controller designed for the PMSG-connected converter as the control-to-output voltage transfer function of the WTG-coupled converter contains no RHP-zero under the MPPT mode. Although the main function of the WECSs is extracting the maximum power of the wind energy, they also need to be capable of operating under the controlled power mode as one of the required grid codes. Therefore, in this section, the stability of the interconnected system under the CP mode will be discussed.

The stability of the interconnected system, where the WT dynamics are considered as the source and the PMSG-connected converter as the load, can be evaluated using the minor loop gain method. The input impedance obtained in Chapter 4 where the output voltage controller was designed based on the control-to-output voltage transfer function of the PMSG-connected converter is used here. As discussed before, $Z_{\mathrm{in-q-cv}} = 1/Y_{\mathrm{in-q-cv}}$ behaves like a negative resistor within the low frequencies where the drive-train torsional modes of the WTs usually oscillate. As can be found from Figure 31, the magnitude peak of the WT drive-train output impedance that occurs at the torsional frequency exceeds the input impedance of the output voltage-controlled PMSG-converter $\left(\left|Z_{\mathrm{oS}}/Z_{\mathrm{in-q-cv}}\right| \geq 1\right)$ while the phase difference exceeds 180° as expected because of the negative resistor-like behaviour of the input impedance thus the impedance ratio of the

interconnected system does not satisfy the Nyquist stability criterion and hence, the WTG-coupled converter under the DC-link voltage control with a fast regulation is unstable. In Figure 32, the transient performance of the DC-link voltage is shown where it can be seen that after switching the control mode from the MPPT to the controlled power mode at 2.7s, the DC-link voltage oscillates around the torsional frequency where it becomes unstable. The same transient behaviour occurs in the angular speed of turbine shaft and the rotor of the PMSG as illustrated in Figure 33.

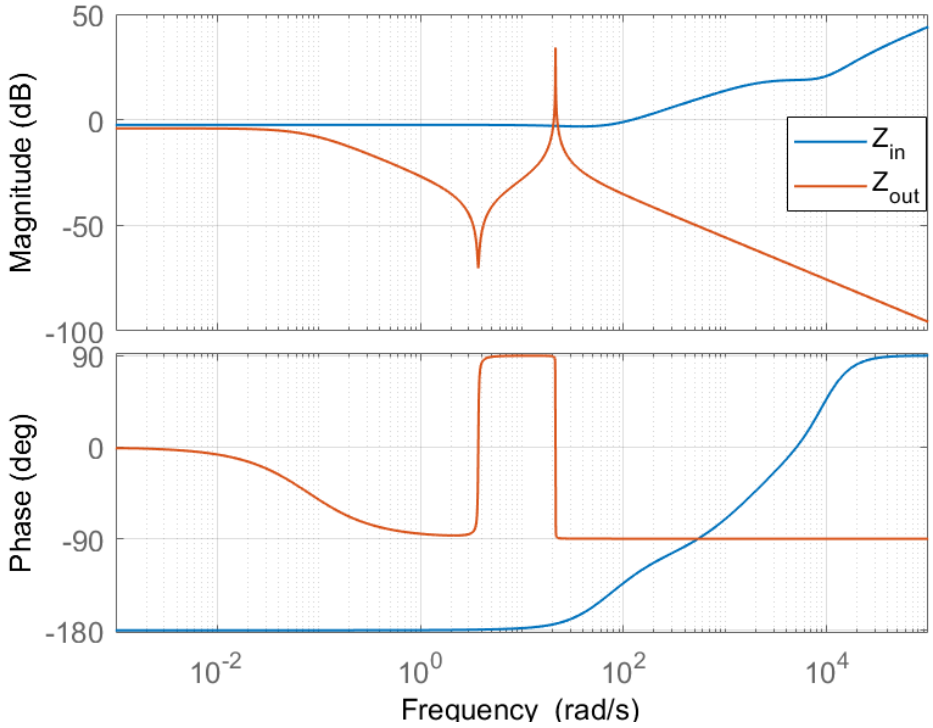

***Figure 31**. Frequency response of the input impedance of PMSG-connected converter under the DC voltage closed-loop over the output impedance of the WT.*

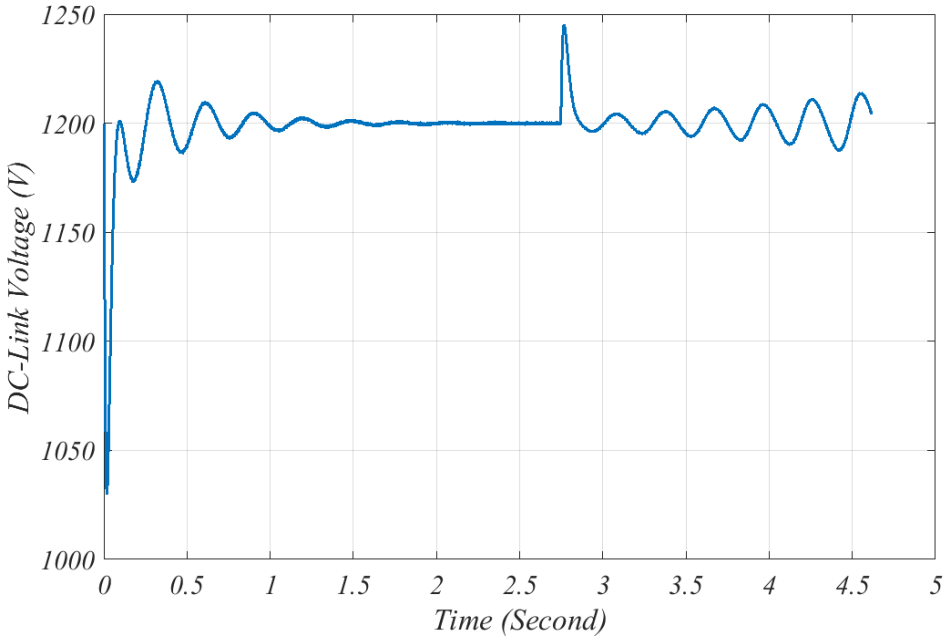

***Figure 32**. DC-Link voltage under transient from MPPT to CP mode*

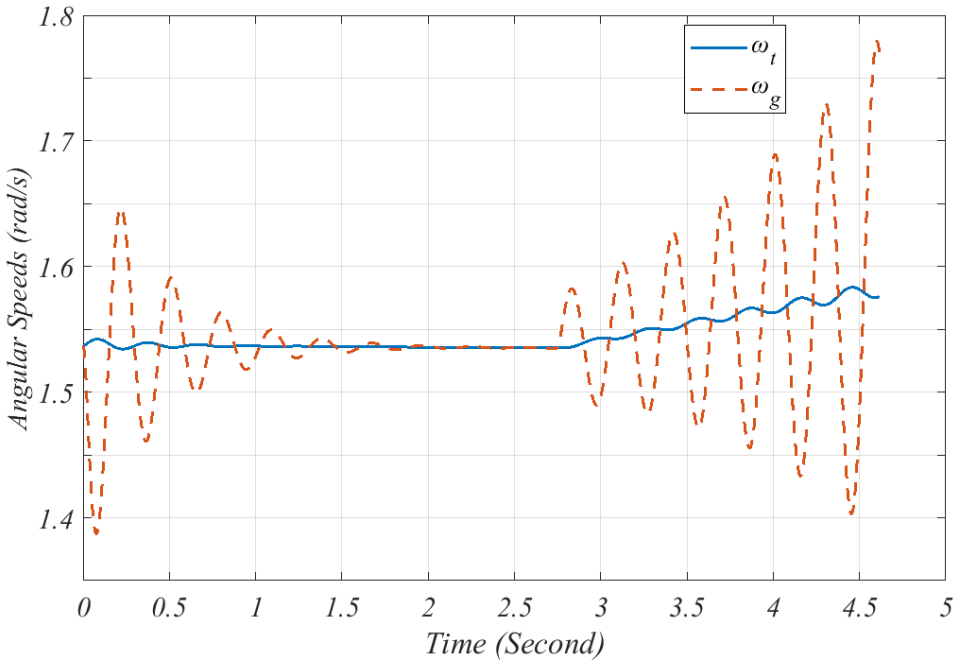

***Figure 33**. Turbine shaft speed and generator rotor speed under transient from MPPT to CP mode*

The transfer function of the input admittance of the PMSG-connected converter under the output voltage is presented as

$$Y_{\text{in-q-cv}} = \frac{Y_{\text{in-q-c}}}{1 + L_{\text{v}}} + \frac{L_{\text{v}}}{1 + L_{\text{v}}} Y_{\text{in-q-inf}} \ , \tag{6.13}$$

in which $Y_{\text{in-q-cv}}$ consists of two terms where both are affected by the loop gain of the DC-link voltage controller. The loop gain designed in Chapter 4 is tuned based on the control-to-output voltage transfer function obtained from the PMSG-connected converter in which it only contains a real RHP-zero located in high frequency. Hence, the crossover frequency of the loop control tuned so that the bandwidth of the DC-link voltage occurs in half of the RHP-zero frequency. Therefore, the loop gain can be considered much larger than 1 $(L_{\text{v}} \gg 1)$ within the frequencies below the controller crossover frequency so $L_{\text{v}}/(1 + L_{\text{v}}) \approx 1$. Moreover, the former term in (6.13) can be ignored for the low frequency studies as L_{v} is large and $Y_{\text{in-q-c}}$ is small. Therefore, the closed-loop input admittance of the PMSG-connected converter can be approximated as

$$Y_{\text{in-q-cv}} \approx Y_{\text{in-q-inf}} \ . \tag{6.14}$$

As explained earlier, the ideal input impedance $(R_{\text{st}} \approx {Y_{\text{in-q-inf}}}^{-1})$ of the PMSG-connected converter has negative resistor-like behaviour in the low frequencies. Therefore, from (6.14), one can conclude that the dynamic behaviour the input impedance of the PMSG-connected converter under the output voltage can be modelled as a negative pure resistor in the low frequencies.

In addition to the minor loop gain method, the denominator of $\left(1+\ Z_{\mathrm{oS}}Y_{\mathrm{in-q-cv}}\right)^{-1}$ can also be used for the stability studies where it must meet the Routh-Hurwitz criterion. This approach is more useful for the stability boundary determination thus it will be applied here [36]. Hence, by substituting $Y_{\mathrm{in-q-inf}}$ instead of $Y_{\mathrm{in-q-cv}}$, the following calculation can be used to analysis the interconnected system stability.

$$\begin{aligned}\left(1+\ Z_{\mathrm{oS}}Y_{\mathrm{in-q-cv}}\right)^{-1} &\approx (1+\ Z_{\mathrm{oS}}/R_{\mathrm{st}})^{-1}\\ &= \left(1+\frac{C_{\mathrm{t}}s^2+\ s/r_{\mathrm{dyn}}+\ L_{\mathrm{t}}}{C_{\mathrm{t}}C_{\mathrm{g}}R_{\mathrm{st}}s^3+\ R_{\mathrm{st}}/r_{\mathrm{dyn}}C_{\mathrm{g}}s^2+\ R_{\mathrm{st}}L_{\mathrm{t}}\left(C_{\mathrm{t}}+C_{\mathrm{g}}\right)s+\ R_{\mathrm{st}}/r_{\mathrm{dyn}}\,L_{\mathrm{t}}}\right)^{-1}\end{aligned}$$

$$= \frac{C_{\mathrm{t}}C_{\mathrm{g}}R_{\mathrm{st}}s^3+\ R_{\mathrm{st}}/r_{\mathrm{dyn}}C_{\mathrm{g}}s^2+\ R_{\mathrm{st}}L_{\mathrm{t}}\left(C_{\mathrm{t}}+C_{\mathrm{g}}\right)s+\ R_{\mathrm{st}}/r_{\mathrm{dyn}}\,L_{\mathrm{t}}}{C_{\mathrm{t}}C_{\mathrm{g}}R_{\mathrm{st}}s^3+\ \left(R_{\mathrm{st}}/r_{\mathrm{dyn}}C_{\mathrm{g}}+C_{\mathrm{t}}\right)s^2+\left(R_{\mathrm{st}}L_{\mathrm{t}}\left(C_{\mathrm{t}}+C_{\mathrm{g}}\right)+1/r_{\mathrm{dyn}}\right)s+L_{\mathrm{t}}\left(R_{\mathrm{st}}/r_{\mathrm{dyn}}+1\right)}$$

$$= \frac{C_{\mathrm{t}}C_{\mathrm{g}}s^3+\ C_{\mathrm{g}}/r_{\mathrm{dyn}}s^2+\ L_{\mathrm{t}}\left(C_{\mathrm{t}}+C_{\mathrm{g}}\right)s+\ L_{\mathrm{t}}/r_{\mathrm{dyn}}}{\underbrace{C_{\mathrm{t}}C_{\mathrm{g}}}_{a_0}\,s^3+\underbrace{\left(C_{\mathrm{g}}/r_{\mathrm{dyn}}+C_{\mathrm{t}}/R_{\mathrm{st}}\right)}_{a_1}s^2+\underbrace{\left(L_{\mathrm{t}}\left(C_{\mathrm{t}}+C_{\mathrm{g}}\right)+1/\left(R_{\mathrm{st}}r_{\mathrm{dyn}}\right)\right)}_{a_2}s+\underbrace{L_{\mathrm{t}}\left(1/r_{\mathrm{dyn}}+1/R_{\mathrm{st}}\right)}_{a_3}}. \quad (6.15)$$

Applying the Ruth-Hurwitz stability criterion to test the stability of the DC-link voltage control under the fast regulation, it can be realized that the control system is stable if the denominator of $(1+\ Z_{\mathrm{oS}}/R_{\mathrm{st}})^{-1}$ comply with the necessary conditions for the stability at all operating points. Therefore, all the inequalities given by

$$\begin{aligned} a_0 &> 0\\ a_1 &> 0\\ a_2 &> 0\\ a_3 &> 0 \end{aligned}, \quad (6.16)$$

must be hold true. If all the above conditions meet the stability requirement, the condition that all the roots are in the LHP is

$$a_1a_2\ -\ a_3a_0\ >0\,. \quad (6.17)$$

a_0 is always positive as it includes only the inertia values. However, a_1 is negative as the static resistance is negative and the turbine inertia C_{t} is much larger than the generator inertia C_{g}. Assuming $L_{\mathrm{t}}\left(C_{\mathrm{t}}+C_{\mathrm{g}}\right)\gg\ 1/\left(R_{\mathrm{st}}r_{\mathrm{dyn}}\right)$, a_2 can be considered as a positive value. Regarding the inequality of a_3, it can be positive or negative depending on the operating point. As discussed before, the sign of a_3 can be obtained as follows:

$$\begin{aligned} &\omega_{\mathrm{MPP}}<\omega_{\mathrm{OP}},\ r_{\mathrm{dyn}}<\ R_{\mathrm{st}}\ \Rightarrow\ \ a_3>0\\ &\omega_{\mathrm{MPP}}=\omega_{\mathrm{OP}},\ \ r_{\mathrm{dyn}}=\ R_{\mathrm{st}}\ \Rightarrow\ \ a_3=0\\ &\omega_{\mathrm{MPP}}>\omega_{\mathrm{OP}},\ r_{\mathrm{dyn}}>\ R_{\mathrm{st}}\ \Rightarrow\ \ a_3<0 \end{aligned}\,. \quad (6.18)$$

According to the Ruth-Hurwitz stability method, the system under the study is unstable even if only one of the inequalities does not meet the requirement. Moreover, the number

of RHP-poles can be obtained based on the number of changes in sign of the inequalities. The inequality of $a_1a_2 - a_3a_0 > 0$ is not needed to analysis for the stability assessment as all the coefficient of the polynomial are not positive.

Therefore, one concludes that the interconnected system is unstable under the fast DC-link voltage regulation because a_1 is negative. Besides that, if $a_3 > 0$, there will be only a pair of complex RHP-poles and for $a_3 < 0$, one real RHP-pole will appear in addition to the complex RHP-poles.

To avoid instability, the time response of the output voltage control should be slowed down which means the bandwidth of the control loop has to be decreased. Hence, the assumptions that considered in the case of the DC-link voltage under the fast control are no longer valid as $L_{\mathrm{v}}/(1 + L_{\mathrm{v}}) \approx 1$. Therefore, the DC-link dynamic and the PI-controller parameters must be considered in determining the stability conditions and the input impedance of the PMSG-connected converter under the output voltage control can be written as follows:

$$Y_{\mathrm{in-q-cv}} = \frac{Y_{\mathrm{in-q-c}}}{1 + L_{\mathrm{v}}} + \frac{L_{\mathrm{v}}}{1 + L_{\mathrm{v}}} Y_{\mathrm{in-q-inf}}\,. \tag{6.19}$$

As the low frequency range is the case, the first term of $Y_{\mathrm{in-q-cv}}$ can be ignored. Moreover, since the bandwidth of the current control loop is much faster than that of voltage control loop, $L_{\mathrm{in\_q}}/(1 + L_{\mathrm{in\_q}}) \approx 1$ and can be neglected in the low frequency stability studies. Therefore, $Y_{\mathrm{in-q-cv}}$ can be approximated as

$$Y_{\mathrm{in-q-cv}} = \frac{L_{\mathrm{v}}}{1 + L_{\mathrm{v}}} Y_{\mathrm{in-q-inf}}\ , \tag{6.20}$$

and by substituting (4.15) into (6.20), the input admittance under the cascaded control scheme can be expressed by

$$Y_{\mathrm{in-q-cv}} \approx \frac{K\,(\omega_{\mathrm{z}} - s)/(\omega_{\mathrm{p}} + s)K_{\mathrm{pv}}\,(s + \omega_{\mathrm{zv}})/s}{1 + K\,(\omega_{\mathrm{z}} - s)/(\omega_{\mathrm{p}} + s)K_{\mathrm{pv}}\,(s + \omega_{\mathrm{zv}})/s} \frac{1}{R_{\mathrm{st}}}. \tag{6.21}$$

Hence, the calculations for stability analysis based on the Ruth-Hurwitz method can be given as

$$\begin{aligned}
&(1 + Z_{\mathrm{oS}}\, Y_{\mathrm{in-q-cv}})^{-1} \\
&= \left(1 + \frac{C_{\mathrm{t}}s^2 + s/r_{\mathrm{dyn}} + L_{\mathrm{t}}}{C_{\mathrm{t}}C_{\mathrm{g}}s^3 + C_{\mathrm{g}}/r_{\mathrm{dyn}}s^2 + L_{\mathrm{t}}(C_{\mathrm{t}} + C_{\mathrm{g}})s + L_{\mathrm{t}}/r_{\mathrm{dyn}}} \frac{K\,(\omega_{\mathrm{z}} - s)/(\omega_{\mathrm{p}} + s)K_{\mathrm{pv}}\,(s + \omega_{\mathrm{zv}})/s}{1 + K\,(\omega_{\mathrm{z}} - s)/(\omega_{\mathrm{p}} + s)K_{\mathrm{pv}}\,(s + \omega_{\mathrm{zv}})/s} \frac{1}{R_{\mathrm{st}}}\right)^{-1} \\
&= \left(1 + \frac{KK_{\mathrm{pv}}(C_{\mathrm{t}}s^2 + s/r_{\mathrm{dyn}} + L_{\mathrm{t}})\,(\omega_{\mathrm{z}} - s)(s + \omega_{\mathrm{zv}})}{(C_{\mathrm{t}}C_{\mathrm{g}}s^3 + C_{\mathrm{g}}/r_{\mathrm{dyn}}s^2 + L_{\mathrm{t}}(C_{\mathrm{t}} + C_{\mathrm{g}})s + L_{\mathrm{t}}/r_{\mathrm{dyn}})\left((1 - KK_{\mathrm{pv}})s^2 + (\omega_{\mathrm{p}} + KK_{\mathrm{pv}}(\omega_{\mathrm{z}} - \omega_{\mathrm{zv}}))\right)s + KK_{\mathrm{iv}}\omega_{\mathrm{z}}} \frac{1}{R_{st}}\right)^{-1}
\end{aligned}$$

$$= \frac{\begin{pmatrix} C_t C_g R_{st}(1-KK_{pv})s^5 + \left(C_t C_g R_{st}\left(\omega_p + KK_{pv}(\omega_z-\omega_{zv})\right) + C_g\frac{R_{st}}{r_{dyn}}(1-KK_{pv})\right)s^4 \\ + \left(C_t C_g R_{st} KK_{iv}\omega_z + C_g\frac{R_{st}}{r_{dyn}}\left(\omega_p + KK_{pv}(\omega_z-\omega_{zv})\right) + L_t R_{st}(C_t+C_g)(1-KK_{pv})\right)s^3 \\ + \left(C_g\frac{R_{st}}{r_{dyn}}KK_{iv}\omega_z + L_t R_{st}(C_t+C_g)\left(\omega_p + KK_{pv}(\omega_z-\omega_{zv})\right) + L_t\frac{R_{st}}{r_{dyn}}(1-KK_{pv})\right)s^2 \\ + \left(L_t R_{st}(C_t+C_g)KK_{iv}\omega_z + L_t\frac{R_{st}}{r_{dyn}}\left(\omega_p + KK_{pv}(\omega_z-\omega_{zv})\right)\right)s + L_t\frac{R_{st}}{r_{dyn}}KK_{iv}\omega_z \end{pmatrix}}{\begin{pmatrix} C_t C_g R_{st}(1-KK_{pv})s^5 + \left(C_t C_g R_{st}\left(\omega_p + KK_{pv}(\omega_z-\omega_{zv})\right) + C_g\frac{R_{st}}{r_{dyn}}(1-KK_{pv}) - C_t KK_{pv}\right)s^4 \\ + \left(C_t C_g R_{st} KK_{iv}\omega_z + C_g\frac{R_{st}}{r_{dyn}}\left(\omega_p + KK_{pv}(\omega_z-\omega_{zv})\right) + L_t R_{st}(C_t+C_g)(1-KK_{pv}) + KK_{pv}\left(C_t(\omega_z-\omega_{zv}) - \frac{1}{r_{dyn}}\right)\right)s^3 \\ + \left(C_g\frac{R_{st}}{r_{dyn}}KK_{iv}\omega_z + L_t R_{st}(C_t+C_g)\left(\omega_p + KK_{pv}(\omega_z-\omega_{zv})\right) + L_t\frac{R_{st}}{r_{dyn}}(1-KK_{pv}) + KK_{pv}\left(C_t\omega_z\omega_{zv} + \frac{\omega_z-\omega_{zv}}{r_{dyn}}\right) - L_t\right)s^2 \\ + \left(L_t R_{st}(C_t+C_g)KK_{iv}\omega_z + L_t\frac{R_{st}}{r_{dyn}}\left(\omega_p + KK_{pv}(\omega_z-\omega_{zv})\right) + KK_{pv}\left(\frac{\omega_z\omega_{zv}}{r_{dyn}} + L_t(\omega_z-\omega_{zv})\right)\right)s + KK_{iv}\omega_z L_t\left(\frac{R_{st}}{r_{dyn}}+1\right) \end{pmatrix}}. \quad (6.22)$$

To study the stability of the interconnected system under the slow DC-link voltage control, the denominator of (6.22) must meet the Ruth-Hurwitz stability criterion. However, as studying a fifth order polynomial is complicated, the model needs to be simplified using reasonable assumptions.

In the case of the large wind turbines, the inertia of the turbine is much higher than that of the generator ($J_t \gg J_g$) thus the speed deviations on the turbine side can be assumed to be constant ω_t. Hence, the dynamic response of turbine will not affect the mechanical dynamic of the drive-train connected to the PMSG which is faster. Therefore, the wind turbine drive-train dynamics can be reformulated as follows

$$J_g\frac{d\hat{\omega}_g}{dt} = K_s\hat{\theta}_s - \hat{T}_g - B_s\hat{\omega}_g, \quad (6.23)$$

$$\frac{d\hat{\theta}_s}{dt} = -\hat{\omega}_g, \quad (6.24)$$

where the transfer function between the generator rotor speed and the electromechanical torque can be expressed as

$$\frac{\hat{\omega}_g}{\hat{T}_g} = -\frac{s}{J_g s^2 + B_s s + K_s}. \quad (6.25)$$

Neglecting the damping coefficient, the transfer function of (6.25) can be simplified as

$$\frac{\hat{\omega}_g}{\hat{T}_g} = -\frac{s/J_g}{s^2 + \frac{K_s}{J_g}}, \quad (6.26)$$

where it can be represented by the electrical expression as

$$Z_{oS} = \frac{s/C_g}{s^2 + \omega_n^2}. \quad (6.27)$$

By substituting (6.27) into (6.22), the characteristic polynomial can be presented as

$$\left(1 + Z_{oS}\,Y_{in-q-cv}\right)^{-1} = \left(1 + \frac{s/C_g}{s^2 + \omega_n^2}\frac{K(\omega_z - s)/(\omega_p + s)K_{pv}(s + \omega_{zv})/s}{1 + K(\omega_z - s)/(\omega_p + s)K_{pv}(s + \omega_{zv})/s}\frac{1}{R_{st}}\right)^{-1}$$

$$= \frac{\begin{pmatrix} C_{\mathrm{g}}R_{\mathrm{st}}(1-KK_{\mathrm{pv}})s^4 + C_{\mathrm{g}}R_{\mathrm{st}}\left(\omega_{\mathrm{p}} + KK_{\mathrm{pv}}(\omega_{\mathrm{z}}-\omega_{\mathrm{zv}})\right)s^3 \\ +C_{\mathrm{g}}R_{\mathrm{st}}\left(KK_{\mathrm{iv}}\omega_{\mathrm{z}} + \omega_{\mathrm{n}}^2\left(1-KK_{\mathrm{pv}}\right)\right)s^2 \\ +C_{\mathrm{g}}R_{\mathrm{st}}\omega_{\mathrm{n}}^2\left(\omega_{\mathrm{p}} + KK_{\mathrm{pv}}(\omega_{\mathrm{z}}-\omega_{\mathrm{zv}})\right)s + C_{\mathrm{g}}R_{\mathrm{st}}\omega_{\mathrm{n}}^2 KK_{\mathrm{iv}}\omega_{\mathrm{z}} \end{pmatrix}}{\begin{pmatrix} C_{\mathrm{g}}R_{\mathrm{st}}(1-KK_{\mathrm{pv}})s^4 + \left(C_{\mathrm{g}}R_{\mathrm{st}}\left(\omega_{\mathrm{p}} + KK_{\mathrm{pv}}(\omega_{\mathrm{z}}-\omega_{\mathrm{zv}})\right) - KK_{\mathrm{pv}}\right)s^3 \\ +\left(C_{\mathrm{g}}R_{\mathrm{st}}\left(KK_{\mathrm{iv}}\omega_{\mathrm{z}} + \omega_{\mathrm{n}}^2\left(1-KK_{\mathrm{pv}}\right)\right) + KK_{\mathrm{pv}}(\omega_{\mathrm{z}}-\omega_{\mathrm{zv}})\right)s^2 \\ +\left(C_{\mathrm{g}}R_{\mathrm{st}}\omega_{\mathrm{n}}^2\left(\omega_{\mathrm{p}} + KK_{\mathrm{pv}}(\omega_{\mathrm{z}}-\omega_{\mathrm{zv}})\right) + KK_{\mathrm{iv}}\omega_{\mathrm{z}}\right)s + C_{\mathrm{g}}R_{\mathrm{st}}\omega_{\mathrm{n}}^2 KK_{\mathrm{iv}}\omega_{\mathrm{z}} \end{pmatrix}}. \tag{6.28}$$

Now the Ruth-Hurwitz stability criterion can be applied on the denominator of (6.28) to assess the interconnected system stability under the output voltage control as expressed by

$$\begin{aligned} d(s) = {} & \underbrace{C_{\mathrm{g}}R_{\mathrm{st}}(1-KK_{\mathrm{pv}})}_{a_0}s^4 + \underbrace{\left(C_{\mathrm{g}}R_{\mathrm{st}}\left(\omega_{\mathrm{p}} + KK_{\mathrm{pv}}(\omega_{\mathrm{z}}-\omega_{\mathrm{zv}})\right) - KK_{\mathrm{pv}}\right)}_{a_1}s^3 \\ & + \underbrace{\left(C_{\mathrm{g}}R_{\mathrm{st}}\left(KK_{\mathrm{iv}}\omega_{\mathrm{z}} + \omega_{\mathrm{n}}^2\left(1-KK_{\mathrm{pv}}\right)\right) + KK_{\mathrm{pv}}(\omega_{\mathrm{z}}-\omega_{\mathrm{zv}})\right)}_{a_2}s^2 \\ & + \underbrace{\left(C_{\mathrm{g}}R_{\mathrm{st}}\omega_{\mathrm{n}}^2\left(\omega_{\mathrm{p}} + KK_{\mathrm{pv}}(\omega_{\mathrm{z}}-\omega_{\mathrm{zv}})\right) + KK_{\mathrm{iv}}\omega_{\mathrm{z}}\right)}_{a_3}s + \underbrace{C_{\mathrm{g}}R_{\mathrm{st}}\omega_{\mathrm{n}}^2 KK_{\mathrm{iv}}\omega_{\mathrm{z}}}_{a_4}. \end{aligned} \tag{6.29}$$

So, if all the coefficients $(a_0 \ldots\ldots a_4)$ are positive, then the inequalities of (6.30) must be hold true to guarantee the stability of the system.

$$\begin{aligned} a_1a_2 - a_3a_0 > 0 \\ a_1a_2a_3 - (a_0a_3^2 + a_4a_1^2) > 0 \end{aligned} \tag{6.30}$$

Applying simplifications, the inequalities of (6.30) can be simplified as

$$0 < \frac{1}{1 - \dfrac{\left(\dfrac{I_{\mathrm{o}}}{U_{\mathrm{o}}} + \dfrac{3}{2}D_{\mathrm{q}}K_{\mathrm{pv}}\right)K_{\mathrm{pv}}}{C_{\mathrm{dc}}K_{\mathrm{iv}}}} < \frac{\omega_{\mathrm{n}}^2}{\omega_{\mathrm{nc}}^2}, \tag{6.31}$$

where ω_{nc} is the crossover frequency of the DC-link voltage control loop and can be given as

$$\omega_{\mathrm{nc}} = \sqrt{KK_{\mathrm{iv}}\omega_{\mathrm{z}}}\,. \tag{6.32}$$

Therefore, to ensure the stability of the interconnected system, the inequality of (6.31) must hold true. From (6.32), it can be realized that the control loop gain crossover frequency is depended on the operating point and the controller parameter K_{iv}. One concludes that the inequality presented in (6.31) can be true only if the controller parameters are designed so that the crossover frequency of the DC-link voltage control loop is smaller than the resonance frequency of the drive-train dynamic. Moreover, based on the set of controllability rules proposed in [35], the gain crossover frequency ω_{nc} must be smaller than $|Z_{\mathrm{RHP}}|$ where a complex RHP zero is the case. However, the worst-case should be considered to ensure the stability for all the operating point at the below the

rated wind velocity. Therefore, ω_{nc} should be smaller than the lowest $|Z_{\mathrm{RHP}}|$ which can be obtained as

$$\omega_{\mathrm{Lz2,3}} \approx \frac{\frac{1}{R_{\mathrm{fc}}}\frac{(C_{\mathrm{t}}+C_{\mathrm{g}})}{C_{\mathrm{t}}C_{\mathrm{g}}} - \frac{1}{r_{\mathrm{dyn}}C_{\mathrm{t}}} + \frac{1}{R_{\mathrm{st}}C_{\mathrm{g}}}}{2} \pm j\sqrt{\frac{L_{\mathrm{t}}(C_{\mathrm{t}}+C_{\mathrm{g}})}{C_{\mathrm{t}}C_{\mathrm{g}}}} \approx \frac{1}{2R_{\mathrm{st}}C_{\mathrm{g}}} \pm j\sqrt{\frac{L_{\mathrm{t}}(C_{\mathrm{t}}+C_{\mathrm{g}})}{C_{\mathrm{t}}C_{\mathrm{g}}}}. \quad (6.33)$$

For a complex zero $z = x \pm jy, x \geq 0$, the absolute value of the zero can be calculated as

$$|\omega_{\mathrm{Lz2,3}}| = \sqrt{\left(\frac{1}{2R_{\mathrm{st}}C_{\mathrm{g}}}\right)^2 + \frac{L_{\mathrm{t}}(C_{\mathrm{t}}+C_{\mathrm{g}})}{C_{\mathrm{t}}C_{\mathrm{g}}}}. \quad (6.34)$$

According to (6.34), the absolute value of the pair of complex RHP zeros $\omega_{\mathrm{Lz2,3}}$ depends on the operating point and the drive-train components. However, while the latter term can be assumed to be constant, the former term changes with operating point and wind speed. The static resistance is the only variable parameter that its value may vary within the different operating points and wind speed. According to (5.33) and (4.22), the largest value of R_{st} which result in the lowest frequency of RHP-zeros can be obtained in the maximum rotor speed of the lowest operating wind speed where the generator torque is at its lowest. The estimated value of the real part of the RHP-zeros that calculated based on (6.33) is shown in Figure 34 in comparison with the precise values where no approximation is taken. It can be observed that the minimum value of the real part occurs at the lowest operating wind speed in the maximum rotor speed as predicted before.

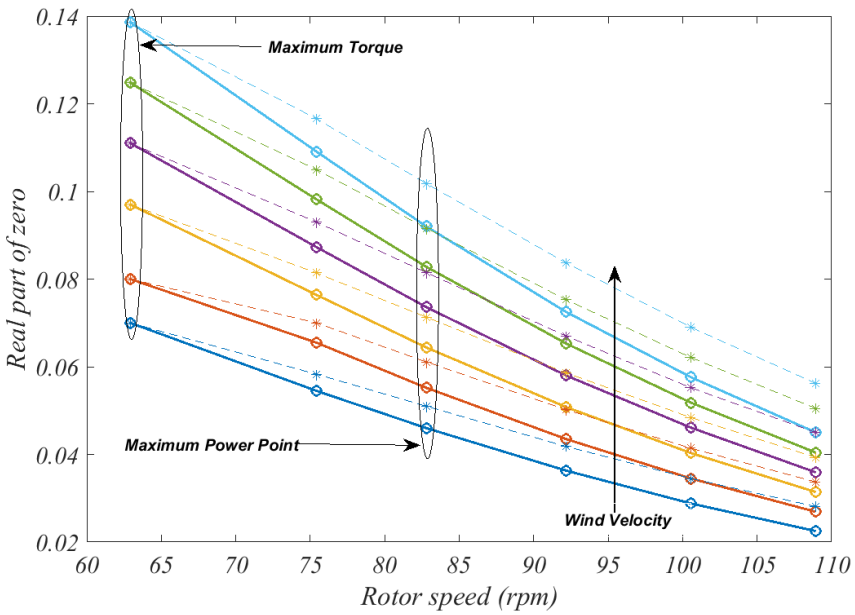

***Figure 34**. Variation of the real part of the RHP-zeros for different operating point and wind speed. Approximated values shown by the solid line and the precise one with the dashed line.*

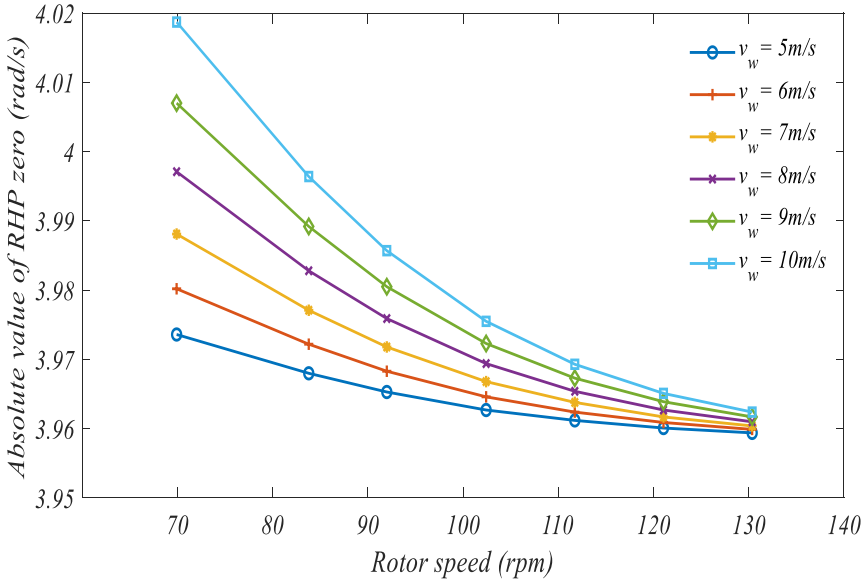

***Figure 35**. Frequency of RHP-zeros as a function of rotor speed*

The effect of the variation in the operating point and wind velocity on the frequency of the RHP-zeros is predicted as illustrated in Figure 35 where the highest frequency happens at the maximum torque operating point at the highest wind speed and the lowest frequency occurs at the maximum rotor speed of the lowest wind speed. Clearly, the effect of the wind speed variation is higher at the maximum torque point as the torque is directly proportional to the square of the wind speed and the variation is lower at the maximum rotor speed as the rotor speed is directly proportional to the wind speed. According to [35], for a complex pair of zeros, $z = x \pm jy$, the bandwidth of the control loop ω_{B} must be designed as

$$\omega_{\mathrm{B}} \approx \omega_{\mathrm{nc}} < \begin{cases} |z|/4 & Re(z) \gg Im(z) \quad (y/x \ll 1) \\ |z|/2.8 & Re(z) = Im(z) \quad (y/x = 1) \\ |z| & Re(z) \ll Im(z) \quad (y/x \gg 1) \end{cases}, \tag{6.35}$$

to ensure the stability of the system. As can be seen from Figure 36, the effect of the real part of complex RHP zeros is negligible as the frequency of torsional mode varies over a fairly narrow range which indicates that where $y/x \gg 1$ changes in operating point and wind speed do not play a key role in torsional stability studies. Hence, in this case, the natural frequency can be taken as the worst-case scenario where the crossover frequency of the control loop must be placed below ω_{n}. Therefore, by substituting (6.32) into (6.31), K_{iv} can be calculated as

$$K_{\mathrm{iv}} = \frac{C_{\mathrm{dc}}\omega_{\mathrm{n}}^2}{6D_{\mathrm{q}}}. \tag{6.36}$$

Given that, the inequality of (6.31) can be rewritten as

$$0 < \frac{1}{1 - \frac{\left(\frac{I_o}{U_o} + \frac{3}{2}D_q K_{pv}\right)K_{pv}}{C_{dc}K_{iv}}} < 4 \rightarrow \frac{\left(\frac{I_o}{U_o} + \frac{3}{2}D_q K_{pv}\right)K_{pv}}{C_{dc}K_{iv}} < \frac{3}{4}$$

$$\frac{\frac{3}{2}D_q\left(D_q\frac{I_q}{E_q} + K_{pv}\right)K_{pv}}{C_{dc}K_{iv}} \leq \frac{3}{4} \rightarrow \frac{\left(D_q\frac{I_q}{E_q} + K_{pv}\right)}{C_{dc}} \leq \frac{\omega_{zv}}{2D_q}. \quad (6.37)$$

Finally, K_{pv} must be tuned so that the inequality of (6.37) held true. Hence, by substituting (6.36) into (6.37), the inequality can be given as

$$\left(K_{pv}^2 + D_q K_{pv}\right) \leq \frac{C_{dc}^2\omega_n^2}{12D_q^2} \Rightarrow K_{pv} \leq \frac{\sqrt{\left(D_q\frac{I_q}{E_q}\right)^2 + \frac{C_{dc}^2\omega_n^2}{3D_q^2}}}{2} - \frac{D_q\frac{I_q}{E_q}}{2}. \quad (6.38)$$

From (6.38), it can be found that the maximum value for K_{pv} can be achieved at the MPP of the highest operating wind speed.

Applying the proposed guideline for tuning the PI controller parameters where the worst-case scenario is considered, the input impedance of the PMSG-connected converter under the DC-link voltage is shaped so that the interconnected system is stable under the CP mode as shown in Figure 36. The obtained predicted model is verified by the frequency response of the simulation model as illustrated in Figure 37.

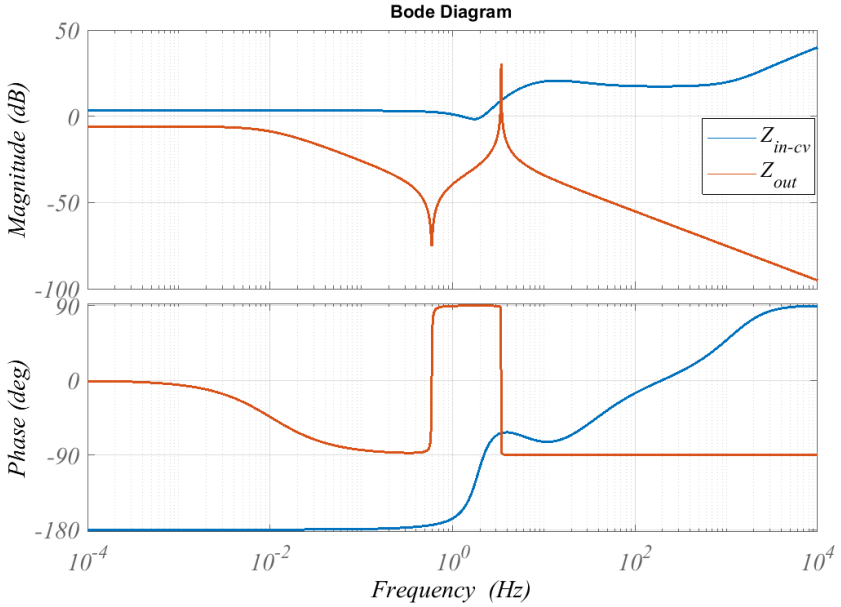

***Figure 36**. Output impedance of WT against input impedance of output voltage controlled PMSG*

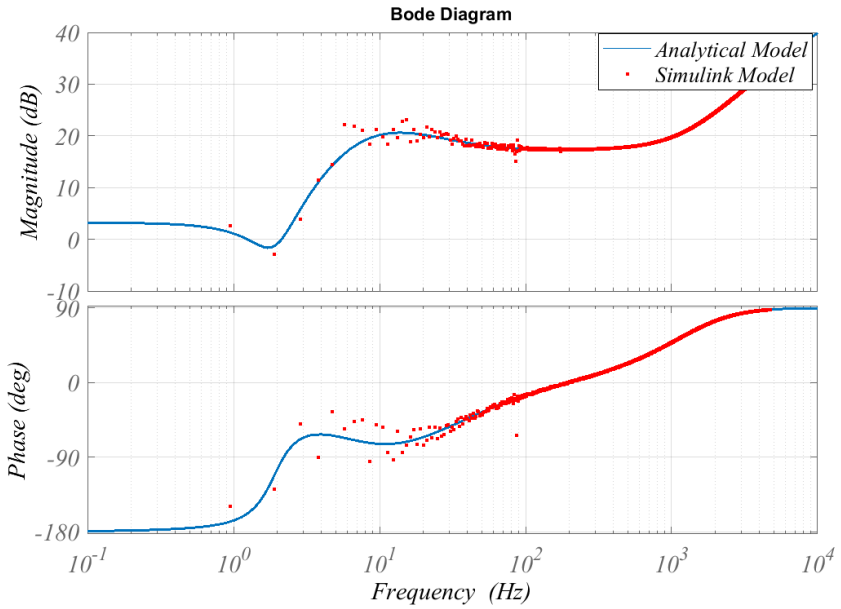

***Figure 37**. Input impedance of PMSG under DC-link voltage control*

Furthermore, the effectiveness of the DC-link voltage controller in damping the oscillatory modes caused by the WT drive-train is demonstrated in the time-domain simulations. Figure 38 shows the transient performance of the DC-link voltage where the WT initially operates at the MPP of wind speed of 7 m/s, considering that the MPPT lookup table is not employed here, after 2s the vibrations are damped in the DC-link voltage. At 4.5s, the active power controller setpoint decreases to $0.8P_{\mathrm{MPP}}$ where the voltage of DC-link fluctuates slightly and then settles down after 1s. The transient behaviour of the rotational speeds is illustrated in Figure 39 in which it can be observed that the oscillations are damped after 3 s. The active power reference change occurs at 4.5 s where the speed oscillations in the generator rotor are attenuated faster than the initial step while the oscillatory behaviour in the turbine shaft is negligible.

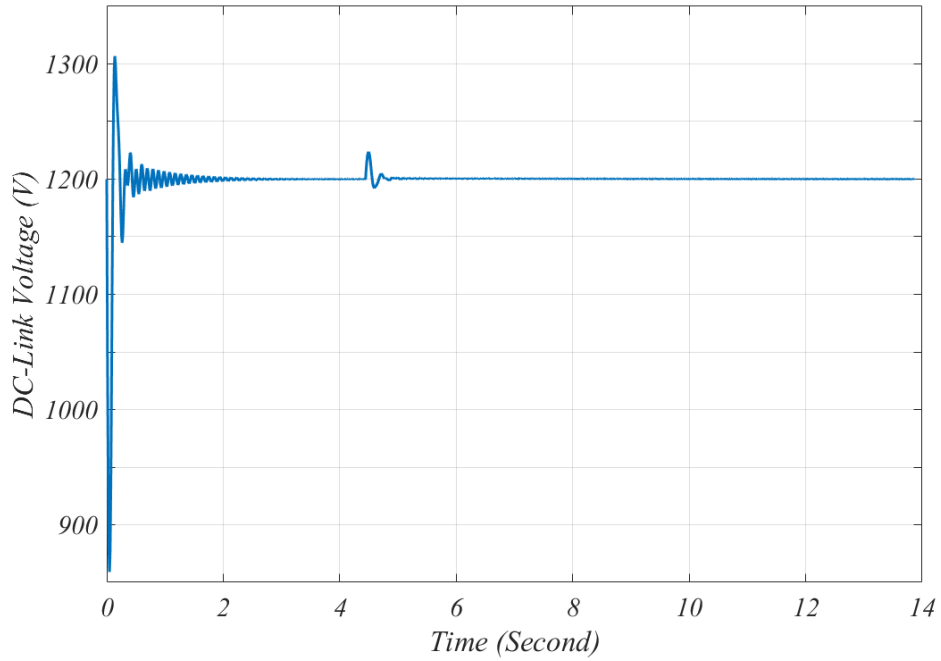

***Figure 38**. DC-Link voltage transient performance under CP mode*

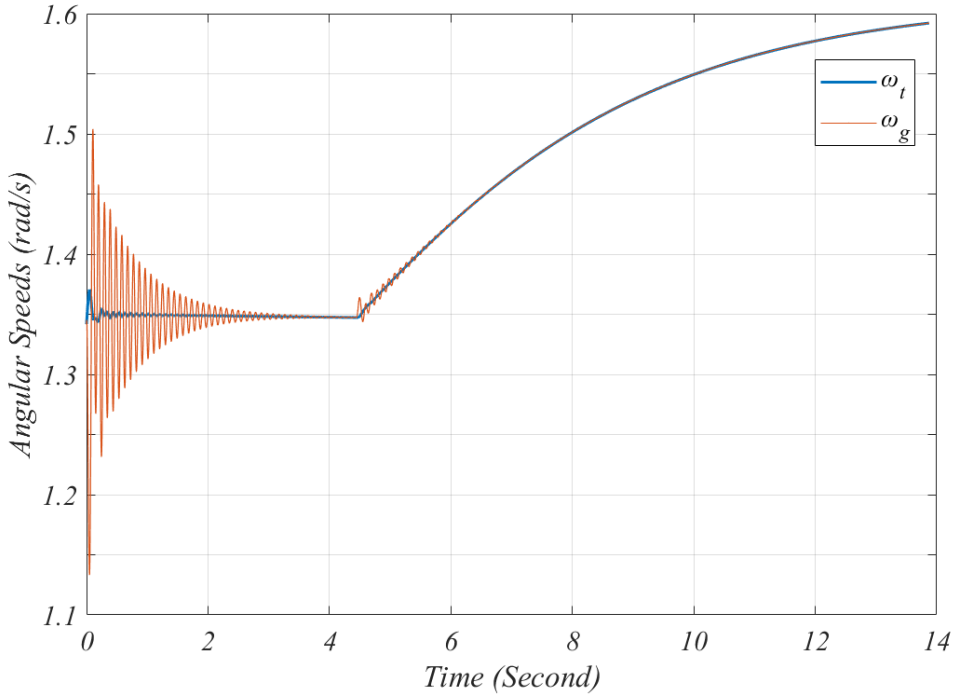

***Figure 39**. Angular speed of turbine shaft and PMSG rotor under CP mode*

7. CONCLUSIONS

In this thesis, the frequency-domain model of a conventional voltage source boost converter is adopted for the dynamic modelling of a PMSG-connected converter under the alternative control strategy. Hence, the transfer function of the input impedance for the q-channel is derived where it is found that its dynamic behaviour in the low frequency is like a negative resistor. One real right-half-plane zero which is dependent on the operating point and the wind speed is revealed in the transfer function between the DC-link voltage and the q-component control variable. Considering the worst-case scenario in the designing process where the RHP-zero is located at its lowest frequency, it is concluded that the DC-link voltage control loop must be designed at the operating point in which the maximum torque at the highest operating wind speed occurs. The effect of the wind turbine dynamics on the interfacing converter is studied in which the location of poles and zeros of the control-to-output voltage transfer function as a function of the operating point is described. It is realized that the WTG-coupled converter can be unstable when the operating point operates on the left-hand side of the torque-rotational speed curve. Furthermore, an operating-point-dependant pair of complex right-half-plane zero appears in the control-to-output voltage transfer function which is introduced by the drive-train dynamic. However, the effect of the operating point on the location of zero is found to be negligible because of generator large inertia. Moreover, one real zero emerges in the transfer function of the control-to-DC-link voltage in the WTG-coupled converter where it can be positive at the operating points that the dynamic resistance is larger than the static resistance.

The stability assessment of the wind turbine and the interfacing PMSG-connected converter is performed by the impedance ratio method and it reveals that under the open-loop condition, the interconnected system is unstable due to negative resistor-like behaviour of the converter input impedance. Under the current control loop, however, it is concluded that the interconnected system can be stable if the crossover frequency of the loop gain is designed to be high enough. Nevertheless, the oscillations are poorly damped under the closed-loop current control and a cascaded control scheme is needed to sufficiently dampen the torsional oscillations. Dynamic behaviour of the cascaded control WTG-coupled converter under the MPPT mode is analysed where one can conclude that no maximum limitations impose on the bandwidth of the DC-link voltage control loop since the plant transfer function does not contain and right-half-plane zero. However, the crossover frequency of the loop gain must be placed higher than the oscillatory mode of

the drive-train. Therefore, the same design rules for the DC-link voltage control loop designed for the PMSG-connected converter can be used for the WTG-coupled converter when operates under the MPPT mode. The stability of the interconnected system under the CP mode is evaluated and it is found that the WTG-coupled converter becomes unstable utilizing the voltage controller designed for the MPPT. Hence, a guideline for tuning the DC-link voltage PI controller parameters is developed to ensure stable operation for the interconnected system stability under the CP mode.

REFERENCES

[1] Wind energy in Europe in 2018, Trends and statistics, wind Europe, February 2019. Available (accessed on 20.09.2019):https://windeurope.org/about-wind/statistics/european/wind-energy-in-europe-in-2018/

[2] Wind power in Finland, Suomen Tuulivoimayhdistys ry, available (accessed on 05.10.2019): https://www.tuulivoimayhdistys.fi/en/wind-power-in-finland/wind-power-in-finland

[3] J.K. Pedersen, M. Akke, N.K. Poulsen, and K.O.H. Pedersen, Analysis of wind farm islanding experiment, in IEEE Trans. on Energy Conversion, vol. 15, no. 1, Mar. 2000, pp. 110-115.

[4] S. Sheng, Wind Turbine Drivetrain Condition Monitoring (Presentation). NREL (National Renewable Energy Laboratory). NREL/PR-5000-52908, 2011. Available (accessed on 10.12.2018): https://www.nrel.gov/docs/fy12osti/52908.pdf

[5] H. Polinder, F. F. A. van der Pijl, G. -. de Vilder and P. J. Tavner, Comparison of direct-drive and geared generator concepts for wind turbines, in IEEE Trans. on Energy Conversion, vol. 21, no. 3, Sept. 2006, pp. 725-733.

[6] A. Binder and T. Schneider, Permanent magnet synchronous generators for regenerative energy conversion – a survey, European Con. on Power Electronics and Applications, EPE 2005, September, Dresden, Germany, 2005, pp. 11-14.

[7] V. Akhmatov, Analysis of dynamic behavior of electric power systems with large amount of wind power, PhD thesis, Ørsted DTU, Denmark, 2003.

[8] N. Fichaux, J. Beurskens, P. H. Jensen, and J. Wilkes, UpWind Design limits and solution for very large wind turbines, 2011. Available (accessed on 10.12.2018): http://www.ewea.org/fileadmin/ewea_documents/documents/upwind/21895_UpWind_Report_low_web.pdf

[9] P.Kurronen, Challenges in applying permanent magnet technology to wind power generators, Technical Paper, The Switch 2010.

[10] G. Ramtharan, N. Jenkins, O. Anaya-Lara, and E. Bossanyi, Influence of rotor structural dynamics representations on the electrical transient performance of FSIG and DFIG wind turbines, Wind Energy, vol. 10, Jul./Aug. 2007, pp. 293-301.

[11] V. Akhmatov, A.H. Nielsen, J.K. Pedersen, and O. Nymann, Variable-speed wind turbines with multi-pole synchronous permanent magnet generators, Part I: Modelling in dynamic simulation tools, Wind Engineering, vol. 27, no. 6, 2003, pp. 531-548.

[12] H. Geng and D. Xu, Stability analysis and improvements for variable-speed multipole permanent magnet synchronous generator-based wind energy conversion system, in IEEE Trans. Sustainable Energy, vol. 2, no. 4, Oct. 2011, pp. 459-467.

[13] M.Nasiri, J.Milimonfared and S.H.Fathi, A review of low-voltage ride-through enhancement methods for permanent magnet synchronous generator-based wind turbines, Renewable and Sustainable Energy Reviews 47, March 2015, pp. 399-415.

[14] H. Geng, D. Xu, B. Wu, and G. Yang, Comparison of oscillation damping capability in three power control strategies for PMSG-based WECS, Wind Energy, vol. 14, DEC 2011, pp. 389-406.

[15] O. Alizadeh and A. Yazdani, A control strategy for power regulation in a direct-drive WECS with flexible drive-train, IEEE Trans. Sustainable Energy, vol. 5, no. 4, Oct. 2014, pp. 1156–1165.

[16] H. Geng, D. Xu, B. Wu, and G. Yang, Active damping for PMSG-based WECS with dc-link current estimation, in IEEE Trans. on Industrial Electronics, vol. 58, no.4, April 2011, pp. 1110-1119.

[17] A. Hansen and G. Michalke, Multi-pole permanent magnet synchronous generator wind turbines' grid support capability in uninterrupted operation during grid faults, IET Renewable Power Generation., vol. 3, no. 3, Sep. 2009, pp. 333–348.

[18] H. Geng, G. Yang, D. Xu, B. Wu, Unified power control for PMSG-based WECS operating under different grid conditions, IEEE Trans. Energy Conversion, vol. 26, no. 3, Sep. 2011, pp. 822-830.

[19] M. F. M. Arani and Y. A. I. Mohamed, Assessment and Enhancement of a Full-Scale PMSG-Based Wind Power Generator Performance Under Faults, in IEEE Trans. on Energy Conversion, vol. 31, no. 2, pp. 728-739, June 2016.

[20] M.Rahimi, Mathematical modeling, dynamic response analysis, and control of PMSG-based wind turbines operating with an alternative control structure in power control mode, International Trans. on Electrical Energy, Sep. 2017, pp. 1-18.

[21] Y. Xia, K. H. Ahmed and B. W. Williams, Wind Turbine Power Coefficient Analysis of a New Maximum Power Point Tracking Technique, in IEEE Trans. on Industrial Electronics, vol. 60, no. 3, pp. 1122-1132, March 2013.
[22] Z. Dalala, Z. U. Zahid and J. Lai, New overall control strategy for wind energy conversion systems in MPPT and stall regions, in IEEE Energy Conversion Congress and Exposition, Denver, CO, 2013, pp. 2412-2419.
[23] J.Licari, Control of a Variable-Speed Wind Turbine, PhD thesis, Institute of Energy, Cardiff University, Feb.2013
[24] P. Krause, O. Wasynczuk, and S. Sudhoff, Analysis of Electric Machinery and Drive Systems. New York, NY, USA: Wiley, 2013.
[25] J.Puukko, Issues on Dynamic Modeling and Design of Grid-Connected Three-Phase VSIs in Photovoltaic Applications, PhD thesis, Tampere University, November 2012.
[26] L. Harnefors, Modeling of Three-Phase Dynamic Systems Using Complex Transfer Functions and Transfer Matrices, in IEEE Trans. on Industrial Electronics, vol. 54, no. 4, Aug. 2007, pp. 2239-2248
[27] L. Harnefors, M. Bongiorno and S. Lundberg, Input-Admittance Calculation and Shaping for Controlled Voltage-Source Converters, in IEEE Trans. on Industrial Electronics, vol. 54, no. 6, Dec. 2007, pp. 3323-3334.
[28] T. Roinila, J. Huusari, and M. Vilkko, On frequency-response measurements of power-electronic systems applying MIMO identification techniques, in IEEE Trans. Industrial Electronics, vol. 60, no. 11, Nov. 2013, pp. 5270–5276.
[29] Kolar, J. W., Friedli, T., Krismer, F., Looser, A., Schweizer, M., Friedemann, R. A., Steimer, P. K. and Bevirt, J. B, Conceptualization and multiobjective optimization of the electric system of an airborne wind turbine, in IEEE Journal of Emerging and Selected Topics in Power Electronics vol. 1, no. 2, June 2013, pp.73–103.
[30] Y. Zou, M. E. Elbuluk and Y. Sozer, Stability Analysis of Maximum Power Point Tracking (MPPT) Method in Wind Power Systems, in IEEE Trans. on Industry Applications, vol. 49, no. 3, May-June 2013, pp. 1129-1136.
[31] S. Kolesnik, M. Sitbon, G. Agranovich, A. Kuperman and T. Suntio, Comparison of photovoltaic and wind generators as dynamic input sources to power processing interfaces, 2nd International Conf. on Intelligent Energy and Power Systems (IEPS), Kiev, 2016, pp.1-5.
[32] L. Nousiainen et al., Photovoltaic Generator as an Input Source for Power Electronic Converters, in IEEE Trans. on Power Electronics, vol. 28, no. 6, June 2013, pp. 3028-3038.
[33] L. Harnefors, Analysis of Subsynchronous Torsional Interaction with Power Electronic Converters, in IEEE Trans. on Power Systems, vol. 22, no. 1, Feb. 2007, pp. 305-313.
[34] T.Suntio, J.Viinamäki, J.Jokipii, T.Messo, and A.Kuperman, Dynamic characterization of power electronic interfaces, IEEE Journal of Emerging and Selected Topics in Power Electronics, vol. 2, no. 4, December 2014, pp.949-961.
[35] S.Skogestad and I.Postlethwaite, Multivariable Feedback Control: Analysis and Design, 2nd Edition, John Willey & Sons, September 2005.
[36] M. Cespedes, L. Xing and J. Sun, Constant-Power Load System Stabilization by Passive Damping, in IEEE Trans. on Power Electronics, vol. 26, no. 7, July 2011, pp. 1832-1836.

APPENDIX A: CLOSED-LOOP CURRENT CONTROL TRANSFER FUNCTIONS

The input admittances of the PMSG-connected converter under the current control loops are expressed as

$$Y_{\mathrm{in-d-c}} = \left[\frac{Y_{\mathrm{in-d}}}{1 + L_{\mathrm{in-d}}} - \frac{G_{\mathrm{ci-qd}}L_{\mathrm{in-q}}}{G_{\mathrm{ci-q}}(1 + L_{\mathrm{in-d}})} \cdot \frac{G_{\mathrm{cr-dq}}}{(1 + L_{\mathrm{in-q}})}\right] \frac{1}{1 - \frac{G_{\mathrm{ci-qd}}L_{\mathrm{in-q}}}{G_{\mathrm{ci-q}}(1 + L_{\mathrm{in-d}})} \cdot \frac{G_{\mathrm{ci-dq}}L_{\mathrm{in-d}}}{G_{\mathrm{ci-d}}(1 + L_{\mathrm{in-q}})}}, \quad (A.1)$$

$$G_{\mathrm{cr-qd-c}} = \left[\frac{G_{\mathrm{cr-qd}}}{1 + L_{\mathrm{in-d}}} - \frac{G_{\mathrm{ci-qd}}L_{\mathrm{in-q}}}{G_{\mathrm{ci-q}}(1 + L_{\mathrm{in-d}})} \cdot \frac{Y_{\mathrm{in-q}}}{(1 + L_{\mathrm{in-q}})}\right] \frac{1}{1 - \frac{G_{\mathrm{ci-qd}}L_{\mathrm{in-q}}}{G_{\mathrm{ci-q}}(1 + L_{\mathrm{in-d}})} \cdot \frac{G_{\mathrm{ci-dq}}L_{\mathrm{in-d}}}{G_{\mathrm{ci-d}}(1 + L_{\mathrm{in-q}})}}, \quad (A.2)$$

$$G_{\mathrm{cr-dq-c}} = \left[\frac{G_{\mathrm{cr-dq}}}{1 + L_{\mathrm{in-q}}} - \frac{G_{\mathrm{ci-dq}}L_{\mathrm{in-d}}}{G_{\mathrm{ci-d}}(1 + L_{\mathrm{in-q}})} \cdot \frac{Y_{\mathrm{in-d}}}{(1 + L_{\mathrm{in-d}})}\right] \frac{1}{1 - \frac{G_{\mathrm{ci-dq}}L_{\mathrm{in-d}}}{G_{\mathrm{ci-d}}(1 + L_{\mathrm{in-q}})} \cdot \frac{G_{\mathrm{ci-qd}}L_{\mathrm{in-q}}}{G_{\mathrm{ci-q}}(1 + L_{\mathrm{in-d}})}}, \quad (A.3)$$

$$Y_{\mathrm{in-q-c}} = \left[\frac{Y_{\mathrm{in-q}}}{1 + L_{\mathrm{in-q}}} - \frac{G_{\mathrm{ci-dq}}L_{\mathrm{in-d}}}{G_{\mathrm{ci-d}}(1 + L_{\mathrm{in-q}})} \cdot \frac{G_{\mathrm{cr-qd}}}{(1 + L_{\mathrm{in-d}})}\right] \frac{1}{1 - \frac{G_{\mathrm{ci-dq}}L_{\mathrm{in-d}}}{G_{\mathrm{ci-d}}(1 + L_{\mathrm{in-q}})} \cdot \frac{G_{\mathrm{ci-qd}}L_{\mathrm{in-q}}}{G_{\mathrm{ci-q}}(1 + L_{\mathrm{in-d}})}}. \quad (A.4)$$

The dynamics of the output variable to the input variables can be given as

$$G_{\mathrm{oi-d-c}} = \left[\frac{G_{\mathrm{oi-d}}}{1 + L_{\mathrm{in-d}}} - \frac{G_{\mathrm{ci-qd}}L_{\mathrm{in-q}}}{G_{\mathrm{ci-q}}(1 + L_{\mathrm{in-d}})} \cdot \frac{G_{\mathrm{oi-q}}}{(1 + L_{\mathrm{in-q}})}\right] \frac{1}{1 - \frac{G_{\mathrm{ci-qd}}L_{\mathrm{in-q}}}{G_{\mathrm{ci-q}}(1 + L_{\mathrm{in-d}})} \cdot \frac{G_{\mathrm{ci-dq}}L_{\mathrm{in-d}}}{G_{\mathrm{ci-d}}(1 + L_{\mathrm{in-q}})}}, \quad (A.5)$$

$$G_{\mathrm{oi-q-c}} = \left[\frac{G_{\mathrm{oi-q}}}{1 + L_{\mathrm{in-q}}} - \frac{G_{\mathrm{ci-dq}}L_{\mathrm{in-d}}}{G_{ci-\mathrm{d}}(1 + L_{\mathrm{in-q}})} \cdot \frac{G_{\mathrm{oi-d}}}{(1 + L_{\mathrm{in-d}})}\right] \frac{1}{1 - \frac{G_{\mathrm{ci-dq}}L_{\mathrm{in-d}}}{G_{\mathrm{ci-d}}(1 + L_{\mathrm{in-q}})} \cdot \frac{G_{\mathrm{ci-qd}}L_{\mathrm{in-q}}}{G_{\mathrm{ci-q}}(1 + L_{\mathrm{in-d}})}}. \quad (A.6)$$

The dynamic of the control variables to the inductor currents of the PMSG-connected converter are presented as

$$G_{\mathrm{ci-d-c}} = \left[\frac{L_{\mathrm{in-d}}}{(1 + L_{\mathrm{in-d}})} - \frac{G_{\mathrm{ci-qd}}L_{\mathrm{in-q}}}{G_{\mathrm{ci-q}}(1 + L_{\mathrm{in-d}})} \cdot \frac{G_{\mathrm{ci-dq}}L_{\mathrm{in-d}}}{(1 + L_{\mathrm{in-q}})G_{\mathrm{ci-d}}}\right] \frac{1}{1 - \frac{G_{\mathrm{ci-qd}}L_{\mathrm{in-q}}}{G_{\mathrm{ci-q}}(1 + L_{\mathrm{in-d}})} \cdot \frac{G_{\mathrm{ci-dq}}L_{\mathrm{in-d}}}{G_{\mathrm{ci-d}}(1 + L_{\mathrm{in-q}})}}, \quad (A.7)$$

$$G_{\mathrm{ci-qd-c}} = \left[\frac{G_{\mathrm{ci-qd}}L_{\mathrm{in-q}}}{(1+L_{\mathrm{in-d}})G_{\mathrm{ci-q}}} - \frac{G_{\mathrm{ci-qd}}L_{\mathrm{in-q}}}{G_{\mathrm{ci-q}}(1+L_{\mathrm{in-d}})} \cdot \frac{L_{\mathrm{in-q}}}{(1+L_{\mathrm{in-q}})}\right] \frac{1}{1-\frac{G_{\mathrm{ci-qd}}L_{\mathrm{in-q}}}{G_{\mathrm{ci-q}}(1+L_{\mathrm{in-d}})} \cdot \frac{G_{\mathrm{ci-dq}}L_{\mathrm{in-d}}}{G_{\mathrm{ci-d}}(1+L_{\mathrm{in-q}})}}, \quad (A.8)$$

$$G_{\mathrm{ci-dq-c}} = \left[\frac{G_{\mathrm{ci-dq}}L_{\mathrm{in-d}}}{(1+L_{\mathrm{in-q}})G_{\mathrm{ci-d}}} - \frac{G_{\mathrm{ci-dq}}L_{\mathrm{in-d}}}{G_{\mathrm{ci-d}}(1+L_{\mathrm{in-q}})} \cdot \frac{L_{\mathrm{in-d}}}{(1+L_{\mathrm{in-d}})}\right] \frac{1}{1-\frac{G_{\mathrm{ci-dq}}L_{\mathrm{in-d}}}{G_{\mathrm{ci-d}}(1+L_{in-q})} \cdot \frac{G_{\mathrm{ci-qd}}L_{\mathrm{in-q}}}{G_{\mathrm{ci-q}}(1+L_{\mathrm{in-d}})}}, \quad (A.9)$$

$$G_{\mathrm{ci-q-c}} = \left[\frac{L_{\mathrm{in-q}}}{(1+L_{\mathrm{in-q}})} - \frac{G_{\mathrm{ci-dq}}L_{\mathrm{in-d}}}{G_{\mathrm{ci-d}}(1+L_{\mathrm{in-q}})} \cdot \frac{G_{\mathrm{ci-qd}}L_{\mathrm{in-q}}}{(1+L_{\mathrm{in-d}})G_{\mathrm{ci-q}}}\right] \frac{1}{1-\frac{G_{\mathrm{ci-dq}}L_{\mathrm{in-d}}}{G_{\mathrm{ci-d}}(1+L_{\mathrm{in-q}})} \cdot \frac{G_{\mathrm{ci-qd}}L_{\mathrm{in-q}}}{G_{\mathrm{ci-q}}(1+L_{\mathrm{in-d}})}}. \quad (A.10)$$

The dynamic behaviour of the input variables to the output voltage can be described as

$$T_{\mathrm{io-d-c}} = T_{\mathrm{io-d}} - \frac{G_{\mathrm{co-d}}}{G_{\mathrm{ci-d}}}L_{\mathrm{in-d}}Y_{\mathrm{in-d-c}} - \frac{G_{\mathrm{co-q}}}{G_{\mathrm{ci-q}}}L_{\mathrm{in-q}}G_{\mathrm{cr-dq-c}}, \quad (A.11)$$

$$T_{\mathrm{io-q-c}} = T_{\mathrm{io-q}} - \frac{G_{\mathrm{co-d}}}{G_{\mathrm{ci-d}}}L_{\mathrm{in-d}}G_{\mathrm{cr-qd-c}} - \frac{G_{\mathrm{co-q}}}{G_{\mathrm{ci-q}}}L_{\mathrm{in-q}}Y_{\mathrm{in-q-c}}. \quad (A.12)$$

The output impedance of the converter under the current control can be given as

$$Z_{\mathrm{o-c}} = Z_{\mathrm{o}} - \frac{G_{\mathrm{co-d}}}{G_{\mathrm{ci-d}}}L_{\mathrm{in-d}}G_{\mathrm{oi-d-c}} - \frac{G_{\mathrm{co-q}}}{G_{\mathrm{ci-q}}}L_{\mathrm{in-q}}G_{\mathrm{oi-q-c}}. \quad (A.13)$$

The control-to-output voltage transfer functions under the closed-loop current can be expressed as

$$G_{\mathrm{co-d-c}} = \frac{G_{\mathrm{co-d}}}{G_{\mathrm{ci-d}}}L_{\mathrm{in-d}} - \frac{G_{\mathrm{co-q}}}{G_{\mathrm{ci-d}}}L_{\mathrm{in-d}}G_{\mathrm{ci-d-c}} - \frac{G_{\mathrm{co-q}}}{G_{\mathrm{ci-q}}}L_{\mathrm{in-q}}G_{\mathrm{ci-dq-c}}, \quad (A.14)$$

$$G_{\mathrm{co-q-c}} = \frac{G_{\mathrm{co-q}}}{G_{\mathrm{ci-q}}}L_{\mathrm{in-q}} - \frac{G_{\mathrm{co-d}}}{G_{\mathrm{ci-d}}}L_{\mathrm{in-d}}G_{\mathrm{ci-qd-c}} - \frac{G_{\mathrm{co-q}}}{G_{\mathrm{ci-q}}}L_{\mathrm{in-q}}G_{\mathrm{ci-q-c}}. \quad (A.15)$$

APPENDIX B: CASCADED CONTROL TRANSFER FUNCTIONS

The transfer functions of the input dynamics under the output voltage control are presented by

$$Y_{\mathrm{in-d-cv}} = \frac{Y_{\mathrm{in-d-c}}}{1 + L_{\mathrm{v}}} + \frac{L_{\mathrm{v}}}{1 + L_{\mathrm{v}}} Y_{\mathrm{in-d-inf}}, \quad (B.1)$$

$$G_{\mathrm{cr-qd-cv}} = \frac{G_{\mathrm{cr-qd-c}}}{1 + L_{\mathrm{v}}} + \frac{L_{\mathrm{v}}}{1 + L_{\mathrm{v}}} G_{\mathrm{cr-qd-inf}}, \quad (B.2)$$

$$G_{\mathrm{cr-dq-cv}} = \frac{G_{\mathrm{cr-dq-c}}}{1 + L_{\mathrm{v}}} + \frac{L_{\mathrm{v}}}{1 + L_{\mathrm{v}}} G_{\mathrm{cr-dq-inf}}, \quad (B.3)$$

$$Y_{\mathrm{in-q-cv}} = \frac{Y_{\mathrm{in-q-c}}}{1 + L_{\mathrm{v}}} + \frac{L_{\mathrm{v}}}{1 + L_{\mathrm{v}}} Y_{\mathrm{in-q-inf}}, \quad (B.4)$$

where

$$Y_{\mathrm{in-d-inf}} = Y_{\mathrm{in-d}} - \frac{G_{\mathrm{io-q}} G_{\mathrm{ci-d}}}{G_{\mathrm{co-d}}}, \quad (B.5)$$

$$G_{\mathrm{cr-qd-inf}} = G_{\mathrm{cr-qd}} - \frac{G_{\mathrm{io-q}} G_{\mathrm{ci-qd}}}{G_{\mathrm{co-q}}}, \quad (B.6)$$

$$G_{\mathrm{cr-dq-inf}} = G_{\mathrm{cr-dq}} - \frac{G_{\mathrm{io-d}} G_{\mathrm{ci-dq}}}{G_{\mathrm{co-d}}}, \quad (B.7)$$

$$Y_{\mathrm{in-q-inf}} = Y_{\mathrm{in-q}} - \frac{G_{\mathrm{io-d}} G_{\mathrm{ci-q}}}{G_{\mathrm{co-q}}}. \quad (B.8)$$

The output dynamics under the cascade control scheme, where both the DC-link voltage and the current loops are closed, can be given:

$$G_{\mathrm{io-d-cv}} = \frac{G_{\mathrm{io-d-c}}}{1 + L_{\mathrm{v}}}, \quad (B.9)$$

$$G_{\mathrm{io-q-cv}} = \frac{G_{\mathrm{io-q-c}}}{1 + L_{\mathrm{v}}}, \quad (B.10)$$

$$Z_{\mathrm{o-cv}} = \frac{Z_{\mathrm{o-c}}}{1 + L_{\mathrm{v}}}, \quad (B.11)$$

$$G_{\mathrm{co-d-cv}} = \frac{G_{\mathrm{co-d-c}}}{1 + L_{\mathrm{v}}}, \quad (B.12)$$

$$G_{\mathrm{co-q-cv}} = \frac{L_{\mathrm{v}}}{1 + L_{\mathrm{v}}}. \quad (B.13)$$

APPENDIX C: STUDY CASE PARAMETERS

Table 1. *Wind turbine parameters.*

Quantity	Value
Rated power	1.6MW
Rated wind speed	12m/s
Rated angular speed	22rpm
Rotor radius	33m
Blade parameters $(c_0, c_1, c_2, c_3, c_4, c_5, c_6)$	0.22,116,0.4,5, -12.5,0.08,0.035
Optimum tip speed ratio	6.33
Maximum power coefficient	0.44
Turbine inertia	2.9 ×10^6 kgm^2

Table 2. *PMSG parameters.*

Quantity	Value
Rated power	1.5MW
Rated voltage	690V
Rated current	1775A
Rated frequency	17.6Hz
Number of pole pairs	48
Flux induced by magnets	5.34
Stator resistance	22.4mΩ
Stator d-and q-axis inductance	1.5mH
Generator inertia	90000 kgm^2

Table 3. *Drive-train and other parameters.*

Quantity	Value
Shaft stiffness	4×10^7 Nm/rad
Air mass density	1.237 kg/m^3
DC-link capacitor	25 mF
DC-link voltage	1200V

Table 4. *Controller parameters.*

Controller	Value
Current loop	
K_{cd}, K_{cq}	-0.63
$\omega_{zc-d}, \omega_{zc-q}$	300
$\omega_{pc-d}, \omega_{pc-q}$	6.2832e+03
Voltage loop MPPT mode	
K_{pv}	3
K_{iv}	100
Voltage loop CP mode	
K_{pv}	0.25
K_{iv}	5